

Energy-domain synchrotron radiation Mössbauer source for physics under extreme conditions

DISSERTATION

zur Erlangung des akademischen Grades eines
Doktors der Naturwissenschaften (Dr. rer. nat.)
an der Bayreuther Graduiertenschule für Mathematik und
Naturwissenschaften (BayNAT) der Universität Bayreuth

vorgelegt von

Vasily Potapkin
aus Ekaterinburg (Russland)

Bayreuth, 2012

Die vorliegende Arbeit wurde in der Zeit von März 2009 bis Juli 2012 am Bayerisches Geoinstitut der Universität Bayreuth unter der Leitung von Herrn Prof. Dr. Leonid Dubrovinsky angefertigt.

Vollständiger Abdruck der von der Fakultät für Chemie/Biologie/Geowissenschaften der Universität Bayreuth genehmigten Dissertation zur Erlangung des Grades eines Doktors der Naturwissenschaften (Dr. rer. nat.).

Tag der Einreichung: 20 June 2012

Tag der wissenschaftlichen Kolloquiums: 22 October 2012

Amtierende Dekanin: Prof. Dr. Beate Lohnert

Prüfungsausschuß:

Prof. Dr. Tomoo Katsura, Universität Bayreuth	(Vorsitzender)
Prof. Dr. Leonid Dubrovinsky, Universität Bayreuth	(Erstgutachter)
Prof. Dr. Alexei Bosak, ESRF	(Zweitgutachter)
Prof. Dr. S. Kümmel, Universität Bayreuth	
Prof. Dr. J. Senker, Universität Bayreuth	

Table of Contents

ZUSAMMENFASSUNG	5
SUMMARY	9
1. INTRODUCTION	12
1.1 ORIGIN AND THE STRUCTURE OF THE EARTH	12
1.2 MINERALOGICAL MODEL OF THE MANTLE. (Mg,Fe)(Si,Al)O ₃ PEROVSKITE AS DOMINANT COMPONENT OF THE EARTH LOWER MANTLE	16
2. MOTIVATION	22
2.1 SPIN STATE OF IRON IN THE LOWER MANTLE SILICATE PEROVSKITE	22
2.2 NEED FOR ENERGY-DOMAIN SYNCHROTRON MÖSSBAUER SPECTROSCOPY	23
3. METHODS AND INSTRUMENTATION	25
3.1 CREATION OF HIGH PRESSURE	25
3.2 MÖSSBAUER SPECTROSCOPY	27
4. SYNOPSIS (SCOPE OF THE THESIS)	32
4.1 THEORETICAL CALCULATION AND EXPERIMENTAL STUDY OF ANGULAR DEPENDENCES AND ENERGY, TEMPORAL DISTRIBUTIONS OF SYNCHROTRON-BASED ⁵⁷ Fe MÖSSBAUER RADIATION	32
4.2 THE ⁵⁷ Fe SYNCHROTRON MÖSSBAUER SOURCE	37
4.3 SPIN STATE OF Fe ³⁺ IN THE LOWER MANTLE	39
4.4 DOUBLE SIDED LASER SYSTEM FOR SMS AND X-RAY DIFFRACTION	42
4.5 LIST OF MANUSCRIPTS AND STATEMENT OF AUTHOR'S CONTRIBUTION	43
MANUSCRIPTS	46
5.1 MULTISPACE QUANTUM INTERFERENCE IN ⁵⁷Fe SYNCHROTRON MÖSSBAUER SOURCE	46
5.1.1 ABSTRACT	46
5.1.2 INTRODUCTION	47
5.1.3 MULTISPACE INTERFERENCE OF γ RAY PHOTON IN THE UNIT CELL OF ⁵⁷ FeBO ₃ CRYSTAL.	50
5.1.4 NUCLEAR EXCITON POLARITON UNDER DIFFRACTION CONDITIONS	60
5.1.5 ANGULAR, ENERGY AND TIME DISTRIBUTIONS OF Fe SM RADIATION	65
5.1.6 SUMMARY AND CONCLUSION	73
5.2 ANGULAR DEPENDENCIES OF SPECTRAL AND TEMPORAL DISTRIBUTIONS OF NUCLEAR RESONANCE RADIATION OF SYNCHROTRON-BASED ⁵⁷Fe MÖSSBAUER SOURCE	76
5.2.1 ABSTRACT	76
5.2.2 INTRODUCTION	77
5.2.3. EXPERIMENTAL METHODS	79
5.2.4. RESULTS AND DISCUSSION	81
5.2.5 SUMMARY	85

5.3 THE ^{57}Fe SYNCHROTRON MÖSSBAUER SOURCE AT THE ESRF	87
5.3.1 ABSTRACT	87
5.3.2 INTRODUCTION	88
5.3.3 SYNCHROTRON MÖSSBAUER SOURCE	91
5.3.4 OPTICAL SCHEME	102
5.3.5 PROPERTIES OF THE SMS RADIATION	106
5.3.6 APPLICATIONS	108
5.3.7 CONCLUSIONS	111
5.4 NO SPIN TRANSITION OF FERRIC IRON IN THE LOWER MANTLE	112
5.4.1 ABSTRACT	112
5.4.2 INTRODUCTION	112
5.4.3. EXPERIMENTAL METHODS	113
5.4.4. RESULTS AND DISCUSSION	114
5.4.5. SUPPLEMENTARY INFORMATION	119
5.5 PORTABLE DOUBLE-SIDED LASER-HEATING SYSTEM FOR ENERGY-DOMAIN MÖSSBAUER SPECTROSCOPY AT SYNCHROTRON AND SINGLE CRYSTAL DIFFRACTION EXPERIMENTS WITH DIAMOND ANVIL CELLS	128
5.5.1 ABSTRACT	128
5.5.2 INTRODUCTION	128
5.5.3. DESIGN OF THE LASER-HEATING SYSTEM	130
5.5.4. EXAMPLES OF APPLICATION OF THE PORTABLE LASER-HEATING SYSTEM	135
5.5.5. CONCLUSIONS	139
5.6 FULL LIST OF PUBLICATIONS (WITH PAPERS NOT INCLUDED INTO THE THESIS)	141
BIBLIOGRPHY	142
ACKNOWELEGMENTS	156
ERKLÄRUNG	157

Zusammenfassung

Eisen ist eines der häufigsten Elemente der Erde und eine wichtige Komponente in Mineralien. Elektrische und magnetische Eigenschaften eisenhaltiger Materialien beeinflussen signifikant Prozesse in der Tiefe der Erde. In den Mineralien, die den Unteren Mantel ausmachen, kann Eisen sowohl in verschiedenen Valenz- und Spinzuständen als auch in verschiedenen kristallographischen Umgebungen vorkommen. Die meisten experimentellen Techniken gestatten es nicht, die Entwicklung der Eigenschaften verschiedener Eisenplätze individuell zu verfolgen oder sie sind nicht geeignet für Untersuchungen unter gleichzeitigen Hochdruck- und Hochtemperaturbedingungen. Unter diesen Bedingungen werden Untersuchungen zur elektronischen Struktur von Eisen eine große Herausforderung.

Die vorliegende Doktorarbeit ist in zwei Hauptabschnitte gegliedert. Der erste Teil beschäftigt sich mit der Entwicklung einer Synchrotron Mössbauer Quelle (Synchrotron Mössbauer Source, SMS). Sie erlaubt eine energieabhängige Mössbauerspektroskopie von Proben unter Drücken jenseits von 100 GPa in lasergeheizten Diamanthochdruckzellen. Der zweite Teil der Arbeit ist dem Verhalten von Eisen in eisen-/aluminiumhaltigen Silikat-Perowskiten unter Bedingungen des Unteren Mantels gewidmet.

1. Synchrotron Mössbauer Quelle

Es existieren mehrere Techniken, um elektrische und magnetische Eigenschaften von Materialien unter extremen Bedingungen zu untersuchen: Röntgenemissionsspektroskopie (XES), Nahkanten-Röntgenabsorptionsspektroskopie (XANES), Kernresonanzstreuung, usw. Die ausgereifteste, empfindlichste und geeigneteste Technik für solche Studien ist jedoch die (energiedifferenzielle) Mössbauerspektroskopie.

Die niedrige Brillanz der dazu benötigten radioaktiven Quellen und die niedrige Anreicherung des Eisens in den Mineralien des Unteren Mantels erfordert jedoch im Falle der energieaufgelösten Mössbauerspektroskopie lange Messzeiten und limitiert die Anwendung auf moderate Drücke. Dieser Umstand würde durch die Kombination der ausergewöhnlichen Eigenschaften der Synchrotronstrahlung (hohe Brillanz, Möglichkeiten zur extremen Fokussierung) mit denen der klassischen Mössbauerspektroskopie gelöst werden. In kurz: Es wird eine Synchrotronquelle mit

Mössbauerstrahlung benötigt. Die Konstruktion einer solchen Quelle war die Hauptaufgabe meiner Promotionsarbeit. Smirnov et al. (1997) hat die Möglichkeit einer solchen Quelle an der Nuclear Resonance Beamline (ID18) der European Synchrotron Facility (ESRF) demonstriert. Die Quelle basiert auf reinen Kernreflexen im antiferromagnetischen Kristall FeBO_3 .

Die technischen Hauptaufgaben meiner Promotionsarbeit waren (a) die Konstruktion einer permanent verfügbaren Quelle mit (b) der bestmöglichen Energieauflösung bei gleichzeitiger höchstmöglicher Intensität. Um diese Ziele zu erreichen, wurden zunächst theoretische Rechnungen durchgeführt, um die beste Strategie zur Optimierung der Quelle zu finden. Mehrere Experimente folgten, um die theoretischen Ergebnisse zu verifizieren. Zudem wurden mehrere optische Anordnungen der SMS getestet, um die optimale Anordnung zu bestimmen.

Das Ergebnis des wissenschaftlichen Entwicklungsprogramms ist eine wirkungsvolle Synchrotron Mössbauer Quelle für Hochdruckanwendungen an der Nuclear Resonance Beamline (ID18) der ESRF. Theoretische und experimentelle Ergebnisse zur Winkelabhängigkeit der Energie- und Zeitverteilung der reinen Kernreflexe des Eisenboratkristalles erlaubten es, die SMS bezüglich höchstmöglicher Intensität und bestmöglicher Energieauflösung zu optimieren. Die Energiebandbreite der Strahlung der SMS ist etwa 15 neV ($3 \Gamma_0$), die Intensität etwa $2,5 \cdot 10^4$ Photonen/s und der typische durchstimmbare Geschwindigkeitsbereich etwa ± 12 mm/s ($\pm 0,6$ μeV). Im Gegensatz zu klassischen radioaktiven Quellen kann die Strahlung der SMS in den Bereich von zehn Mikrometern fokussiert werden. Die SMS ist ein 'in-line' Monochromator, der permanent in der optischen Hütte der Beamline installiert ist und nach Einbringung in den Synchrotronstrahl betriebsbereit ist. Sie kann in Verbindung mit allen verfügbaren Probenumgebungen der Beamline betrieben werden.

Die Verfügbarkeit der SMS eröffnet Möglichkeiten, Systeme mit komplexen Hyperfeinstrukturen unter extremen Bedingungen zu untersuchen, wie z.B. unter Ultrahochvakuum und Hochdruck. Weiterhin erlaubt es die Quelle, Spektren in sehr kurzer Zeit, d.h. in wenigen Minuten, zu messen; kurz genug, um Daten auch in Verbindung mit Laserheizung zu nehmen. Mehrere Hochdruckmessungen und kombinierte Hochdruck-, Hochtemperaturmessungen wurden im Rahmen der Doktorarbeit durchgeführt. Diese werden im zweiten Teil der Doktorarbeit beschrieben. Die fast 100-prozentige rückstoßfreie Strahlung der Quelle und ihre hohe

Brillanz erlaubt viele SMS Anwendungen. Die SMS kann in allen Betriebsmoden eines Synchrotrons betrieben werden.

2. Untersuchungen zum Spinzustand der Fe^{3+} Ionen in Perowskiten

Silikat-Perowskit $(\text{Mg,Fe})(\text{Si,Al})\text{O}_3$ ist die am häufigsten vorkommende Phase im Unteren Mantel der Erde. Die Kenntnis ihrer Eigenschaften ist unabdingbar für das Verständnis des Verhaltens des Unteren Mantels. Dynamische, thermodynamische und Transporteigenschaften der Silikat-Perowskite können empfindlich durch den Valenz- und Spinzustand des Eisens beeinflusst werden. Silikat-Perowskite mit 5-10 mol% Eisen ($\text{Fe}^{3+} / \Sigma\text{Fe} \sim 50\text{-}75\%$; McCammon et al., 1997) und Al ist die dominante Phase im Unteren Mantel der Erde ($\sim 75\text{ vol}\%$)(Zhang et al., 2006; Stackhouse et al., 2007). Dennoch bleiben die Veränderungen der elektronischen Eigenschaften des Eisens unter ähnlichen Bedingungen wie des Unteren Mantels weiterhin umstritten.

Der zweite Teil meiner Promotionsarbeit ist den Untersuchungen des Spinzustandes in Fe^{3+} reichen Silikat-Perowskiten unter Hochdruck gewidmet. Vier verschiedene Silikat-Perowskitproben mit unterschiedlicher Stöchiometrie wurden mit Hilfe der Synchrotron Mössbauer Quelle untersucht. Die SMS Spektren wurden bei Raumtemperatur und unter Drücken bis 122 GPa in einer Diamant-Stempelzelle gemessen. Es wurden Proben wie hergestellt bzw. auch thermisch ausgeheilte (mittels Laserheizung) benutzt.

Die aus den Messungen gewonnenen Hyperfeinwechselwirkungsparameter, d.h., die Isomerieverschiebung und die Quadrupolaufspaltung, sind bei gleichem Druck für alle Proben dieser Arbeit innerhalb des experimentellen Fehlers gleich. Zudem ändert sich das $\text{Fe}^{3+}/\Sigma\text{Fe}$ Verhältnis nicht für die individuellen Proben über den gesamten Druckbereich des Experiments. Die Hyperfeinwechselwirkungsparameter des Fe^{3+} -Dubletts entsprechen einem Hochspinzustand (Gütlich et al., 2011) und ihre flache Abhängigkeit vom Druck deutet an, dass Fe^{3+} keinen Spinübergang im gesamten Druckbereich macht. Alle beobachteten Änderungen in den Spektren sind den Änderungen des elektronischen Zustandes des Fe^{2+} zuzuschreiben. Die Hyperfeinwechselwirkungsparameter des Fe^{2+} -Dubletts mit der kleinen Quadrupolaufspaltung entsprechen einem Hochspinzustand (McCammon et al., 2008), während das Dublett mit der grossen Quadrupolaufspaltung, dessen Anteil mit zunehmendem Druck auf Kosten des

Hochspinzustandes zunimmt, entweder einem Zwischenspinzustand (IS) des Fe^{2+} entspricht (McCammon et al., 2008) oder mit einer Verzerrung der Umgebung des Platzes des Hochspin- Fe^{2+} erklärt werden kann (Hsu et al., 2010). Ungeachtet der Interpretation des Fe^{2+} Spinzustandes bleibt die Schlussfolgerung bezüglich des nicht vorhandenen Spinüberganges in Fe^{3+} dieselbe.

Diese Ergebnisse zeigen, dass der kürzlich berichtete Spinübergang in Fe^{3+} nicht stattfindet, wenn Fe^{3+} Ionen die A-Plätze besetzen. In diesem Fall bleiben die Fe^{3+} Ionen in Silikat-Perowskiten sowohl mit als auch ohne Aluminium bis mindestens 122 GPa im Hochspinzustand. Dieser Druck entspricht fast den Bedingungen, die an der Grenze zwischen dem Unteren Mantel und dem Äusseren Kern herrschen. Die Ergebnisse zeigen auch, dass Fe^{3+} Ionen unter Hochtemperaturausheilung und Hochdruck nicht von den A-Plätzen in die B-Plätze diffundieren. Demzufolge gibt es auch kein Anzeichen für einen Hochspin- zu Niederspinübergang auf Grund eines Platzwechsels der Fe^{3+} Ionen. Dies steht im Gegensatz zu den Fe^{2+} Ionen, die von einem Hochspin- in einen Zwischenspinzustand übergehen, ohne dabei einen Niederspinzustand bei Raumtemperatur in dem untersuchten Druckbereich zu erreichen. Diese Ergebnisse lassen vermuten, dass die seismischen Geschwindigkeitsanomalien im Unteren Mantel nicht einem Spinübergang in Fe^{3+} zuzuschreiben sind.

Summary

Iron is one of the most abundant elements on Earth, and it is an important component in minerals. Electronic and magnetic properties of iron-bearing materials significantly affect processes occurring in the deep interior of the Earth. In the materials that make up the Earth's lower mantle iron may exist in different valence, spin states and crystallographic environments. Most of the existing experimental techniques either do not allow to separately follow evolution of different iron sites or are not suitable for measurements under high-pressure/high-temperature conditions. This makes studies of iron electronic structure under such conditions extremely challenging.

The current Ph.D. thesis is divided into two major parts. The first part is dedicated to the development of a Synchrotron Mössbauer Source (SMS). This device allows energy domain Mossbauer spectroscopy to be performed on a sample under pressures above 100 GPa in laser heated diamond anvil cells. The second part is dedicated to studying the behavior of iron in iron/alumina-bearing silicate perovskite under conditions of the Earth's lower mantle.

1. Synchrotron Mössbauer Source

There are several techniques that allow magnetic and electronic properties of materials under extreme conditions to be probed: X-ray Emission Spectroscopy (XES), X-ray absorption near edge structure (XANES), Nuclear Resonance Spectroscopies, *etc.* For elements in which observation of Mössbauer effect is possible the most mature, sensitive, and suitable technique for studies of magnetic and electronic properties is energy-domain Mössbauer spectroscopy.

However, due to low brilliance of utilized radioactive sources and low natural abundance of iron in lower mantle minerals measurements using conventional energy-resolved Mössbauer spectroscopy require very long time and usually are limited to moderate pressures. The problem can be solved by combining the outstanding properties of synchrotron radiation (high brilliance, possibility for extreme focusing) with the energy-resolved approach. In brief, what is needed is a synchrotron source of Mössbauer radiation. Construction of such source was the primary task of my PhD work. The possibility to develop such a source was demonstrated at the Nuclear Resonance beamline ID18 at the European Synchrotron Radiation Facility (ESRF) by Smirnov *et al.* (1997). The source is based on pure nuclear reflections existing in antiferromagnetic $^{57}\text{FeBO}_3$ crystals.

The major technical goals of my PhD work were to (a) construct a device that would be permanently ready for operation, and (b) optimize it to have the best possible resolution and highest possible intensity. In order to achieve these goals theoretical calculations were first conducted to understand how to best improve the performance. Second, several experiments were performed to confirm the theoretically predicted results. Third, several optical schemes of the SMS were tested in order to determine the optimal setup.

As a result of the research and development program a powerful Synchrotron Mössbauer Source (SMS) for high-pressure applications was constructed at the Nuclear Resonance beamline (ID18) of the ESRF. Using results obtained in the combined theoretical/experimental study of angular dependence of energy and temporal distributions of the pure nuclear reflections of iron borate crystal, the SMS was optimized for the highest possible intensity and best possible resolution. The bandwidth of radiation provided by the SMS is between 10-15 neV (2-3 Γ_0 , where Γ_0 is a natural linewidth of Mössbauer resonance for Iron), the intensity is $\sim 2.5 \times 10^4$ photons/s and the typical scanning velocity range is about ± 12 mm/s (± 0.6 μ eV). In contrast to conventional radioactive sources, the SMS gives the possibility to focus the beam to tens of microns. SMS is the in-line monochromator, permanently located in the optics hutch and operational immediately after moving it into the incident beam position. The source can be used with all existing sample environments in the experimental hutches downstream of the beamline.

The implementation of this device opens the possibility for studying systems with complex hyperfine structure utilizing energy-resolved approach under various extreme conditions, for example at high-pressure. Furthermore, the SMS allows for very short collection times of only a few minutes, which enables data to be collected during laser heating. Several high-pressure and high-pressure/high-temperature studies that have already been performed are described in the second part of this Ph.D. thesis. The almost 100% recoilless resonant radiation delivered by the source and its high brightness allow a broad field of SMS applications. The SMS can be utilized in any mode of synchrotron storage ring operation.

2. Study of the spin state of Fe^{3+} ions in perovskite

Silicate perovskite $(\text{Mg,Fe})(\text{Si,Al})\text{O}_3$ is the most abundant phase in the Earth's lower mantle. Knowledge of its properties is indispensable for understanding lower mantle behavior. Dynamic, thermodynamic, and transport properties of silicate perovskite can be significantly affected by the valence and spin state of iron. Silicate perovskite with 5-10 mol% of Fe (where $\text{Fe}^{3+}/\Sigma\text{Fe} \sim 50-75\%$ (McCammon *et al.*,

1997)) and Al, is dominant phase in Earth lower mantle (~75 vol%) (Zhang *et al.*, 2006; Stackhouse *et al.*, 2007). The behavior of Fe electronic properties under conditions close to those of the Earths lower mantle remains strongly controversial.

The second part of my Ph.D. work is dedicated to an investigation of the spin state of iron in Fe³⁺- rich silicate perovskite at high pressure. Four different silicate perovskite samples with different stoichiometry were studied using the Synchrotron Mössbauer Source. SMS spectra were collected at room temperature and pressures up to 122 GPa using diamond anvil cells, with or without laser annealing of the samples.

The hyperfine parameters, i.e., centre shift and quadrupole splitting, for the same phases, which were extracted from measured spectra for all perovskite samples studied in this work, are the same at each pressure within experimental error. Moreover, there is no change in Fe³⁺/ΣFe for individual samples over the entire pressure range of the experiment. The hyperfine parameters of the Fe³⁺ doublet are consistent with the high-spin state (Gütlich *et al.*, 2011), and their smooth variation with pressure indicates that Fe³⁺ does not undergo spin crossover within the entire pressure range. All observed changes in the spectra are associated with abrupt changes in the electronic state of Fe²⁺. The hyperfine parameters of the low QS Fe²⁺ doublet correspond to the high-spin state (McCammon *et al.*, 2008), while the doublet with high quadrupole splitting, whose intensity grows with pressure at the expense of the Fe²⁺ high-spin state, corresponds either to intermediate-spin (IS) Fe²⁺ (McCammon *et al.*, 2008) or a distortion of the site occupied by high-spin Fe²⁺ (Hsu *et al.*, 2010). Based on results presented in a work of Narygina (2010), we indentify changes in Fe²⁺ electronic structure as high-spin to intermediate spin transition. Irrespective of the interpretation of the Fe²⁺ spin state, conclusions regarding the absence of spin crossover in Fe³⁺ remain valid.

These results show that the previously reported spin crossover of Fe³⁺ ions does not occur when Fe³⁺ occupies the A-site. In both alumina-containing and alumina-free silicate perovskites Fe³⁺ ions remain in the high-spin state up to at least 122 GPa, i.e., almost up to the pressure corresponding to the lower mantle - outer core boundary. The results also indicate that Fe³⁺ ions do not diffuse from the A-site to the B-site in perovskite after high-temperature annealing at high pressure, Mössbauer spectra of before and after annealing are identical. There is also no evidence for high-spin to low-spin crossover of Fe³⁺ ions due to site change. In contrast, the results confirm that Fe²⁺ ions undergo a transition from a high-spin to an intermediate spin state, without reaching a low-spin state within the studied pressure range at room temperature. These results suggest that the seismic velocity anomalies in the lower mantle cannot be attributed to spin crossover in Fe³⁺.

1. Introduction

Knowledge of the Earth's structure, composition and dynamics is crucial for tracing of the planet's evolution and understanding of the global geological processes. At the moment a general, internally consistent model of the Earth exists. Even though minor feature is still a need to be clarified, model is generally accepted by scientific community. The model of the Earth is constructed based upon data from cosmochemistry (element composition), physical chemistry (phase equilibrium) and planetary formation model. Hereby acquired model is constrained by seismological studies, which is independent source of information on densities, general structure and speed of seismic velocities in the Earth. Combination of data obtained from these sources lies in the background of a mineralogical model of the Earth.

1.1 Origin and structure of the Earth.

Solid bodies started to form at least 4.568 billion years ago (Bouvier and Wadhwa, 2010) as a result of the collapse of the nebula, i.e., giant atomic/molecular cloud. Conservation of the angular moment made the cloud rotate faster pushing mass to the center of the rotation. On the other hand, the collapse of the nebula released enormous amounts of energy. The cloud material due to its high radiative opacity absorbed the released energy. Thus, the early stages of the Solar system were extremely hot.

With system cooled, nebula material started to condense. At the first stage, radiation cooling of the nebula material led to condensing of highly refractory compounds - materials with high melting temperature (1850-1400K) (Lewis, 2004). These were lithophile (Ca/Al oxides and silicates) and siderophile compounds (free metals and alloys - W, Ir, Os, Fe, Ni, Co). Due to reducing conditions of the process, metals were condensed almost entirely in metallic form. Major condensation and oxidization of Mg, Si is considered to happen at 1400-1250K with formation of olivine ((Mg,Fe)₂SiO₄ at ~1400 K), and enstatite ((Mg,Fe)SiO₃) at slightly lower temperatures (~1100 K). Atomic sodium and potassium could remain in vapor phase until the completion of the enstatite formation. At temperatures 1250-650 K, Na and K in form of vapor were reacting with Al bearing minerals producing alkali alumina-silicates. Upon further cooling (680-600 K), the first and one of the most important

sulfides FeS was formed. Finally at even lower temperatures, cooling of gases containing highly volatile elements (C, H, O, N) led to their condensation (Palme and Jones, 2003).

The earliest stages of the Solar system formation at present are not well understood. The most widely accepted model of terrestrial planet formation is planetesimal theory (Chambers, 2003). According to the model, in the first stage nebular dust settles to form a relatively dense plane of material from which the planets grow. In the second stage either through gravitational instabilities (Safranov, 1969; Goldreich and Ward, 1973; Goodman and Pindor, 1999) or through the collisions of dust grains, growth of 1-km sized bodies occurs, so-called “planetesimals”. In the third stage of accretion - “runaway growth”, gravity starts to play a role and builds 1-km sized objects into 1000-km sized objects – planetary embryos, the ultimate size of which depends on the amount of available material. It is possible that bodies of the size of Moon or Mars could have formed at this stage (Wetherill and Stewart, 1993). The last stage of accretion - “oligarchic growth” was the slowest and marked by giant collisions between bodies the size of the Moon or Mars (Agnor *et al.*, 1999). Energy released in such massive impacts combined with energy provided by decay of the radioactive isotopes was sufficient to melt some of the protoplanets (partially or completely), which lead to their differentiation (Tonks, 1992; Rubie *et al.*, 2007). The differentiation of the terrestrial planets originates in density difference between the silicates and metal phases and manifests in the depletion of mantle with siderophile elements relative to the original abundances of the Solar system. According to the modern planetary core formation theories, the dense siderophile elements (Fe, Ni, Co, Pt, etc.) were sinking through magma ocean or the partially molten mantle. Differences between the predicted and observed concentrations of the siderophile elements in crust and upper mantle gave birth to several additional hypotheses, namely, metal-silicate equilibration at high pressure and temperature at the base of magma ocean (Murthy, 1991), the 'late-veneer' hypothesis describing addition of material to the Earth's lithosphere by meteor/asteroid bombardment (Kimura *et al.*, 1974; Morgan, 1986), and inefficient core formation with small quantity of iron trapped in the mantle during core formation (Jones and Drake, 1986).

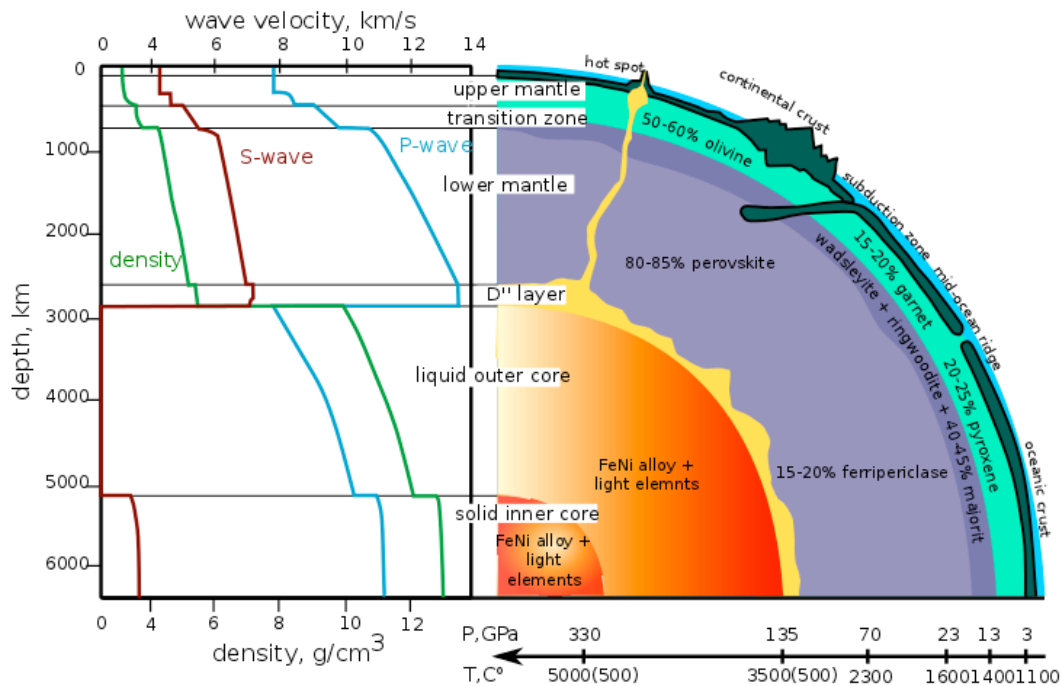


Figure 1.1

Representation of the Earth's inner structure together with density and seismic sound velocity profiles after Dziewonski and Anderson, (1981). The ratio of the major upper/lower mantle minerals are given in volume fractions (Stixrude and Lithgow-Bertelloni 2005a, 2005b) (picture taken from Glazyrin, 2012b)

It is believed that all the terrestrial planets share the same mechanism of a metal core formation and complex crystallization of the magma ocean. Even though each of the planet has gone through its own particular stages of evolution. The Earth is undoubtedly has been studied the most, from all of the terrestrial planets. Direct access to the information on the structure of the Earth comes from the measurements of seismic sound velocities. Combination of seismic measurements with high-pressure experimental research provides necessary information that allows to constrain, to certain extent, Earth's interiors and compositions of the silicate mantle and the core (Figure 1.1).

Mainly two things determine the bulk composition of the Earth: (a) the chemical composition of the solar nebula from which the sun and planets were formed, and (b) the nature of the physical processes that concentrated materials to form the planets. The composition of the sun is similar to the majority of stars in our galaxy, thus the relative abundances of the elements in the sun are referred to as “cosmic abundances”. Additional constraints on the bulk solar nebula composition

come from studies of meteorites, which, being small bodies with a simple history, they provide insight into the early stages of the Solar system evolution. The *chondrites* meteorites are chemically primitive, having compositions similar to that of the sun. The *nonchondritic meteorites* experienced in their history partial (primitive *achondrites*) or entire melting (differentiated *achondrites*). Therefore they to some extent reflect chemical processing similar to that, which affected terrestrial and lunar rocks (Krot *et al.*, 2003). However, only by use cosmic abundances one cannot provide a well-constrained bulk chemical composition of the Earth. One also must to take in to account significant differentiation inside the planet that caused formation of the chemically isolated silicate outer part (crust and mantle) and metallic core. Currently the bulk chemical silicate Earth (crust and mantle) composition is relatively well constrained, although a small scatter between different estimations exist (see Table 1.1) (Palme and O'Neill, 2003).

Table 1.1

Major constituents composition of the bulk silicate Earth according to different estimates (wt.%)

	1	2	3	4	5	6	7	8
MgO	38.1	38.3	36.8	35.5	37.80	37.8	37.77	36.77
Al ₂ O ₃	3.3	4.0	4.1	4.8	4.06	4.4	4.09	4.49
SiO ₂	45.1	45.1	45.6	46.2	45.00	45.0	46.12	45.40
CaO	3.1	3.5	3.5	4.4	3.27	3.5	3.23	3.65
FeO	8.0	7.8	7.5	7.7		8.1	7.49	8.10
Total:	97.6	98.7	97.5	98.6		98.8	98.7	98.41

1 - (Ringwood 1979) 2 - (Jagoutz et al. 1979); 3 - (Wänke et al. 1984); 4 - (Palme and Nickel 1985); 5 - (Hart and - Zindler 1986); 6 - (McDonough and Sun 1995); 7 - (Allègre et al. 1995); 8 - (O'Neill and Palme 2000); All Fe as FeO

Because the core is isolated from the mantle, its chemical composition can be only indirectly estimated based on the global mass balance between the composition of the entire Earth, estimated from cosmic abundances, and the composition of silicate part of the Earth. So the difference between the cosmic abundance of an element and its amount in the silicate part provides a rough estimation of the amount of this element in the core. Modeling of the mineral assemblage of the silicate Earth is

constrained by both its bulk chemical composition (Table 1.1) and seismic profiles, providing the most detailed information regarding the structure of the Earth's interior. Analyses of seismic waves profiles revealed the presence of the two major discontinuities within the mantle: (I) the so-called *transition zone* at a depth from 410 to 660 km, which defines the boundary between the upper and lower mantle; (II) and the D'' *layer* that lies just above the core-mantle boundary (Fig. 1.1). The origin of the mantle discontinuities will be discussed in the following section.

1.2. Mineralogical model of the Mantle. (Mg,Fe)(Si,Al)O₃ perovskite as dominant component of Earth lower mantle.

Even though element composition of mantle is quite homogeneous, the structure of minerals from which is composed gradually change with pressure. At the small depths (<100 km) Earth composed of 4 major phases: olivine, orthopyroxene, clinopyroxene and garnet. In the framework of the popular "pyrolite model" (Ringwood, 1975), it is believed that the (Mg,Fe)₂SiO₄ olivine composes about 60% of the Earth's upper mantle (Fig. 2) and that the nature of mantle heterogeneities are related to the depth-varying behavior of olivine.

The first transition happens at the upper boundary of the transition zone (the layer in the lowermost upper mantle, characterized by anomalous behavior of seismic wave velocities) where (Mg,Fe)₂SiO₄ olivine transforms to its high pressure polymorph – β -phase or wadsleyite with a modified spinel structure, which occurs at around 14 GPa (410-km depth) (Fig. 1.2). Then at about 17 GPa (500-550 km depth) wadsleyite transforms to a more densely packed spinel-structured phase – (Mg,Fe)₂SiO₄ ringwoodite. In turn, ringwoodite disproportionates to (Mg,Fe)SiO₃ perovskite and (Mg,Fe)O ferropericline. This disproportion defines the lower mantle composition and the bottom of transition zone, which is the 660-km discontinuity.

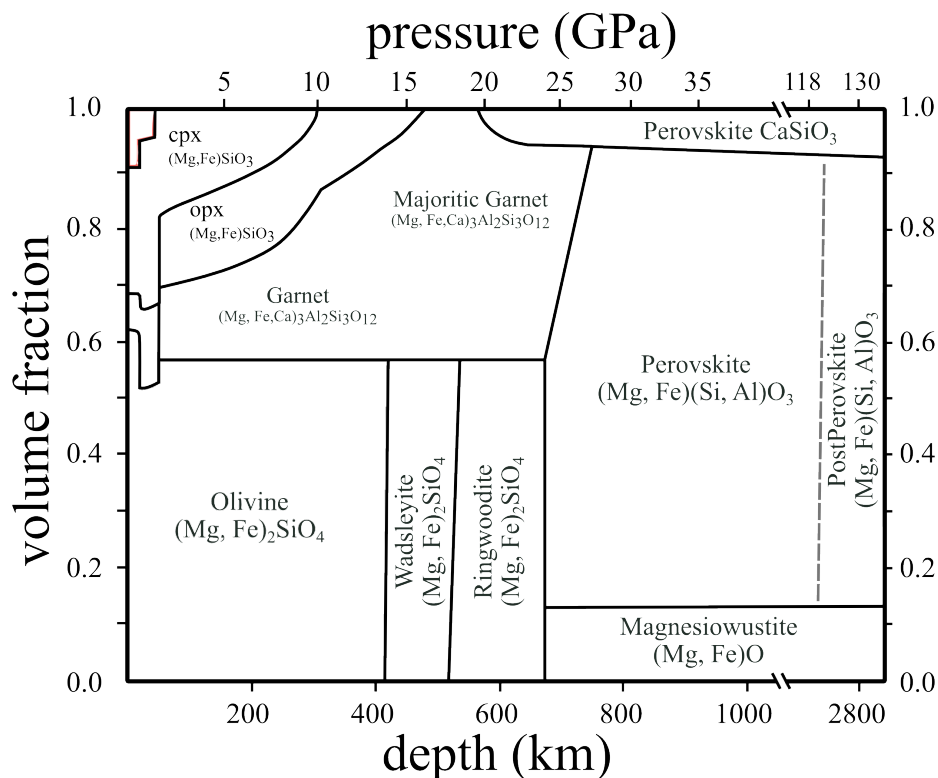


Figure 1.2

Mineral volume fraction of the pyrolite model mantle (Ringwood 1989, 1991; Stixrude and Lithgow-Bertelloni 2005). Opx and cpx are acronyms for orthopyroxene and clinopyroxene respectively. Modified after Frost, (2008).

The remaining non-olivine components (together they make ~40% of upper mantle volume): orthopyroxene, clinopyroxene and garnet, undergo gradual transitions at the depth from 350 to 450 km: pyroxene dissolves in garnet via $\text{MgSi} \rightarrow \text{Al}_2$ substitution, resulting in the formation of Al-depleted garnet (majorite) at pressures above 16 GPa (Irifune and Ringwood, 1987), which eventually also transforms to silicate perovskite (at 23 – 26 GPa or 660 - 750 km depth) with exsolution of Ca-bearing silicate perovskite (Fig. 1.2). Since the dissolution of pyroxenes in garnet is “smeared out” over more than 100 km, it leads to changes in slope of the curves of seismic velocity versus depth rather than causing discrete discontinuities.

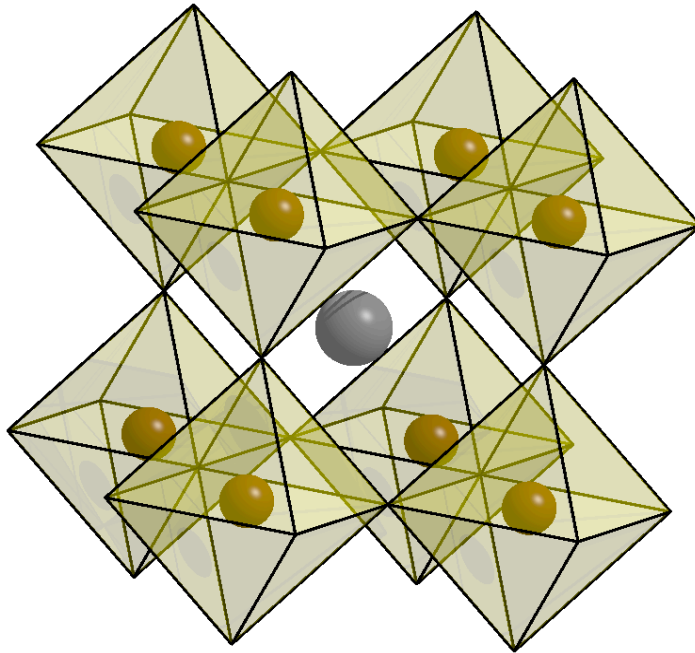


Figure 1.3

Polyhedral models of perovskite (Ross and Hazen, 1989). Big solid grey spheres correspond to $\text{Mg}^{2+}/\text{Fe}^{2+/3+}$ in tetradecahedral site; $\text{Si}^{4+}/\text{Al}^{3+}$ octahedra in the perovskite structure are shown in green.

Summarizing all above, in the lower mantle we have three dominant phases: (Fe,Mg)O ferropericlase, MgSiO_3 silicate perovskite and CaSiO_3 perovskite. After majoritic garnet (the main reservoir of Al in upper mantle), becomes unstable, the perovskite is the main candidate for a phase in lower mantle, which can incorporate Al. Iron in the lower mantle is divided between ferropericlase and silicate perovskite.

Finally, at pressures and temperatures close to those of the core-mantle boundary magnesium silicate perovskite (space group *Pnma*) undergo a structural transition into the post-perovskite phase (space group *Cmcm*) (Murakami *et al.*, 2004). This transition is believed to be “responsible” for the D’ seismic discontinuity at 2600-km depth (Fig. 1.1 and Fig. 1.2).

The iron containing silicate perovskite is a dominant phase in the Earth lower mantle, making ~80% of its volume (almost ~ 48% of entire volume of the Earth). Therefore, this perovskite generally defines lower mantle seismic and density profiles, electrical and thermal conductivity, redox state, etc. Thus understanding of the silicate perovskite properties is critical for construction model of the Earth.

The ideal cubic ABX_3 perovskite crystal structure with space group $Pm3m$ consists of a three-dimensional network of the corner connected octahedra (B-site) and the cavities between the octahedra form the tetradecahedral site (A-site). The lower mantle silicate perovskite has the $GdFeO_3$ structure type, which is distorted from the ideal cubic symmetry by tilting of the octahedra and has the space group $Pnma$ (Horiuchi *et al.*, 1987). It has two sites: the large distorted 8- to 12- fold coordinated A-site predominantly occupied by a Mg^{2+} (big solid grey spheres in Fig. 1.3) (Horiuchi *et al.*, 1987, McCammon *et al.*, 1992); and the smaller nearly symmetrical octahedral B-site predominantly occupied by a Si^{4+} (small colored in green in Fig. 1.3).

Let's look in the more details; so the base composition for the lower mantle perovskite is the $MgSiO_3$ (MgPv), where Mg^{2+} and Si^{4+} cations are balanced by O^{2-} anions. In the lower mantle, it is assumed that the MgPv incorporate Fe (in two states Fe^{3+} and Fe^{2+}) and non-negligible amounts of aluminum. Let's look in the more details how this cations can enter perovskite.

The aluminum ions Al^{3+} due to their small ionic radius (0.53 pm) can enter only the B-site of the silicate perovskite through the Si^{4+} substitution. However, such substitution creates the imbalance in the charge of the system. So it should be coupled with creating of an oxygen vacancy, otherwise a 3+ ion should substitute the Mg^{2+} in the A-site. In case of Fe^{3+} the situation is more complicated. Its ionic radius of 0.63 pm is closer to that of silicon than ionic radius of ferric ions. Thus it was proposed that ferrous iron could enter B-site as well as A-site of MgPv and substitute both Mg^{2+} and Si^{4+} . The Fe^{3+} ion, which enters the A-site, allows the Al^{3+} to enter the B-site without creating oxygen defects in the MgPv. The Fe^{2+} ions can enter the A-site of MgPv substitute the Mg^{2+} one to one. On the other hand, ferrous iron can't enter B-site due to fact that Fe^{2+} ionic radius of 0.77 pm is bigger than 0.4 pm in case of Si^{4+} and because of needs to balance charge of the of system. Several mechanisms for such substitution were proposed, namely, $Mg^{2+}_A + Si^{4+}_B$ to $Fe^{3+}_A + Fe^{3+}_B$, $Mg^{2+}_A + Si^{4+}_B$ to $Fe^{3+}_A + Si^{4+}_B + \square^{2-}$ (oxygen vacancy) and $Mg^{2+}_A + Si^{4+}_B$ to $Fe^{3+}_A + Al^{3+}_B$; where A and B subscripts indicate the corresponding MgPv site. The last mechanism attracts increasing attention as; silicate perovskite with 5-10 mol% of Fe and Al is dominant

phase in Earth lower mantle (~75 vol%) (Zhang *et al.*, 2006; Stackhouse *et al.*, 2007) and it allows for both cations to enter MgPv without creating of the oxygen vacancies which a not energetically favorable under high-pressure.

It was found, that the silicate perovskite in its stability field has considerable amount of the Fe^{3+} , up to $\text{Fe}^{3+}/\Sigma\text{Fe} \sim 50\text{--}75\%$ (McCammon *et al.*, 1997). Enriching of perovskite in Fe^{3+} is believed to be due to the crystal chemistry; in presence of the aluminum iron predominantly is in Fe^{3+} state (McCammon *et al.*, 1997) and not due to oxidation state of the lower mantle (Frost *et al.*, 2004; McCammon *et al.*, 2005). Therefore, the iron/aluminum containing silicate perovskite (FeAlPv) is the most appropriate system to study a role of iron in the lower mantle properties.

Behavior of the iron is different for its various valence state and depends on which crystallographic site it occupies in MgPv. There is no agreement in the pressures of the spin transition of the Fe^{3+} reported by previous studies, broadly a high-spin (HS) (five unpaired d electrons) to low-spin (LS) (one unpaired d electron) transition is predicted when Fe^{3+} occupies the B-site, while Fe^{3+}_A is predicted to remain in the high-spin state at all pressures throughout the lower mantle (Zhang *et al.*, 2006; Stackhouse *et al.*, 2007; Catalli *et al.*, 2010 and 2011; Hsu *et al.*, 2011). Even though Fe^{3+} is predicted to occupy exclusively the A-site in lower mantle compositions of FeAlPv (Vanpeteghem *et al.*, 2006), a HS-LS transition of Fe^{3+} was reported to occur in FeAlPv at high pressure, potentially due to exchange of Fe^{3+} from the A- to the B-site (Catalli *et al.*, 2011; Hsu *et al.*, 2011).

Iron is playing an essential role in the modeling of the lower mantle properties. This transition element influences chemical partitioning and reactions among mantle minerals, as well as thermal, electrical, and mechanical properties at depth (Fyfe, 1960; Burns, 1970; Gaffney and Anderson, 1973; Sherman, 1988; Lin *et al.*, 2005, 2006; Goncharov *et al.*, 2006; Keppler *et al.*, 2007). For example, it was found that presence of the Fe^{3+} could control the radiative conductivity of the perovskite in the lower mantle (Keppler *et al.*, 2007). Already more than 50 years ago, Fyfe (1960) predicted that a spin-pairing transition of iron takes place within the lower mantle. Indeed the transition was experimentally observed in the ferropicriase (Badro *et al.*, 2003; Lin *et al.*, 2005, 2006; Speziale *et al.*, 2005; Kantor *et al.*, 2006a)

and the silicate perovskite (Badro *et al.*, 2004; Jackson *et al.*, 2005; Li *et al.*, 2006). It was found out that these transitions strongly affect an elastic properties of the ferropericlase; for example change of the shear velocities reaches ~4% (Murakami *et al.*, 2012). This indicates that existence of the spin transition of the iron in the MgPv may lead to the change in it share velocities. Thus, existence of a so-called “Spin transition zone” in the lower mantle could explain phenomena like, for example, a small seismic heterogeneities (Hedlin *et al.*, 1997; Kaneshima *et al.*, 1999). The essence of these heterogeneities can also be related to a small fluctuations in a Mg/Fe or a (Mg,Fe)/Si ratios (Bina, 2003). Such a fluctuation can be, in turn, caused by the spin transitions in the lower mantle assemblage (Lin *et al.*, 2007).

The Earth mineralogy model is constrained through comparison of sound velocities obtained in laboratory studies to the seismological data. Recently Murakami *et al.*, (2012) had measured V_s for iron-free MgPv containing Al and compared results to Preliminary Reference Earth Model (PREM). They came to conclusion that the lower mantle on at least 93% consists of the MgPv. So, in the lower mantle a Mg/Si ratio is around 1. Such a high proportion is more consistent with the chondritic mantle model than with conventionally used peridotitic mantle model. Such, chemical stratification implies layered mantle convection with limited mass transport. However, in that study iron free MgPv was studied, such composition does not correspond to the real life composition of the Earth lower mantle. As was stated before the spin transition of the iron in the MgPv could lead to change in the V_s values for it. Thus, determination of the iron state is critical for determination of the correct mantle model, which, in turn would lead to construction of the correct model for the convection in the Earth mantle.

2. Motivation

2.1 Spin state of iron in the lower mantle silicate perovskite

Lower mantle make up to 60% of Earth volume. This makes lower mantle the largest (by volume) entity of the Earth. Thus, it is impossible to construct a reliable model of the Earth without proper understanding of lower mantle properties. It is believed that Earth lower mantle incorporates in average ~10 mol.% of iron in form of Fe^{2+} and Fe^{3+} (Sturhahn *et al.* 2005). Iron is incorporated in two major phases of lower mantle (>90% of it volume, Fig. 1.2): ferropericlase and Al-bearing magnesium silicate perovskite. Thermal and electrical conductivity, and elastic properties of the lower mantle may strongly depend on iron oxidation and electronic state (Xu *et al.* 1998, Lin *et al.* 2005, Kepler *et al.* 2008). Thus, iron is probably the most important transition element in the physics of the Earth. Construction of reliable model of the Earth is impossible without constraining the evolution of iron properties in ferropericlase and silicate perovskite under lower mantle conditions.

The behavior of iron in ferropericlase is well constrained (Kantor *et al.*, 2006, Murakami *et al.*, 2012). On the other hand, reports on behavior of iron in silicate perovskite remain strongly controversial. There are three main reasons to that. First, iron exists in perovskite in two valence states simultaneously (2+ and 3+ valence states). Second, the structure of magnesium silicate perovskite contains two sites, large 8+4 coordination site (“A”) occupied by Mg^{2+} and a smaller octahedral site (“B”) occupied by Si^{4+} . Even through iron expected to reside in the A-site, there are reports, which suggest that Fe^{3+} ions can also enter the B-site (Catalli *et al.* 2010). Third, all iron electronic states and crystallographic environment may depend on pressure and/or temperature. All together make that irons bearing magnesium silicate perovskite extremely challenging system to study spin state of iron in it. Effect of Al on Fe state should be mentioned here as well.

There are several different scenarios describing the spin transition of iron in silicate perovskite:

- 1) Both Fe^{3+} and Fe^{2+} ions undergo a high-spin to low-spin transition (Badro *et al.* 2004).

- 2) Only Fe^{3+} ions located in A-site undergo high spin to low-spin transition (Jackson *et al.* 2005, Zhang *et al.* 2006, Stackhouse *et al.* 2007).
- 3) Fe^{2+} ions undergo high-spin to intermediate spin transition, while Fe^{3+} stay in high-spin state (McCammon *et al.* 2008, Narygina *et al.* 2010, Lin *et al.* 2008).
- 4) Only Fe^{3+} ions located in B-site undergo high spin to low spin transition (Catalli *et al.* 2010).
- 5) Fe^{2+} ions stay in high spin state in lower mantle (Zhang *et al.* 2006, Cohen *et al.* 1997, Li *et al.* 2005), while observed changes in electronic structure of Fe^{2+} ions are explained by crystallographic distortions of the A-site (Lin *et al.* 2012).
- 6) That a Fe^{3+} ions at high-pressure and high-temperature “diffuse” to B-site at the same moment as undergo high spin to low spin transition (Catalli *et al.*, 2011).

There is no agreement on which of these models describes the behavior of iron in the lower mantle.

We have performed the *in situ* measurements of iron hyperfine parameters in iron/alumina bearing silicate perovskite samples with different stoichiometry in a laser-heated diamond anvil cells (DACs) in order to investigate the spin state of Fe^{2+} and Fe^{3+} at conditions of Earth lower mantle, namely, under pressure up to ~ 130 GPa and temperature up to ~ 3500 C°. In order to perform such study and achieve this goal we developed new experimental tool that was set up at ID18 at ESRF – Synchrotron Mössbauer Source, as usually used methods are not very suitable for this kind of experiments.

2.2 Need for energy-domain synchrotron Mössbauer spectroscopy

Behavior of the iron in silicate perovskites under high-pressure can be investigated by many different techniques: X-ray Emission Spectroscopy (XES), Nuclear Forward Scattering (NFS), X-ray absorption near edge structure (XANES) and related X-ray Magnetic Circular Dichroism (XMCD), conventional Mössbauer spectroscopy and X-ray powder and single crystal diffraction (XRD). Unfortunately application of any of these powerful techniques does not allow unambiguous

determination of the spin state of iron in lower mantle perovskite. For example, although XANES is sensitive to ions valence state and XMCD gives an estimate of $\langle L_z \rangle$ and $\langle S_z \rangle$, there are not well suited for the cases when the same element can be found in different valence state and crystallographic sites (like iron in silicate perovskite). XRD is not a direct method for testing of spin state. XES provides information on the bulk on density of electronic states. This makes separation of the individual contributions from ions with different oxidation state and/or crystallographic sites extremely challenging. On the other hand energy domain ^{57}Fe Mössbauer spectroscopy in many cases enables an unambiguous resolution of all hyperfine parameters of ions in different oxidation and electronic states and different crystallographic environment. High-pressure measurements using conventional radioactive point sources encounter several difficulties such as long counting time (generally more than one week per spectrum at ~ 50 GPa pressure range), difficulties to focus the beam, and strong background. All these difficulties greatly reduce the quality of the spectra and thus resolution and sensitivity of the technique. The third generation synchrotron facility offers a solution in the form of time-domain counterpart of conventional Mössbauer spectroscopy (i.e., nuclear forward spectroscopy, NFS). However NFS is not well suited for high-complexity systems, which contain iron nuclei in different spin, valence states and crystallographic sites.

In order to study spin transition in perovskite under lower mantle conditions we have developed an energy-domain synchrotron Mössbauer source. New methodology allows performing of energy domain Mössbauer measurements using synchrotron as a source of gamma radiation. SMS inherits all of the advantages of the conventional Mössbauer spectroscopy and on top of that offers a number of new benefits: high flux, a beam diameter of a few microns and zero background. SMS allows for rapid measurement of energy-domain Mössbauer spectra under extreme conditions with a quality generally sufficient to unambiguously deconvolute even highly complex spectra. These features were successfully demonstrated in our investigation of iron behavior in Al-bearing silicate perovskite under high-pressure.

3. Methods and Instrumentation

3.1. Creation of high pressure

The first experiments with diamond anvil cells were performed in late 50s of the 20th century (Weir et al. 1959). The method has started to gain popularity only after a discovery of a reliable pressure standard in the beginning of 70s (Forman et al. 1972). Since the technique appears it has been constantly evolving, and the number of possible applications increases. Now the list of DAC applications includes measurements of magnetic properties, resistivity, nuclear magnetic resonance, x-ray diffraction, x-ray absorption, optical spectroscopy, conventional Mössbauer spectroscopy, Nuclear Forward Scattering *etc.* (Chervin et al. 1995, Mito et al. 2001, Garg et al. 2004, Haase et al. 2009).

Operation of diamond anvil cell is very simple and can be described as below. The sample chamber is pressurized by application of force on two uni-axially aligned diamonds, this leads to compression of a sample, a pressure transmitting medium and a pressure standard. The force can be applied in various ways. One of the most popular ways is tightening of the screws (Merrill and Bassett 1974) another one is rising pressure in a membrane for the membrane cell (Chevrin et al., 1995). Basic diamond anvil cell (modified after Merrill-Basset design) is shown in Figure 3.1.

In our experiments, two types of DACs were used; they are shown in Figure 3.2. It is the four pin modified Merrill-Basset cell and the piston-cylinder cell, developed in Bayerisches Geoinstitut (BGI). The typical diameter for these cells is Ø50mm and the average height is between 40 and 45 mm.

The upper limit of pressure generated by diamonds depends on two factors, first-on the size of the diamonds culets and second-on the design of diamonds. In practice the simple rule is used: the smaller is diamonds culet size – the higher maximum pressure can be reached. In the works described below, usually diamonds with a culet diameter Ø250-300 µm were employed.

To generate high-pressure without breaking of the diamond anvils several things are important: diamond supporting plates (seats), correct material of the gasket and good mechanical stability of the diamond anvil cell. Design of diamond backing plates depends on experimental technique and its manufacturer. In BGI DACs used for experiment hardened tungsten carbide plates were employed, without any specific

adjustments. As gasket material we used a small pellets ($5 \times 5 \times 0.2$ mm) made from rhenium metal bars. Rhenium gaskets are less compressible than steel gaskets and allow to reach higher pressures without inducing extremely nonhydrostatic conditions. On top of that they do not have iron impurities. This is a very important criterion for ^{57}Fe Mössbauer absorption experiments. Bodies of DAC used in the experiment were prepared from Republica or Nimonic alloys.

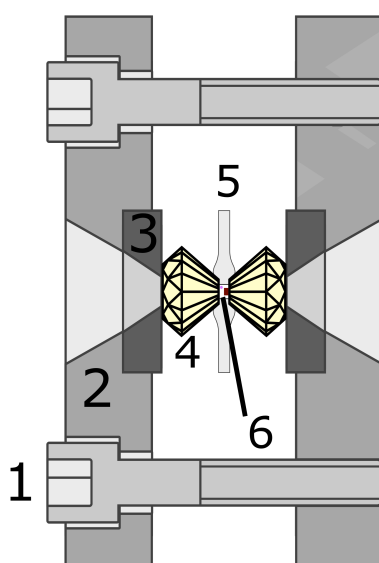


Figure 3.1.1

Schematic diagram of a four-pin modified Merrill-Basset DAC. Diamonds fixed to metallic plates pressurize sample chamber. 1 - screws, 2 - backing plate, 3 - seat, 4 - diamond, 5 - gasket, 6 - sample volume.

One of the most crucial stages of DAC preparation is an alignment of diamonds to a common axis, perpendicular to a culet plane. Relatively small tilt between diamonds culets can lead to destruction of diamond anvils at pressures lower than expected. Next step is a gasket preparation. First it is preindented by diamonds to a thickness of around $\sim 30\text{-}40$ μm . Making a hole in the gasket with electro-discharge-machine (EDM) or laser drill follows the preindentation. This hole serves as a sample chamber.

The size of the hole should be around a half of the diamond culet size. Then, the whole setup including the DAC body with the installed and aligned diamonds, and the gasket is assembled together. Finally, a sample material and pressure standard

(ruby chips (Mao et al. 1986), gold, platinum, NaCl powders, etc. (Fei et al. 2007a)) is loaded into the sample chamber of the gasket. For Mössbauer experiments, normally, a ruby chips were used (for more details see Chapter 5). Pressure generated by diamonds is transmitted to a sample through a pressure medium.

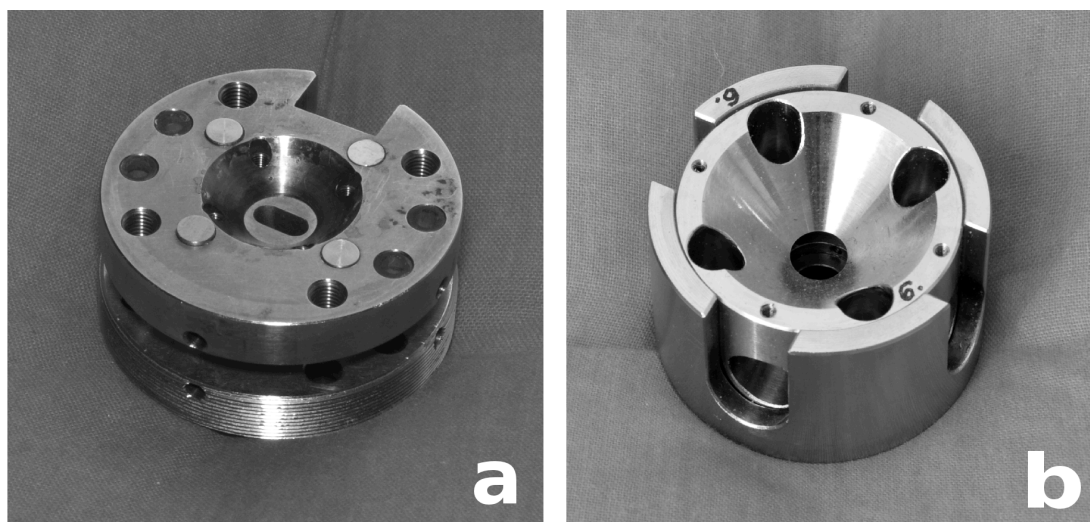


Figure 3.1.2

The diamond anvil cells used in the experiment (a) four pin modified Merrill-Basset cell (b) piston-cylinder cell developed at Bayerisches Geoinstitut.

Excluding some specific cases, the choice of the pressure medium is very important. All of the available pressures transmitting media have their advantages and disadvantages. Usually, the most important criteria is hydrostaticity of a pressure medium (Klotz et al. 2009). For experiments with DACs reported below we used the most hydrostatic pressure transmitting media (Ne or He), loaded into diamond anvil cells at 1-1.5 kbar by a gas loading system installed at BGI (Kurnosov et al. 2008).

3.2. Mössbauer spectroscopy

Experimental results presented in this work were mainly obtained by the energy-domain Mossbauer spectroscopy. Mossbauer spectroscopy is based on the effect of recoilless emission and absorption of γ -photons in solid state (Mössbauer, 1958). If the γ -photon falling to the nuclei has the energy, which exactly coincides

with energy gap between ground and excited states of the nuclei, it can be absorbed and absorbing nucleus would be transformed to its excited state. On the other hand, atom can return to ground state through emission of γ -photon energy exactly equal to energy difference between excited and ground states. Therefore, the measured resonance line absorption/emission position gives directly the energy difference between the different nuclear levels. This resonance process is only possible in absence of recoil. The factor f , which is also known as Lamb-Mössbauer factor, denotes the *recoil free fraction*, i.e., the fraction of emission or absorption occurring without recoil. (f in fact is an equivalent of Debye-Waller factor for Bragg X-ray scattering by periodic lattice.) The recoil-free fraction can be given in terms of the γ -energy E_γ and the *local* mean square displacement of nucleus from equilibrium positions:

$$f = \exp\left[-\langle \chi^2 \rangle E_\gamma^2 / (hc)^2\right] \quad (3.1)$$

where $\langle \chi^2 \rangle$ is a mean square displacement, i.e., the expectation value of the vibrational amplitude in the direction of γ -propagation (Gütlich *et al.* 2011) The Lamb-Mössbauer factor depends on the square of the γ -energy. This in fact limits the choice of the isotopes available for Mössbauer spectroscopy. It was found that value of f factors for nuclei with excited states energies beyond 0.2 MeV is prohibitively small.

The Mössbauer absorption spectrum is mainly characterized by following hyperfine parameters: central shift, quadrupole splitting and hyperfine magnetic splitting.

Central shift (CS) is a shift from zero velocity arises from the sum of Isomer shift and second-order Doppler shift. Isomer shift (δ) is product of interaction between nuclear charge distribution ZeR^2 (R^2 is a mean square radius of nucleus) and the electronic charge density $e|\psi(0)|^2$ at the nuclei. The value of isomer shift allows to identify the spin state, valence state and under normal circumstances the coordination number pertaining to particular iron state. The second-order Doppler shift (δ_{SOD}) is an effect that results from relativistic shift of the energy of the γ -photon due to the thermal motions of the emitting and absorbing nuclei. From its

value one can extract the difference in temperatures between the source of the γ -photon and the absorber (Gütlich *et al.* 2011).

The *quadrupole splitting* (QS) arises from interaction of nuclear quadrupole moment for a given quantum number and the electric field gradient (EFG), which is produced by electrons of the Mössbauer atom and the surrounding charges of ligands. QS is a parameter of immense importance for chemical applications of the Mössbauer effect. It provides information about bond properties and local symmetry of the Mössbauer nuclei site. QS can provide information on the energy splitting between valence electron levels (Ingalls, 1964; Huggins, 1975).

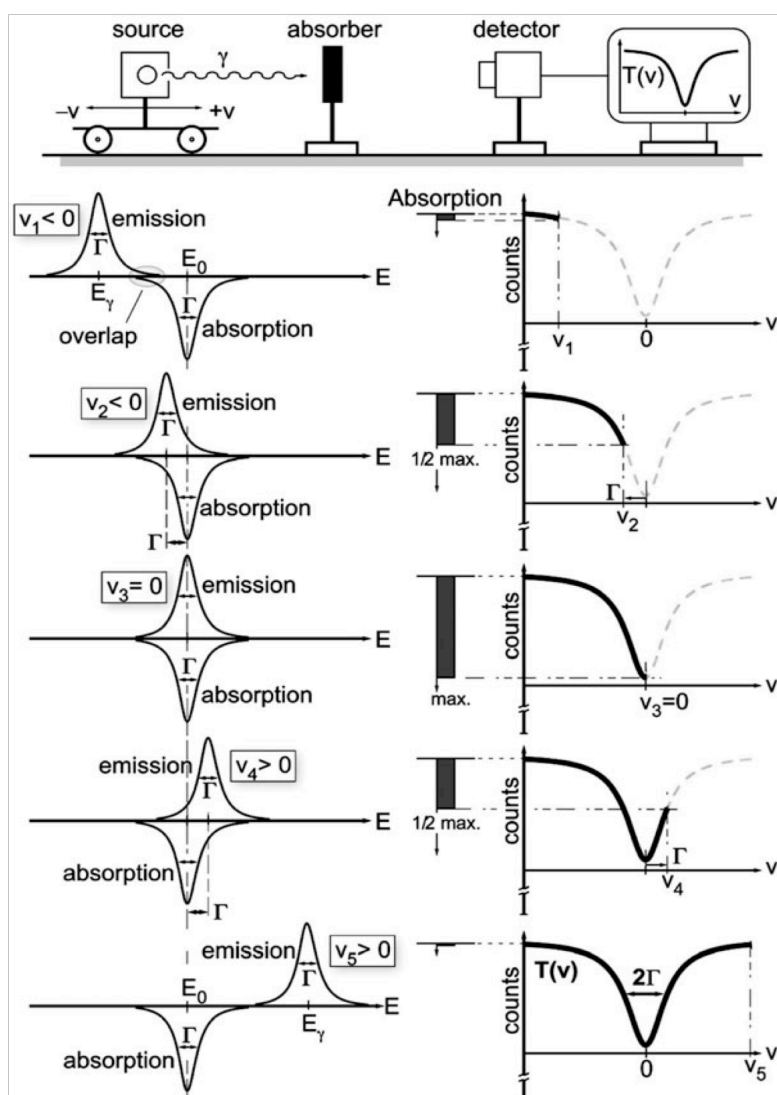


Figure 3.2.1

Schematic illustration of a Mössbauer transmission experiment in five steps. The “Absorption” bars indicate the strength of recoilless nuclear resonant absorption as determined by the “overlap” of emission and absorption lines when the emission line is shifted by Doppler modulation (velocities v_1, \dots, v_5). The transmission spectrum $T(v)$ is usually normalized to the transmission $T(\infty)$ observed for $v \rightarrow \infty$ by dividing $T(v)/T(\infty)$ (taken from Gütlich *et al.* 2011).

The *hyperfine magnetic splitting* arises from interaction between nuclear magnetic dipole moment and surrounding magnetic field. It can provide information about system magnetic ordering and strength of the magnetic exchange interactions between atoms.

All these parameters depend on the valence and the spin state of the Mössbauer atom. This in combination with high sensitivity of the Mössbauer spectroscopy allows for clear distinguishing and separation of contribution from different sites of Mössbauer atom (in our case iron).

There are other parameters, which characterize the Mössbauer spectrum *linewidth* and *relative area* of individual subspectra. Their analysis can give additional information about sample. Mössbauer spectroscopy is extremely powerful technique that, for example, allows for precise measurements of the redox ratio, and also provides the opportunity to study the behavior of iron species separately.

Most of the Mössbauer measurements presented in here were obtained using energy-domain Synchrotron Mössbauer Source, which was developed during this Ph.D. thesis. Detailed description of the SMS construction and basic physics behind it is in presented in Chapters 5.1-5.3. For sample characterization in this thesis also conventional Mössbauer spectroscopy was used. Measurements were performed using standard BGI setup for Mössbauer spectroscopy.

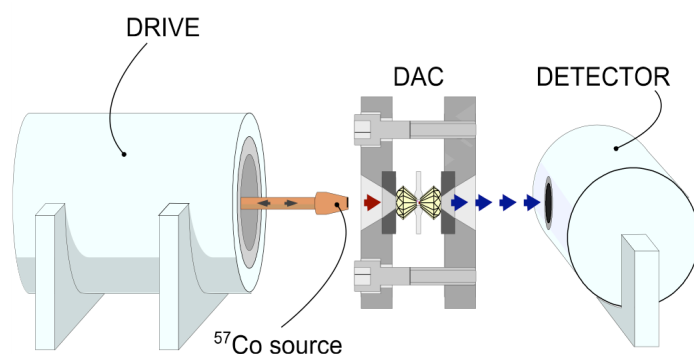


Figure 3.2.2

Schematic drawing of the experimental setup for conventional Mössbauer spectroscopic measurements in the DAC at BGI (from Glazyrin, 2012b).

Due to the μm -thickness of a sample enclosed in a DAC and low iron content, all samples used for DAC experiments were enriched in ^{57}Fe . The velocity scale was calibrated relative to 25 μm Fe foil. The average duration of a single run was 24-48 h in case of conventional measurements and from 10 to 30 minutes in case of SMS. The conventional spectra were fitted to Lorentzian lineshapes using NORMOS (Brand, 1990) and Recoil (Lagarec and Rancourt, 1998) program packages. The SMS Mössbauer spectra were fitted using in-house developed fitting package.

4. Synopsis (Scope of the Thesis)

This chapter provides a summary of the results presented in five papers comprising the Chapter 5. This chapter is organized in following way: Subsection 4.1 is dedicated to theoretical and experimental investigation of angular, energy and temporal properties of pure nuclear reflection of iron borate crystals near its Néel temperature. In subsection 4.2 we present a description of SMS developing and examples of its application beyond high-pressure physics. Subsection 4.3 contains report on spin state of Fe^{3+} ions in perovskite under lower mantle conditions. Finally, in section 4.4 combination of SMS with portable double-sided laser system is described. This combination allows us to perform energy-domain Mössbauer measurements under high-pressure and high-temperature extreme conditions simultaneously.

I wrote three out of five papers presented in Chapter 5 as a first author. For them I had prepared and conducted all experiments, analyzed the data, and performed calculations. I had developed the Synchrotron Mössbauer Source in close collaboration with other coauthors. I had also written the text of the publications (alone or with advices other co-authors) In percents my contribution to Chapters 5.2 and 5.3 is 80% and to 5.4 is 75%. Two manuscripts (Sections 5.1, 5.5) were not written by me as a first author. For the paper described in Section 5.1 I had participate in calculations, data analysis, and text preparations. My total contribution to the paper is around 45%. For fifth paper described in Chapter 5.5 I have prepared and conducted laser-heating experiments with SMS, acquired and analyzed measured spectra, and contributed to the paper preparation, which make my contribution on the level of 33%.

4.1 Theoretical calculation and experimental study of angular dependence, energy and temporal distributions of synchrotron-based ^{57}Fe Mössbauer radiation

We had performed a theoretical calculation of the angular dependences and energy, temporal distributions for pure nuclear reflections in crystal of iron borate

($^{57}\text{FeBO}_3$) at various values of internal magnetic field. These calculations were performed in order to look at the behavior of these distributions while internal magnetic field approaching it collapse, which happens at Néel point. It was found that following the collapse of the internal magnetic field angular dependence of the reflected radiation (rocking curve) becomes significantly broader and change its shape from Gaussian-like to complex structure with two peaks (Fig. 4.1.2-a). On the other hand, energy and time distributions demonstrate strong angular dependence. Only in angular position of the minimum between two peaks (which corresponds to exact value of the Bragg angle) energy distribution consists from just one line (hereafter main line). Outside of this narrow angular region, the main line is accompanied by satellites (Fig. 4.1.1-b). In the region of the lower angle satellite has a lower energy than main line, in the region of higher angles satellite energy is slightly higher. An analysis of time distributions gives (Fig. 4.1.3) an additional insight at the involved processes. The non-exponential decay shape of time distributions in angular position of the minimum reveals a true nature of the main line, which was obtained near the Néel point. In fact this is pseudosingle line formed as the result of the collapse of the hyperfine magnetic structure of nuclear levels. In this particular case, the time distribution follows such dependence:

$$I(t) \propto t^2 \exp(-t/\tau), \quad (4.1.1)$$

where τ – lifetime of the level in the excited state, t – time, $I(t)$ – intensity. The Eq. (4.1.1) actually is a module of the Fourier transform taken from following equation (in limit of $\Delta \rightarrow 0$):

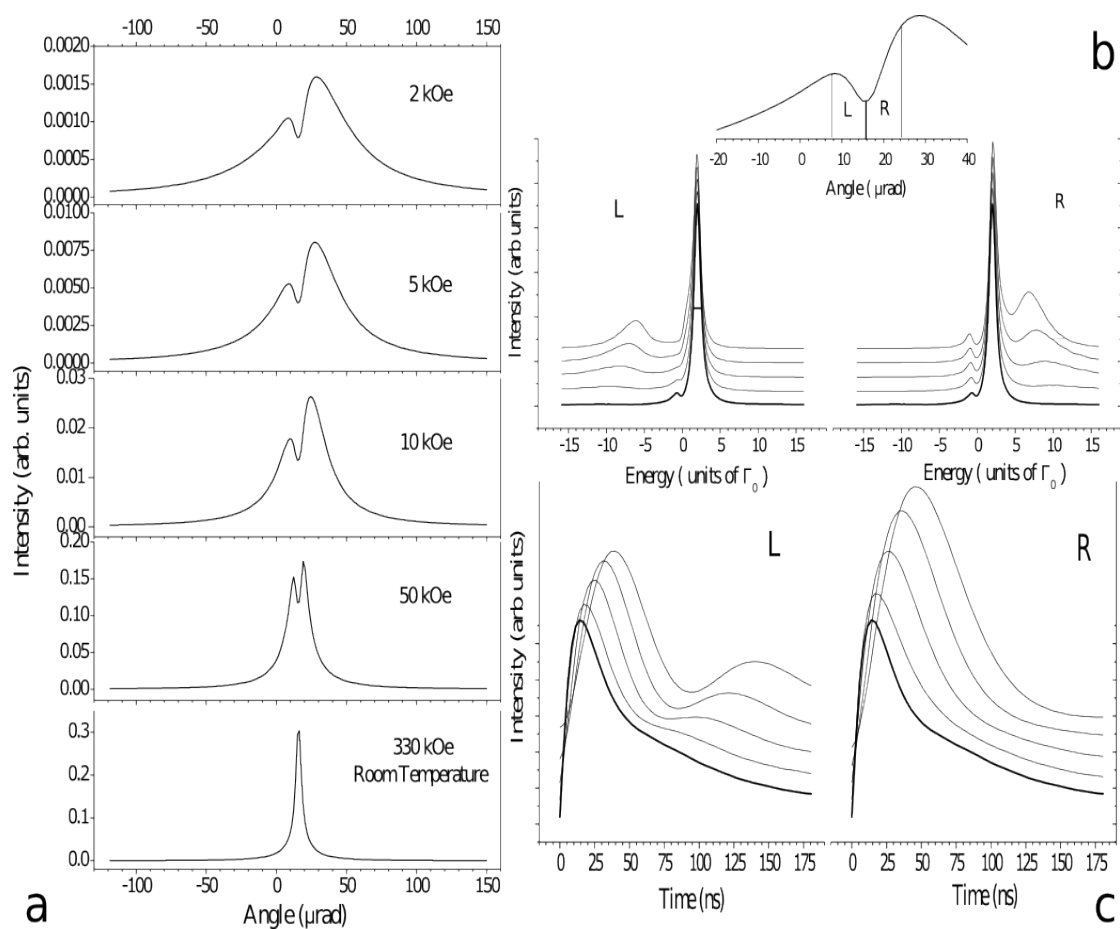
$$A(E) = \frac{1}{E - \frac{\Delta}{2} - i\frac{\Gamma}{2}} - \frac{1}{E + \frac{\Delta}{2} - i\frac{\Gamma}{2}}, \quad (4.1.2)$$

where $A(E)$ – amplitude of the scattered wave, Δ – difference in energy between two lines, Γ – width of the line ($\tau \times \Gamma \approx \hbar$). The Eq. (4.1.2) describes interference between two Lorentzian lines with opposite sign. In first approximation, the module taken from of Eq. (4.1.2) at the limit of $\Delta \rightarrow 0$ describes the main line (which is our pseudosingle line) and in the first approximation followed squared Lorentzian distribution:

$$L^2(E) \propto \left(\frac{\Gamma}{(E - E_0)^2 + (\Gamma)^2} \right)^2, \quad (4.1.3)$$

where E – energy, E_0 – a value of resonance energy, $L(E)$ – intensity.

The results of the experiments performed in almost perfect conditions (high-quality iron borate crystal, very small divergence of the incident beam *etc.*) are in very good agreement with theoretical predictions. Indeed in vicinity of Néel temperature, the width of the crystal rocking curve becomes significantly broader and rocking curve changes its shape from Gaussian-like to complicated structure with two peaks (Figure 4.1.2). Furthermore, the angular and time distributions acquired a strong angular dependence (Figure 4.1.3). As predicted, in the angular region in the minimum between two peaks of rocking curve the energy distribution consist of only one main line free of satellites. The full width at half maximum (FWHM) of this line is of ~ 10 neV ($2\Gamma_0$). Analysis of time distribution showed that the distribution obtained in the minimum angular position can be fitted using Eq. 4.1.1 (Figure 4.1.3-2b). Thus, in first approximation the experimentally obtained main line obeys squared Lorentzian distribution.

**Figure 4.1.1**

Calculated angular, energy and temporal distributions for (333) pure nuclear reflections of iron borate crystal. (a) – Rocking curves calculated with different value of internal magnetic field. Energy and temporal distribution was calculated for value of the external magnetic field equal to 2kOe. The dip zone (taken from Fig.4.1.1a) is shown on the upper panel on Fig. 4.1.1b. The energy and time distributions on the lower panels refer to the left and the right sides of the dip zone, L and R respectively, as shown on the upper panel. The energy and time distributions at the exact dip position are displayed on both L and R panels (bold line curves). Each next distribution corresponds to an angular shift of the crystal from the dip position by 5 μrad . For better visualization the energy and time distributions are equally spaced along the vertical axis. (b) – Energy distributions at different angular position. Only in the angular position, which corresponds to the exact Bragg angle, main line is practically free from satellites. (c) – Temporal distributions at angular positions at which energy distributions was calculated.

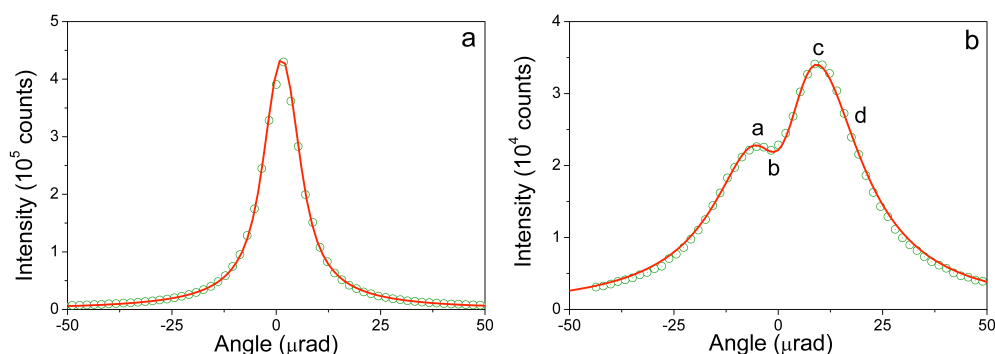


Figure 4.1.2

Angular dependence of the reflected radiation for iron borate (333) pure nuclear reflection of IB crystal (a) at RT (b) 348.9 K. Circles show experimental points, solid line shows theoretical fit. On panel b letters (from a to d) mark angular position of the crystal relative to the incident beam in which energy and time distribution was measured.

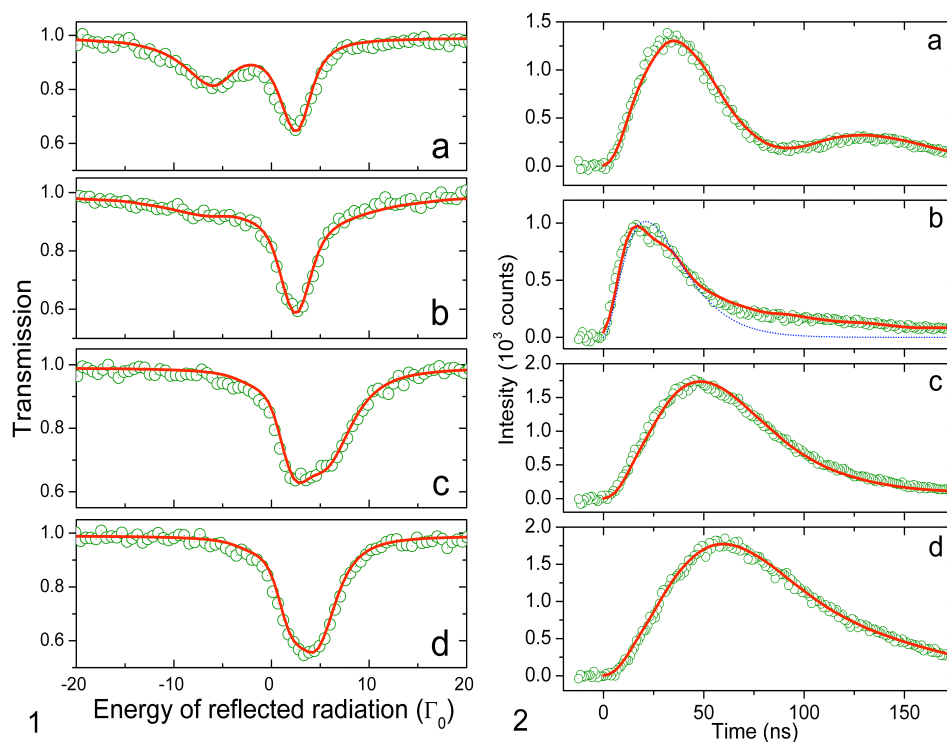


Figure 4.1.3

Measured Energy and time distributions of nuclear Bragg diffraction for iron borate (333) reflection. **[1]** - Energy distributions of nuclear Bragg diffraction for iron borate (333) reflection measured in different angular position of the crystal relative to the incident beam. Olive circles - experimental points, red line - theoretical fit. Energy distribution was measured using standard Mössbauer $K_2Mg^{57}Fe(CN)_6$ single line absorber. **[2]** - Time distributions of nuclear Bragg diffraction for iron borate (333) reflection measured in different angular position of the crystal relative to the incident beam. Olive circles shows experimental points, red line - theoretical fit, blue dash line shows fit to data using Eq. 4.1.1. Measurements performed at four angular positions (4.1.2b): small peak (a), minimum (b), big peak (c) and the right slope of the big peak (d).

4.2 The ^{57}Fe Synchrotron Mössbauer Source

Using results summarized in Section 4.1 (Chapters 5.1 and 5.2) we design a ^{57}Fe Synchrotron Mössbauer Source. It allows to perform energy-domain Mössbauer measurements using synchrotron radiation. The SMS is based on pure nuclear reflection of an iron borate crystal ($^{57}\text{FeBO}_3$). Figure 4.2.1 shows the optical scheme for high-pressure experiment with a DAC using the SMS based on (333) pure nuclear reflection. The SMS is the in-line monochromator, i.e., the beam emitted by the source is directed almost exactly along the synchrotron radiation beam from high-heatload monochromator. We developed design for two in-line optical schemes based on (111) and (333) pure nuclear reflections of the $^{57}\text{FeBO}_3$.

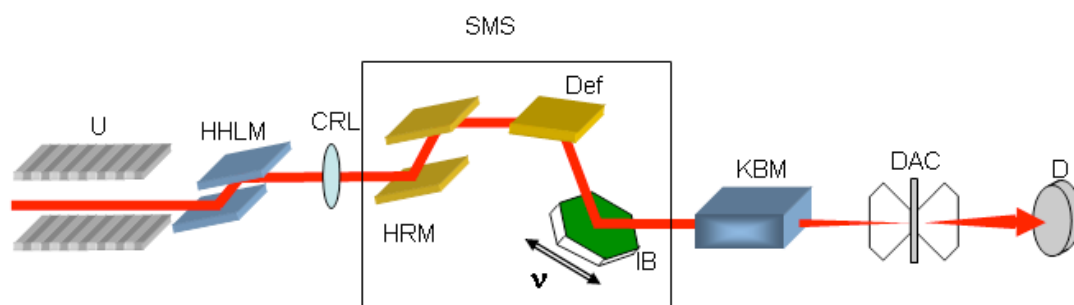


Figure 4.2.1

The optical scheme for a high-pressure experiment with DAC using the Synchrotron Mössbauer Source based on the (333) pure nuclear reflection. U – undulator; HHLM – high-heat-load monochromator; CRL – compound refractive lens; SMS – the Synchrotron Mössbauer Source; HRM – high resolution monochromator, Def – Si (311) deflector, IB – the iron borate crystal inside the furnace with the four magnets and mounted on the Mössbauer transducer; KBM - Kirkpatrick-Baez mirrors; DAC – diamond anvil cell; D – avalanche photo diode detector.

The SMS is optimized for highest intensity and best energy resolution, which is achieved by collimation of the incident synchrotron radiation beam and thus illumination of the high-quality iron borate crystal within a narrow angular range around an optimal position of the rocking curve. The SMS is permanently located in an optics hutch and is operational immediately after moving it into the incident beam.

The bandwidth of radiation provided by the SMS is $\sim 3 \Gamma_0$ or ~ 15 neV (in real experiments we work with energy resolution lower than possible to have more intensity), the intensity is $\sim 2 \times 10^4$ photons/s and the typical scanning velocity range is about ± 12 mm/s (± 0.6 μeV). In contrast to conventional radioactive sources, the SMS gives the possibility to focus the beam to tens of μm (the best achieved by now is 9×6

μm^2). As in-line monochromator SMS can be used with all existing sample environments in the experimental hutches downstream of the beamline.

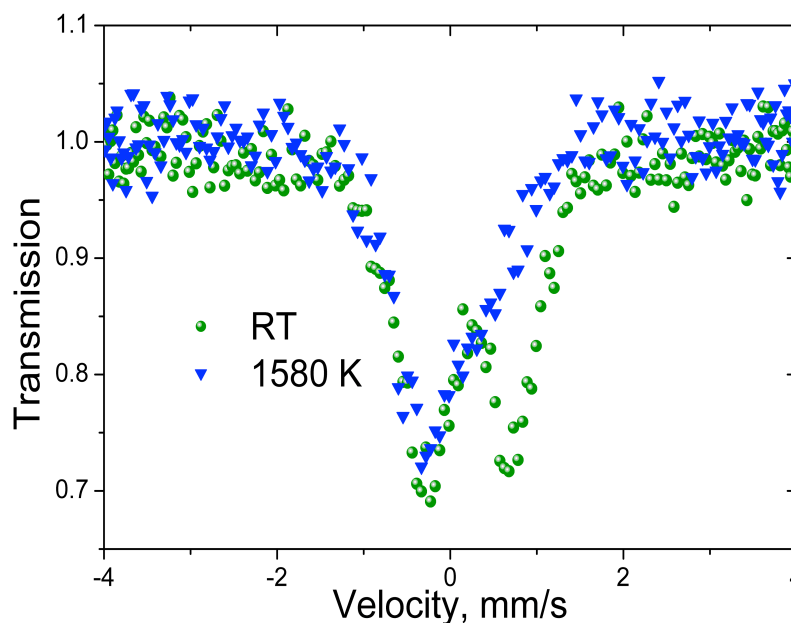


Figure 4.2.2

Spectra of $(\text{Mg}_{0.8}\text{Fe}_{0.2})\text{O}$ ferropericlase at a pressure of 29 GPa at room temperature (green circles) and at 1580 K (blue triangles).

I implemented SMS in order to study electronic properties of materials under high-pressure extreme conditions. One of the biggest SMS advantages is that it allows collecting spectra rapidly, on the scale of several minutes. For example, a high-quality Mössbauer spectrum of the silicate perovskite sample in the DAC at 93 GPa was acquired for about 10 min, compared to more than one week using a radioactive point source for the same sample. This, in combination with possibility to focus beam produced by SMS, enables to perform high-temperature studies using laser heating (Figure 4.2.2). The almost 100% recoilless resonant radiation delivered by the source and its high brightness allows a broad field of SMS applications. Due to a very strong suppression of electronic scattering for pure nuclear reflections ($\sim 10^{-9}$) SMS operation does not required any gating of the prompt electronic scattering. Thus, SMS can be utilized in any mode of storage ring operation.

In this work SMS was used to study of the spin transition in Fe^{3+} ions in iron containing silicate perovskite, which is the dominant phase of the lower mantle of the Earth (by most recent reports ~93% (Murakami *et al.*)).

4.3 Spin state of Fe^{3+} ions in the lower mantle

Using developed energy domain synchrotron Mossbauer source we conducted a study of several iron containing silicate perovskite samples (both Al containing and Al-free). We have studied four different silicate perovskite samples: $\text{Mg}_{0.63}\text{Fe}_{0.37}\text{Si}_{0.63}\text{Al}_{0.37}\text{O}_3$ (~80% $\text{Fe}^{3+}/\Sigma\text{Fe}$); $\text{Mg}_{0.63}\text{Fe}_{0.37}\text{Si}_{0.63}\text{Al}_{0.37}\text{O}_3$ (~70% $\text{Fe}^{3+}/\Sigma\text{Fe}$); $\text{Mg}_{0.78}\text{Fe}_{0.2}\text{Al}_{0.05}\text{Si}_{0.97}\text{O}_{3+\delta}$ (~50% $\text{Fe}^{3+}/\Sigma\text{Fe}$); $\text{Mg}_{0.94}\text{Fe}_{0.06}\text{SiO}_{3+\delta}$ (~20% $\text{Fe}^{3+}/\Sigma\text{Fe}$). In our experiments SMS spectra at room temperature were collected up to 122 GPa using diamond anvil cells, with or without laser annealing of the samples. Details of sample synthesis and experiment methodology are given Section 5.4.

First, energy-domain Mössbauer study of $\text{Mg}_{0.63}\text{Fe}_{0.37}\text{Si}_{0.63}\text{Al}_{0.37}\text{O}_3$ perovskite was performed. It contains iron dominantly as Fe^{3+} , measured spectra are extremely well resolved (Fig. 4.3.1). We fit the data using model that consist of three quadrupole doublets, one assigned to Fe^{3+} and two assigned to Fe^{2+} (high and low quadrupole splitting, QS). Unlike in case of NFS studies, SMS allows unambiguously separate contributions for Fe^{3+} and Fe^{2+} based on doublets centre shifts (CS). As it is clear even from visual inspection of Mössbauer spectra (Fig. 4.3.1) there are no changes in the shape and relative area of the doublet corresponding to the Fe^{3+} over the entire pressure range.

The hyperfine parameters of the low QS Fe^{2+} doublet (blue doublet in Fig. 4.3.1) corresponds to the high-spin state (McCammon *et al.*, 2008), while the doublet with high quadrupole splitting (black doublet in Fig. 4.3.1) corresponds either to intermediate-spin (IS) Fe^{2+} (McCammon *et al.*, 2008) or a distortion of the site occupied by high-spin Fe^{2+} (Hsu *et al.*, 2010). Irrespective of the interpretation of the Fe^{2+} spin state, our conclusions regarding the absence of a spin transition in Fe^{3+} remain the same.

The fitting model obtained for sample #1 spectra was implemented for all other samples. The hyperfine parameters for Fe^{2+} and Fe^{3+} for all samples studied are

the same within experimental error. Moreover there is no change in $\text{Fe}^{3+}/\Sigma\text{Fe}$ for individual samples over the entire pressure range of the experiment (Fig. 4.3.2). The hyperfine parameters of the Fe^{3+} doublet are consistent with the high-spin state (Greenwood and Gibbs, 1971), and their smooth variation with pressure indicates that Fe^{3+} does not undergo any spin transitions within the entire pressure range. Notably the QS value reported for low-spin Fe^{3+} from both experimental (Catalli *et al.*, 2010; Catalli *et al.*, 2011) and theoretical (Hsu *et al.*, 2011) studies (red dashed line, Fig. 4.3.2) are more than twice our observed values.

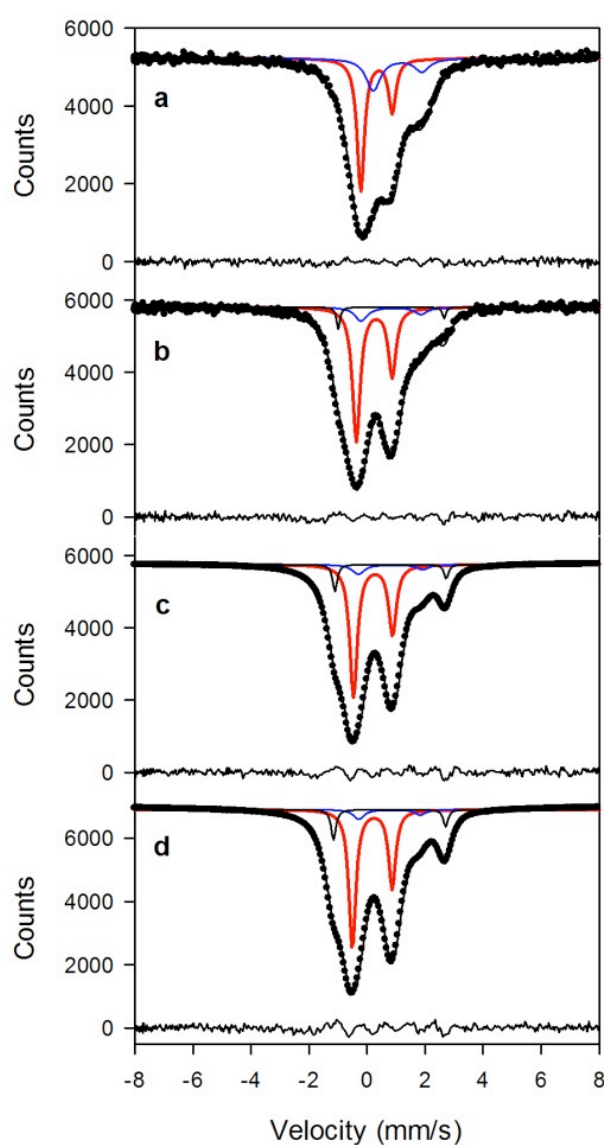


Fig. 4.3.1

SMS spectra of $\text{Mg}_{0.63}\text{Fe}_{0.37}\text{Si}_{0.63}\text{Al}_{0.37}\text{O}_3$ perovskite sample #1 at room temperature showing their evolution with pressure (a) 2.5 GPa; (b) 38 GPa; (c) 67 GPa; (d) 93 GPa. The data were fit to one Fe^{3+} doublet (red) and two Fe^{2+} doublets (blue and black), and the fit residual is shown below each

spectrum. Area asymmetry is due to preferred orientation of the sample, and the velocity scale is given relative to α -iron.

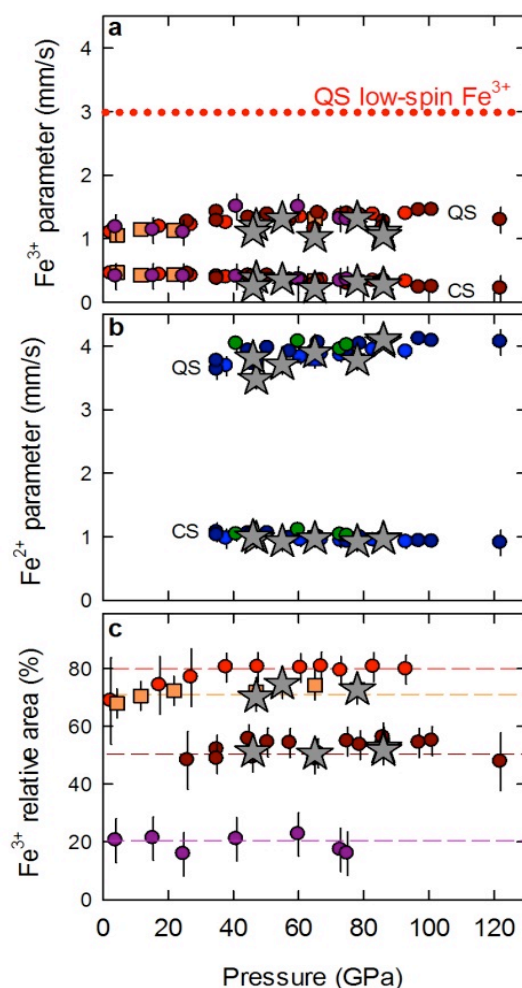


Figure 4.3.2

Pressure variation of FeAlPv hyperfine parameters (centre shift [CS] and quadrupole splitting [QS]) (a) high-spin Fe^{3+} ; (b) high QS Fe^{2+} . Sample data are indicated as follows: $Mg_{0.63}Fe_{0.37}Si_{0.63}Al_{0.37}O_3$ perovskite sample #1 (red and blue circles); $Mg_{0.63}Fe_{0.37}Si_{0.63}Al_{0.37}O_3$ perovskite sample #2 (orange and blue squares); $Mg_{0.78}Fe_{0.2}Al_{0.05}Si_{0.97}O_{3+\delta}$ perovskite (brown and dark blue circles); $Mg_{0.94}Fe_{0.06}SiO_{3+\delta}$ perovskite (purple and green circles). The expected quadrupole splitting for low-spin Fe^{3+} is shown as a horizontal red dashed line. (c) Pressure variation of $Fe^{3+}/\Sigma Fe$ as determined from the relative areas: perovskite sample #1 (red circles); $Mg_{0.63}Fe_{0.37}Si_{0.63}Al_{0.37}O_3$ perovskite sample #2 (orange squares); $Mg_{0.63}Fe_{0.37}Si_{0.63}Al_{0.37}O_3$ perovskite (brown circles); $Mg_{0.94}Fe_{0.06}SiO_{3+\delta}$ perovskite (purple circles). Horizontal lines are guides for the eye. Values obtained after laser heating of $Mg_{0.63}Fe_{0.37}Si_{0.63}Al_{0.37}O_3$ perovskite sample #2 and $Mg_{0.78}Fe_{0.2}Al_{0.05}Si_{0.97}O_{3+\delta}$ perovskite are indicated by grey stars. In all cases, parameters remained unchanged from those before heating within experimental error, demonstrating that there is no high-spin to low-spin transition in Fe^{3+} at the pressure-temperature conditions of the lower mantle

Several studies (Catalli *et al.*, 2010; Catalli *et al.*, 2011; Fujino *et al.*, 2012) have suggested that the reduced volume of LS Fe^{3+}_B could lead to a redistribution of Fe^{3+} from the A- to the B-site in the perovskite structure within the lower mantle. To

test this hypothesis, we laser annealed our samples at a number of pressures and collected SMS spectra both during and after heating. SMS spectra collected during and after laser annealing showed no change to those taken before heating (Chapter 5.4) and hyperfine parameters remain unchanged (star symbols; Fig. 4.3.2).

A final resolution of the controversy surrounding iron spin transitions in iron alumina containing silicate perovskite through Mössbauer spectroscopy (this work) and single crystal X-ray diffraction (Glazyrin *et al.*, 2012) provides an important step in developing quantitative models for joint inversion of electromagnetic and seismic data that place improved constraints on lower mantle mineralogy, composition and thermal state.

4.4 DOUBLE SIDED LASER SYSTEM FOR SMS AND X-RAY DIFFRACTION

The ultimate goal of geophysics is to study Earth interior minerals at conditions close to natural, i.e., under high-pressure and high-temperature conditions simultaneously. Generation of high pressure using DACs was proven to be the most suitable technique for *in-situ* studies, as it covers the whole range of pressures relevant for the Earth's interiors. On the other hand, generation of high temperatures, similar to, for example, temperatures of the lower mantle is a challenging task. External resistive heaters do not allow reaching temperatures above 1000 K due to diamond anvils oxidation. However, the way out was found in combinations of laser heating with generation of high pressure using DACs.

Here we present the development of portable double-sided laser heating system for DACs. It can be mounted on a ~ 0.1 m² area and has a weight of just ~ 12 kg. The system is easily transferable between different in-house or synchrotron facilities and can be assembled and set up during a few hours. We demonstrate application of the system on for examples; first, single crystal X-ray diffraction investigation of $(\text{Mg}_{0.87}, \text{Fe}^{3+}_{0.09}, \text{Fe}^{2+}_{0.04})(\text{Si}_{0.89}, \text{Al}_{0.11})\text{O}_{3+\delta}$ silicate perovskite and second-on an energy-domain Mössbauer spectroscopy study of $(\text{Mg}_{0.8}\text{Fe}_{0.2})\text{O}$ ferropericlae using recently developed Synchrotron Mössbauer Source at high pressures and temperatures. We collected the diffraction data at pressures of 65 GPa to 78 GPa in several sets, namely before, during and after laser heating. Structural

refinements on the integrated intensities converged with values of the R-factors below 5%. We found that (a) the refined amount of iron in the A-site coincides, within uncertainty, with the value determined by microprobe data, (b) laser heating does not affect chemical composition of the silicate perovskite in our experiments, and (c) high temperature does not promote any exchange chemical reactions between the A- and B-sites (i.e. there is no sign of Fe entering the B-site during heating). This is consistent with conclusion made in section 4.3, which was done by independent method. As for SMS studies, the feasibility of energy-domain Mössbauer studies under combination of high-pressure/high-temperature was shown as well as extreme sensitivity of such studies to temperature gradients. Existence of internal temperature calibration in Mossbauer spectroscopy (see Section 3.2 for second-order Doppler shift) makes it perfect instrument for studies under high-temperature extreme condition. Thus, success of the test of SMS/ double-sided laser heating system combination opens rich opportunities, for example, for *in-situ* studies of materials under lower mantle conditions.

4.5 List of manuscripts and statement of author's contribution

[1] G.V. SMIRNOV, A.I. CHUMAKOV, V.B. POTAPKIN, R. RÜFFER, AND S.L. POPOV; MULTISPACE QUANTUM INTERFERENCE IN ^{57}Fe SYNCHROTRON MÖSSBAUER SOURCE; *PHYSICAL REVIEW A* **84** (2011) 053851

G.V. Smirnov (GVS) and A.I. Chumakov (AIC) developed the theoretical formalism. V. Potapkin (VP) and G.V. Smirnov (GVS) performed the calculations. VP, GVS, AIC, R. Ruffer (RR) and S.L. POPOV did analysis of the result. VP, GVS, AVS wrote the manuscript with contributions from other co-authors.

[2] V. POTAPKIN, A.I. CHUMAKOV, G.V. SMIRNOV, R. RÜFFER, C. MCCAMMON, AND L. DUBROVINSKY. ANGULAR, SPECTRAL AND TEMPORAL PROPERTIES OF NUCLEAR RADIATION ^{57}Fe SYNCHROTRON MÖSSBAUER SOURCE. *PHYSICAL REVIEW A* (2012) **86(5)** 053808

The experiments were performed by VP and AIC with a help from L. Dubrovinsky (LD) and C. McCammon (CMcC). VP performed the calculation. VP, AIC, GVS and RR did the analysis of the results. The final interpretation of the results and writing of the manuscript was done by VP, with help from other co-authors.

[3] V. POTAPKIN, A.I. CHUMAKOV, G.V. SMIRNOV, J.-P. CELSE, R. RÜFFER, C. MCCAMMON AND L. DUBROVINSKY. THE ^{57}Fe SYNCHROTRON MÖSSBAUER SOURCE AT THE ESRF; *JOURNAL OF SYNCHROTRON RADIATION* (2012) 19 559-569

The methodology was developed by VP, GVS, AIC and RR. The source design and optical scheme of the device was created by VP and AIC with a help from J.-P. Celse (JPC) and RR. The test of SMS performance and instrument calibration was performed by VP and AIC. The test high-pressure measurements were done by VP, LD, CM and AIC. The VP did final interpretation of the results and wrote the manuscript, with help from other co-authors.

[4] V. POTAPKIN, C. MCCAMMON, L. DUBROVINSKY, K. GLAZYRIN, A. KANTOR, I. KUPENKO, C. PRESCHER, R. SINMYO, G. SMIRNOV, A. CHUMAKOV AND R. RÜFFER, SPIN STATE OF IRON IN LOWER MANTLE; *NATURE COMMUNICATIONS* (2013) **4** 1427.

The SMS methodology was developed by VP, GVS, AIC and RR, and the research project was designed and directed by CM and LD. Samples were synthesized by RS and characterized by VP, RS, KG, LD, and CM. The data were collected by VP, CM, LD, K. Glazyrin (KG), A. Kantor (AK), I. Kупenko (IK), C. Prescher (CP) and AIC. The analysis of SMS was performed by VP, CM and AIC. LD performed the electric conductivity measurements. The VP and CM did final interpretation of the results and wrote the manuscript, with help from other co-authors.

[5] I. KUPENKO, L. DUBROVINSKY, N. DUBROVINSKAIA, C. MCCAMMON, K. GLAZYRIN, E. BYKOVA, T. BOFFA BALLARAN, R. SINMYO, A.I. CHUMAKOV, V. POTAPKIN, A. KANTOR, R. RÜFFER, M. HANFLAND, W. CRICHTON, M. MERLINI, PORTABLE DOUBLE-SIDED LASER-HEATING SYSTEM FOR ENERGY-DOMAIN MÖSSBAUER SPECTROSCOPY AT SYNCHROTRON AND SINGLE CRYSTAL DIFFRACTION EXPERIMENTS WITH DIAMOND ANVIL CELLS; REVIEW SCIENTIFIC INSTRUMENTS (2012) **83** 124501.

The laser-heating methodology was developed by LD, N. Dubrovinskaia (ND), IK, KG. Samples were synthesized by RS and characterized by VP, RS, KG, LD, and CM. The single crystal diffraction data was collected and analyzed by IK, KG, E. Bykova (EB), T. Boffa Ballaran (TBB) M. Hanfland (MH), W. Crichton (WC), M. Merlini (MM). VP did the preparation for SMS experiments. The SMS data were collected by VP, CM, LD, KG, AK, IK, CP, AIC and RR. VP had analyzed the SMS data and had written part of the manuscript dedicated to Synchrotron Mössbauer measurements of the samples under combination of the high-pressure and high-temperature. All authors were involved in the data interpretation. The IK did final assessment of the results and wrote the manuscript with help from other co-authors. VP contributed to the writing of the manuscript.

5. Manuscripts

5.1 Multispace quantum interference in ^{57}Fe synchrotron Mössbauer source

G. V. Smirnov,^{1*} A. I. Chumakov,^{2,1} V. B. Potapkin,^{1,2,3} R. Rüffer,² and S. L. Popov¹

¹*Russian Research Center “Kurchatov Institute”, 123182 Moscow, Russia;*

²*European Synchrotron Radiation Facility, F-38043, Grenoble, France*

³*Bayerisches Geoinstitut, Universität Bayreuth, D-95440 Bayreuth, Germany;*

**-corresponding author*

published in Phys. Rev. A **84** (2011) 053851

5.1.1 Abstract

A physical picture for coherent emission of rays by a nuclear array excited with synchrotron radiation (SR) is given. The particular case of a pure nuclear Bragg reflection from the $^{57}\text{FeBO}_3$ crystal is analyzed. During free de-excitation of the nuclei a nuclear exciton polariton is developing inside the crystal and generates at the exit of the crystal a coherent γ -ray beam. In the crystal the nuclear levels of ^{57}Fe are split because of a combined magnetic and electric interaction. The rich picture of γ -ray interference is described, which involves geometrical space, energy and spin domains. In the vicinity of the Néel temperature of the crystal the magnetic splitting of nuclear levels nearly collapses. These conditions lead to drastic changes in the angular, energy, and temporal properties of the emitted radiation. The emission angular function, which represents the emission intensity for different angular settings of the crystal near Bragg angle - in the approximation of a plane incident wave -, strongly broadens and transforms to a double-hump structure with a central dip in between of the peaks. The energy and temporal distributions of the emitted radiation crucially depend upon the crystal angular setting. Beyond the central dip, the energy distribution of nuclear scattering acquires a complicated form with several satellites at various energies. On the contrary, at the exact angular position of the central dip, the energy spectrum exhibits a single line shape with the line-width close to the natural width of the nuclear resonance. The obtained results constitute the theoretical basis for the understanding and for the further elaboration of the ^{57}Fe Synchrotron

Mössbauer Source - the device which provides a collimated beam of intense and polarized radiation in an energy bandwidth of nano-electronvolts, the nuclear resonance natural level width.

5.1.2 Introduction

Hard x-rays, generated by modern synchrotron radiation (SR) sources, can effectively excite low-lying nuclear metastable states. The short pulses of the x-ray photons provide an almost instantaneous, compared to the lifetime of nuclear state, 'knock-wise' excitation. Under these conditions, the processes of photon absorption and photon emission are two sequential, temporally decoupled, events. At the stage of free de-excitation nuclei of a target generate recoilless γ radiation. This process can serve as an advantageous alternative to a conventional Mössbauer source. The physical nature of these two kinds of sources is, however, absolutely different.

Although in both - the radioisotope and the SR-based source - the same metastable states are excited and the de-excitation of them occurs spontaneously, the excited states are quite different in character and their decay modes differ drastically. In the radioisotope source only one single nucleus is excited at the time and thereafter emits radiation. In the contrary, the excitation of nuclei by a SR pulse and the subsequent nuclear de-excitation are not localized at a single nucleus but spread out over a nuclear ensemble. In fact, each nucleus of the ensemble appears to be excited with a certain probability amplitude. In other words, the excitation is shared by all those nuclei. Such state is referred to as nuclear exciton and can be perceived as a nuclear polarization wave. The initial phase distribution in a nuclear exciton is fully determined by the coherent properties of the transmitted radiation pulse. Typically, it is close to the phase distribution existing in a plane wave.

During de-excitation, each nucleus emits a partial γ -ray wavelet. Since all the wavelets are correlated in phase, their interference leads to the creation of the common coherent wavefield. Inside a crystal, the nuclear polarization wave and the radiation field are tightly coupled and form together a self-consistent dynamical system, called *nuclear exciton polariton or nuclear polariton* (Smirnov *et al.*, 2005; van Burck *et al.*, 2007; Haas, 2007). As the nuclear polariton is developing, a γ -ray photon can be re-absorbed and re-emitted by nuclei several times. At the exit of the

crystal, the nuclear polariton generates a γ -ray beam. The distribution of the emitted γ quanta in time and in space is dictated by the temporal and spatial development of the nuclear polariton, which can exist inside the target in forms of either running or standing wave. The running wave mode is realized in the processes of the forward scattering, while the standing wave pattern is formed for nuclear Bragg reflections. The intensity of γ radiation emitted after each SR pulse is decaying in time. In space, the radiation forms usually the low-divergent beams both in the forward scattering and in Bragg reflection directions (Kagan, *et al.*, 1979).

The delayed resonant γ radiation is, however, preceded by a high-intense x-ray pulse contributing a huge non-resonant background in direction of the primary beam. Even after extreme monochromatization of the incident radiation (e.g., down to 10^{-3} eV) the signal-to-noise ratio is still 10^{-5} - 10^{-6} (with the natural width of nuclear resonance Γ_0 : 5 neV). As for Bragg reflection, an x-ray photon can be reflected by a crystal through either nuclear resonant or Rayleigh electronic scattering processes. It is the electronic scattering that brings the large background in the Bragg direction on top of the nuclear resonant signal.

Fortunately the nature of nuclear Bragg reflections offers a way out of this disappointing situation. The solution of the problem can be found using electronically forbidden but nuclear allowed Bragg reflections, which exist owing to an unusual polarization dependence of nuclear resonance scattering in the presence of hyperfine interaction. Such *pure nuclear reflections* were predicted for antiferromagnetic crystals (Tramell, 1961; Belyakov and Ayvazian, 1968) as well as for the crystals with electric field ordering (Belyakov and Ayvazian, 1969), and observed for the first time in refs. (Smirnov *et al.*, 1960; Mirzababaev *et al.*, 1971). It was a pure nuclear reflection that was applied in the first experiment where nuclear resonance excitation by synchrotron radiation was unequivocally observed (Gerdau *et al.*, 1985).

Since the pure nuclear reflectivity is intimately related to magnetic or electric hyperfine interaction, the nuclear array in a crystal behaves as a multiline radiator due to hyperfine splitting of nuclear levels. This is, of course, an inconvenient characteristic of a Mössbauer source, which can not be accepted. Luckily, a particular case of hyperfine interaction, which is well matched to the idea of the generation of a single-line Mössbauer radiation, does exist. Pure nuclear reflectivity within an energy

band of about natural linewidth of the ^{57}Fe nuclear excited level has been obtained when an iron borate $^{57}\text{FeBO}_3$ single crystal was heated close to Néel temperature T_N (Smirnov *et al.*, 1986). Temporal properties of pure nuclear diffraction in the vicinity of T_N were studied in Ref. Chumakov *et al.*, (1990) using the pulsed structure of SR.

Approaching the transition to the paramagnetic state at Néel temperature (for $^{57}\text{FeBO}_3$ T_N is :348 K), the hyperfine structure of the Mössbauer diffraction spectrum for $^{57}\text{FeBO}_3$ collapses and the reflection normally disappears above T_N due to destructive spatial interference. However, an application of an external weak magnetic field to the crystal results in a drastic transformation of the interference conditions. According to the quantum mechanical principle of superposition of states, after absorption of a SR x-ray photon every nucleus of the nuclear ensemble can be found on one of the four allowed sublevels of the excited state. Furthermore, due to mixing the nuclear spin states, each of these four sublevels is characterized by two allowed spin projections. Thus, the emission of a delayed gamma-ray photon is described by the multi-space interference of the relevant probability waves, where geometrical, energy and spin domains are intrinsically involved. The combined multipath interference in space, energy, and spin domains results in a pseudo single-line resonance structure, which provides a basis for the creation of a single-line synchrotron Mössbauer (SM) source. An analysis of the hyperfine structure under these conditions is given in Ref. Smirnov *et al.* (2000).

The first source of SR-based Mössbauer radiation has been developed (Smirnov *et al.*, 1997) in 1997 at the European Synchrotron Radiation Facility. The source emits a directed beam of fully recoilless and polarized radiation. These properties have been effectively used in the first application of the SM source for studying magnetic field distribution in iron alloys (Pankhurst *et al.*, 2001). A large progress in the further development of the SM source has recently been achieved at SPring-8 (Mitsui *et al.*, 2009).

The physics of SMS is a fascinating example of multispace quantum interference, i.e. the interference of a gamma-quantum in geometrical, energy, and spin spaces. This paper is devoted to the detailed analysis of this coherent processes, which determine the properties of the SM radiation. Namely, the angular, energy, and time distributions of the SM radiation are analyzed in order to define necessary

conditions for an optimal performance of the SM source. The remainder of the paper is organized as follows. Section 1 gives a detailed analysis of the process of the multispace interference of nuclear resonant scattering of SR by the unit cell of $^{57}\text{FeBO}_3$. In section 2, properties of the nuclear polariton for the diffraction process of γ radiation by the nuclear array are considered. In Section 3, the angular, energy, and time distributions of the ^{57}Fe SM radiation are calculated. A summary and conclusions are given in Section 4.

5.1.3 Multispace interference of γ -ray photon in the unit cell of $^{57}\text{FeBO}_3$ crystal

Table 5.1.1

Nuclear transitions between the ground and excited states with magnetic quantum numbers $m_e \rightarrow m_g$ for various transition energies TE_n and various nuclei a in the unit cell of the IB crystal.

$a \setminus TE_n$	TE_1	TE_2	TE_3	TE_4	TE_5	TE_6
1	$-\frac{1}{2} \rightarrow -\frac{3}{2}$	$-\frac{1}{2} \rightarrow -\frac{1}{2}$	$-\frac{1}{2} \rightarrow +\frac{1}{2}$	$+\frac{1}{2} \rightarrow -\frac{1}{2}$	$+\frac{1}{2} \rightarrow +\frac{1}{2}$	$+\frac{1}{2} \rightarrow +\frac{3}{2}$
2	$+\frac{1}{2} \rightarrow +\frac{3}{2}$	$+\frac{1}{2} \rightarrow +\frac{1}{2}$	$+\frac{1}{2} \rightarrow -\frac{1}{2}$	$-\frac{1}{2} \rightarrow +\frac{1}{2}$	$-\frac{1}{2} \rightarrow -\frac{1}{2}$	$-\frac{1}{2} \rightarrow -\frac{3}{2}$

We consider the emission of a γ -ray photon by the two ^{57}Fe nuclei belonging to the unit cell of $^{57}\text{FeBO}_3$ - Iron Borate (IB) - crystal. Let the nuclei be excited by a short pulse of synchrotron radiation much shorter than the lifetime of the excited nucleus. Then the processes of nuclear excitation and de-excitation are two sequential, temporally well decoupled, events. After the prompt absorption of a primary photon and some dwelling in the intermediate excited state, the transition back to the ground

state occurs with emission of a secondary photon. In accordance with the general principles of excitation, both nuclei are excited in the intermediate state with equal probability amplitudes, the phases of which in the case of a plane synchrotron radiation wave are determined by the scalar product $\mathbf{k}_i \mathbf{r}_a$, where \mathbf{k}_i is the wave vector of the incident radiation and \mathbf{r}_a is the vector indicating the position of a nucleus in the unit cell ($a=1,2$). In order to calculate the emission in the direction \mathbf{k}_f , one should add up the amplitudes of the two γ -ray wavelets with the account of their relative phase, which is determined by the difference in their corresponding optical paths. The phase difference is then given by the expression $(\mathbf{k}_f - \mathbf{k}_i) \cdot (\mathbf{r}_2 - \mathbf{r}_1)$. Thus, *in order to evaluate the result of the interference in geometrical space, one has to consider two paths*. The phase difference of waves scattered along the two paths plays a crucial role for the intensity of emission.

Each of the two spatial paths is branched further into separate paths within the energy domain. Due to magnetic dipole interaction of the nuclear spin with the internal field, the nuclear levels in the IB crystal are split into sublevels. The level of the ground state having nuclear spin $I_g = \frac{1}{2}$ splits into two sublevels; and the level of the excited state having spin $I_e = \frac{3}{2}$ splits into four sublevels. The selection rules for magnetic dipole transition (M1), relevant to our case, allow one to observe six nuclear transitions between the ground and excited states with the change of the magnetic quantum number $M = m_e - m_g = 0, \pm 1$. Here m_e, m_g are the magnetic quantum numbers for the excited and ground nuclear states, respectively.

The IB crystal is a canted antiferromagnet. The magnetic and crystalline unit cells of the crystal are the same (like for Fe_2O_3 hematite crystal, see Fig. 16 in Ref. Shull *et al.* (1951)). The magnetic fields acting upon nuclei in the unit cell are equal in magnitude but almost opposite in direction. For this reason, the sublevels of the excited and the ground states have the same energies for both nuclei but the states appropriate to the equivalent sublevels are characterized by the opposite signs of the magnetic quantum numbers. Therefore, the transitions at the 1st and 2nd nuclei with the same resonant transition energies (TE_n) have the opposite signs in the change M

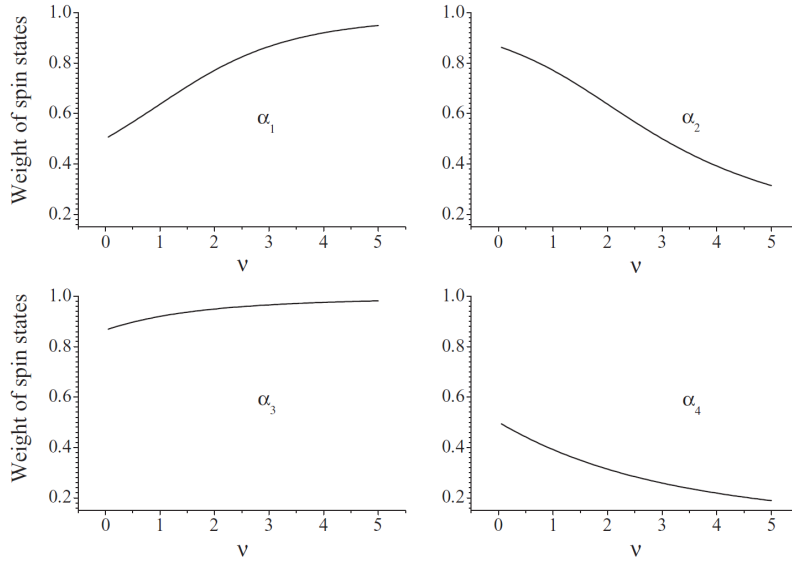
of the spin magnetic quantum numbers, see Table 5.1.1. Here the spin quantization axis z is chosen to be directed along the magnetic field at the 1st nucleus.

For each arbitrary energy TE of the radiation spectral component all six transitions will give its specific contribution to the interference field depending on the energy distance between TE and a resonant energy TE_n , where $n = 1, 2, \dots, 6$. Here one definitely faces a bright case of *inter-resonance nuclear interference*. For the Lorentzian shape of each resonance, the summary amplitude of scattering is then

proportional to $\sum_{n=1}^6 \frac{1}{v_n - i}$, where $v_n = (TE - TE_n)/(\Gamma_0/2)$ stands for the energy

deviation from n th resonance in the units of the resonance natural half-width (for the sake of simplicity we have assumed so far that the amplitudes of different transitions are equal to each other). Thus, for the two nuclei in the unit cell the *combined process of γ -ray interference in geometrical and energy spaces involves twelve contributions*.

The arrangement of atoms in the IB crystal does not only result in the formation of the internal magnetic field at the iron sites but also in the creation of a non-uniform crystalline electric field. The electric field gradient (EFG) in the crystal exhibits axial symmetry. The principal axis of the EFG tensor is orthogonal to the internal magnetic field at both iron sites. The ^{57}Fe nucleus in the first excited state possesses both a magnetic and a quadrupole moment, while in the ground state it has only a magnetic moment. So, the nucleus experiences a pure magnetic dipole interaction in the ground state and a combined magnetic dipole and axially symmetric electric quadrupole interaction in the excited state.


Figure 5.1.1

Amplitudes α_{1-4} of contributions of the pure spin states $\left| \pm \frac{1}{2} \right\rangle$, $\left| \pm \frac{3}{2} \right\rangle$ into the mixed spin states for different energy sublevels ε_{1-4} of the excited nuclear state of different nuclei in the unit cell of the IB crystal, see Table II. For parameter ν see explanation to Eq. (5.1.1).

The splitting of nuclear states in an IB crystal under conditions of the combined magnetic dipole and electric quadrupole hyperfine interaction has been analyzed in ref. Smirnov (2000). The four dimensionless energies ε of the hyperfine interaction in the excited state are given by

$$\begin{aligned} \varepsilon_{1,3} &= +\frac{1}{2}\nu \pm \sqrt{\nu^2 - 3\nu + 9}, \\ \varepsilon_{2,4} &= -\frac{1}{2}\nu \pm \sqrt{\nu^2 + 3\nu + 9}, \end{aligned} \quad (5.1.1)$$

where $\nu = \omega_B/\omega_E$, $\hbar\omega_B = g_e\mu_n B$ is the energy of interaction of the magnetic moment of the nucleus in the excited state with the internal magnetic field B (g_e is the nuclear g -factor in the excited state, μ_n is the nuclear magneton) and $\hbar\omega_E = \frac{1}{2}eQ \frac{\partial^2 V_{el}}{\partial y^2} \frac{1}{2I_e(2I_e - 1)}$ is the energy of interaction of the nuclear electric quadrupole moment Q with the electric field gradient (V_{el} is the electric field potential at the nucleus, e is the charge of proton); ε_i are given in the units of the quadrupole interaction energy $\hbar\omega_E$. Since in the excited state of ^{57}Fe the g -factor is

negative, the sub-level energies are ordered in the following way: $\varepsilon_1 \leq \varepsilon_2 \leq \varepsilon_3 \leq \varepsilon_4$. Concerning the value of the internal magnetic field, it is a function not only of temperature but also of the applied magnetic field. The application of the external field plays a significant role in the near vicinity of Néel temperature where antiferromagnetic ordering of the atomic spins can be induced in the crystal (Borovik-Romanov and Ozhgin, *et al.*, 1960).

For pure magnetic interaction pure spin states (i.e., the states with a defined spin projection m) can exist. But under conditions of combined magnetic and electric hyperfine interaction the excited nuclear states may be mixed over the spin projections. In the particular case of the axially symmetric EFG with the main axis orthogonal to the magnetic field and z-axis directed along the magnetic field, each nuclear excited state is mixed over two spin projections. In this case the Hamiltonian eigenvalues given by Eq. (5.1.1) are appropriate for the eigen functions of the excited states represented in Table 5.1.2.

Table 5.1.2:

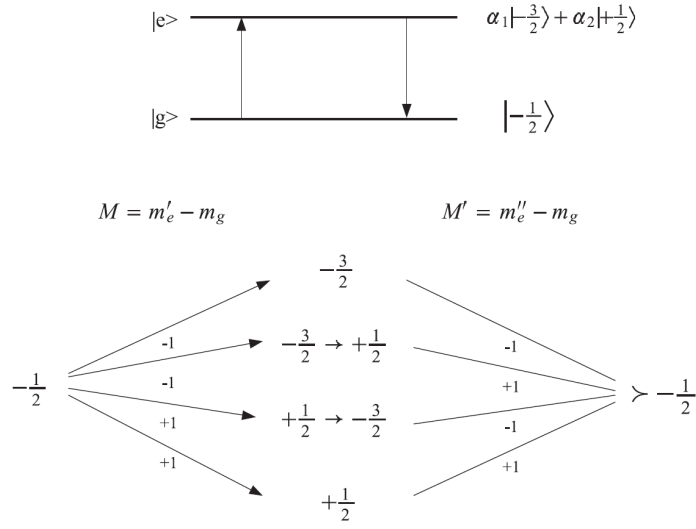
The mixed-spin eigen functions for various excited nuclear states with the eigen energies ε_i and for various nuclei a in the unit cell of the IB crystal.

$a \setminus \varepsilon$	ε_1	ε_2	ε_3	ε_4
1	$\alpha_1 -\frac{3}{2}\rangle + \alpha_2 +\frac{1}{2}\rangle$	$\alpha_3 -\frac{1}{2}\rangle + \alpha_4 +\frac{3}{2}\rangle$	$\alpha_1 +\frac{1}{2}\rangle + \alpha_2 -\frac{3}{2}\rangle$	$\alpha_3 +\frac{3}{2}\rangle + \alpha_4 -\frac{1}{2}\rangle$
2	$\alpha_1 +\frac{3}{2}\rangle + \alpha_2 -\frac{1}{2}\rangle$	$\alpha_3 +\frac{1}{2}\rangle + \alpha_4 -\frac{3}{2}\rangle$	$\alpha_1 -\frac{1}{2}\rangle + \alpha_2 +\frac{3}{2}\rangle$	$\alpha_3 -\frac{3}{2}\rangle + \alpha_4 +\frac{1}{2}\rangle$

The excited nuclear states with energies $\varepsilon_1, \varepsilon_3$ are mixed over spin projections $+\frac{1}{2}, -\frac{3}{2}$, whereas the states with energies $\varepsilon_2, \varepsilon_4$ are mixed over spin projections $-\frac{1}{2}, +\frac{3}{2}$. Table 5.1.2 shows that only four amplitudes $\alpha_1, \alpha_2, \alpha_3, \alpha_4$ are required to describe the eigen functions of all excited states for both nuclei. Following the analysis presented in Ref. (Smirnov, 2000), these amplitudes can be obtained in an explicit form

$$\begin{aligned}\alpha_1 &= \frac{1}{\sqrt{A_1^2/27+1}}, A_1 = 2\nu - 3 - 2\sqrt{\nu^2 - 3\nu + 9}, \\ \alpha_2 &= \frac{1}{\sqrt{A_2^2/27+1}}, A_2 = 2\nu - 3 + 2\sqrt{\nu^2 - 3\nu + 9}, \\ \alpha_3 &= \frac{1}{\sqrt{A_3^2/27+1}}, A_3 = 2\nu + 3 - 2\sqrt{\nu^2 + 3\nu + 9}, \\ \alpha_4 &= \frac{1}{\sqrt{A_4^2/27+1}}, A_4 = 2\nu + 3 + 2\sqrt{\nu^2 + 3\nu + 9}.\end{aligned}\tag{5.1.2}$$

They are defined by a single parameter $\nu = \omega_B/\omega_E$. The magnetic hyperfine field in the IB crystal is a function of temperature. Approaching the transition to the paramagnetic state at Néel temperature T_N , the field magnitude B rapidly decreases. At room temperature, the magnetic interaction dominates over the electric one, parameter $\nu \cong 90$, and the excited nuclear states are nearly pure spin states with $\alpha_1 \cong \alpha_3 \cong 1$ and $\alpha_2 \cong \alpha_4 \cong 0$. On the contrary, in the range of $\nu < 10$ the excited states are already significantly mixed over spin projections. The evolution of the mixed-spin states is illustrated in Fig. 5.1.1. The dependences of the pure spin state contributions α_{1-4} into the mixed states are shown within the range of $\nu < 5$, where the magnetic dipole and electric quadrupole hyperfine interactions are getting comparable. Figure 5.1.1 clearly shows that in approaching Néel temperature ($\nu \rightarrow 0$), the excited states are getting strongly mixed over spin projections. Because the two spin projections are mixed in each excited substate the resonance scattering via a separate nuclear transition in every nucleus branches out further into the four paths.


Figure 5.1.2

Scattering paths via the pure spin states of the excited nuclear sub-state having energy ε_1 in the 1st nucleus of the IB crystal unit cell. On the upper panel the transitions, up and down, between the ground and the excited states are displayed. On the lower panel four possible paths are shown, where changes of spin projections in different paths are indicated. $M = m_e - m_g = \pm 1$ are the changes of magnetic quantum number in separate transitions; m_e, m_g are the magnetic quantum numbers for the excited and ground nuclear states respectively.

For elastic scattering, the process considered here, the initial and final states are the same. Therefore, if measurements do not permit to establish, which intermediate spin state was involved in the scattering, the scattering paths related to all intermediate states should interfere. Here one meets an interesting case of *intra-resonance nuclear interference* in the spin domain. Fig. 5.1.2 shows an example of the scattering paths via the nuclear transition with the lowest transition energy TE_1 for the 1-st nucleus. As it is seen from the figure, in order to build up the interference field for a given transition in a single nucleus, four wavelets of the same frequency but different in polarization states and scattering amplitudes should be added. The amplitude of a wavelet for n -th nuclear transition in a -th nucleus contains the complex G_n^a - factor given by the following general expression

$$G_n^a(m_e', m_e'') = \left\langle \frac{1}{2}, m_g; 1, M \mid \frac{3}{2}, m_e' \right\rangle \left\langle \frac{1}{2}, m_g; 1, M' \mid \frac{3}{2}, m_e'' \right\rangle c_j^{m_e'} c_j^{m_e''} (\mathbf{h}_d^s \mathbf{u}_{-M}^a) (\mathbf{h}_d^s \mathbf{u}_{-M'}^a)^*, \quad (5.1.3)$$

where $\left\langle \frac{1}{2}, m_g; 1, M \mid \frac{3}{2}, m_e \right\rangle$ designates a Clebsch--Gordan coefficient, which is a probability factor for the transition between sublevels of the ground and excited states taking into account the angular momentum transfer for the (nucleus+photon) system; it also depends on the spins of the ground and the excited states and on their z-projections. In this manuscript we are considering diffraction with (M1) multipolarity (magnetic dipole transition) and have chosen the magnetic basis for the polarization vector: $(\mathbf{h}_d^s \mathbf{u}_{-M}^a)$ is the scalar product of the magnetic polarization vector \mathbf{h}_d^s of the wave propagating in the direction $d = 0, 1$ (0 stands for the direction along the incident wave, 1 - for the direction along the exit wave), with polarization $s = \pi, \sigma$ (vectors $\mathbf{h}_{0,1}^\sigma$ lie in the scattering plane, while vectors $\mathbf{h}_{0,1}^\pi$ are perpendicular to it) and the spherical unit vector \mathbf{u}_{-M}^a in the coordinate system related to the hyperfine fields at a th nucleus in the unit cell: $\mathbf{u}_0^a = \mathbf{u}_z^a$, $\mathbf{u}_{\pm 1}^a = \mp \frac{1}{\sqrt{2}} (\mathbf{u}_x^a \pm i\mathbf{u}_y^a)$, where $\mathbf{u}_{x,y,z}$ are mutually orthogonal unit vectors related to the hyperfine fields in the unit cell, \mathbf{u}_z is directed along vector \mathbf{B} (see Fig. 5.1.3); finally, $c_j^{m_e}$ are the amplitudes of spin states in the j th sub-level of the excited nuclear state. Below the $c_j^{m_e}$ - amplitudes are related to the defined above α amplitudes.

$$\begin{aligned}
 c_1^{-\frac{3}{2}} &= c_1^{+\frac{3}{2}} = c_3^{-\frac{1}{2}} = c_3^{-\frac{1}{2}} = \alpha 1, \\
 c_1^{+\frac{1}{2}} &= c_1^{-\frac{1}{2}} = c_3^{-\frac{3}{2}} = c_3^{+\frac{3}{2}} = \alpha 2, \\
 c_2^{-\frac{1}{2}} &= c_2^{+\frac{1}{2}} = c_4^{+\frac{3}{2}} = c_4^{-\frac{3}{2}} = \alpha 3, \\
 c_2^{+\frac{3}{2}} &= c_2^{-\frac{3}{2}} = c_4^{-\frac{1}{2}} = c_4^{+\frac{1}{2}} = \alpha 4.
 \end{aligned} \tag{5.1.4}$$

In the example, depicted in Fig. 5.1.2, the interference in spin space leads to the following expression of the G_1^1 -factor

$$\begin{aligned}
 G_1^1 &= \frac{1}{2} \alpha_1^2 (\mathbf{h}_d^s \mathbf{u}_{+1}^1) (\mathbf{u}_{d'}^s \mathbf{u}_{+1}^1)^* \\
 &+ \frac{1}{2\sqrt{12}} \alpha_1 \alpha_2 (\mathbf{h}_d^s \mathbf{u}_{+1}^1) (\mathbf{h}_{d'}^s \mathbf{u}_{-1}^1)^*
 \end{aligned} \tag{5.1.5}$$

$$\begin{aligned}
 & + \frac{1}{2\sqrt{12}} \alpha_2 \alpha_1 (\mathbf{h}_d^s \mathbf{u}_{-1}^1) (\mathbf{h}_{d'}^{s'} \mathbf{u}_{+1}^1)^* \\
 & + \frac{1}{12} \alpha_2^2 (\mathbf{h}_d^s \mathbf{u}_{-1}^1) (\mathbf{h}_{d'}^{s'} \mathbf{u}_{-1}^1)^*.
 \end{aligned}$$

This example explicitly shows that the result of interference in spin space is strongly dependent on the amplitudes α_j of the pure spin sub-states in the mixed state, which are functions of the crystal temperature. In order to derive the intensity of the emitted radiation, one needs to calculate the nuclear susceptibility amplitude η taking into account all the mentioned interference paths according to the following expression:

$$\eta_{dd'}^{ss'} = -\frac{3}{KV_0} \sigma_0 \beta f_{LM} \sum_a \exp\{(\mathbf{k}_{d'} - \mathbf{k}_d) \cdot \mathbf{r}_a\} \sum_n \frac{1}{V_n - i} \sum_{m_e' m_e''} G_n^a(m_e', m_e''), \quad (5.1.6)$$

The outermost summation here represents the inter-nuclear interference of scattering by different nuclei in the unit cell, the medium summation represents the inter-resonance nuclear interference of scattering via the transitions between the various sublevels of the ground and the excited states, and the innermost summation represents the intra-resonance nuclear interference in the transitions via the various spin states of a particular excited nuclear sub-state.

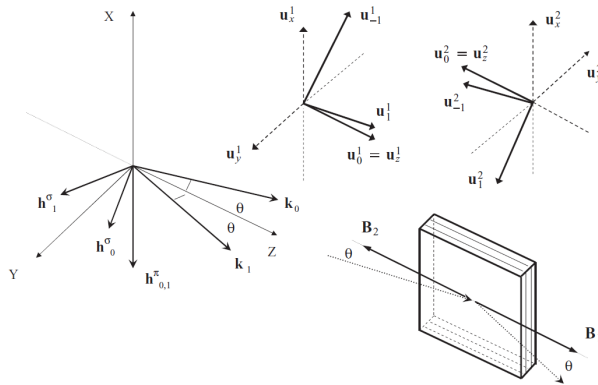


Figure 5.1.3:

Scattering geometry of synchrotron radiation from two nuclei in the IB crystal unit cell; $\mathbf{k}_{0,1}$ and $\mathbf{h}_{0,1}^{\pi,\sigma}$ are the wave vectors and the magnetic polarization vectors of the incident and scattered waves respectively, θ is incidence angle (symmetric scattering geometry is considered); $\mathbf{B}_{1,2}$ are the magnetic fields at the nuclei in the unit cell; $\mathbf{u}_{0,1,-1}^{1,2}$ are the spherical unit vectors related to hyperfine fields at the 1st and 2nd nuclei in the IB crystal unit cell (see text for definition).

In Eq. (5.1.5) $K = 2\pi/\lambda$ stands for the radiation wave number in vacuum; V_0 is the volume of the crystal unit cell; σ_0 is the resonance cross-section; β is the resonant isotope abundance; f_{LM} is the recoilless scattering factor, which is the product of square roots of the Lamb-Mössbauer factors in the directions d, d' ; \mathbf{k}_d and $\mathbf{k}_{d'}$ are the wave-vectors of the incident and exit waves, respectively. In general the nuclear susceptibility amplitudes form a matrix with dimensions (4×4) . Altogether, the *combined γ -ray interference process in the geometrical, energy, and spin spaces should involve 48 contributions.*

In the IB crystal pure nuclear diffraction occurs for the reflections with an odd sum of the Miller indexes, in particular, for reflections (111), (333) etc. These are symmetric reflections, because IB crystals grow as platelets with surface planes parallel to the (111) crystallographic plane. We consider the horizontal scattering geometry. That is illustrated in Fig. 5.1.3, where the polarization and wave vectors of the incident and scattered waves and the sets of the spherical unit vectors at each nucleus in the unit cell are depicted. The magnetic fields at the nuclei lie in the scattering plane.

Synchrotron radiation is linearly polarized. The magnetic polarization vector \mathbf{h}_0^π is perpendicular to the scattering plane. The internal magnetic fields $\mathbf{B}_{1,2}$ are orthogonal to the magnetic polarization vector. In the chosen geometry, the susceptibility amplitudes matrix is reduced to a matrix of second rank. For the π -polarized incident radiation, it takes the following form

$$\eta_{dd'}^{ss'} = \begin{vmatrix} \eta_{00}^{\pi\pi} & \eta_{01}^{\pi\sigma} \\ \eta_{10}^{\sigma\pi} & \eta_{11}^{\sigma\sigma} \end{vmatrix}. \quad (5.1.7)$$

In the presence of hyperfine interaction a nuclear array may act as an optically active medium for incident γ -radiation. In particular, because of the antiferromagnetic arrangement of the fields at the nuclei in the unit cell of the IB crystal, the polarization plane under conditions of pure nuclear diffraction is turned through angle $\pi/2$, so that the exit wave is σ -polarized. In the next section we consider the coherent scattering of the γ -ray by the whole nuclear array in the crystal.

5.1.4 Nuclear exciton polariton under diffraction conditions

A nuclear array in a crystal represents for Mössbauer radiation a resonating three-dimensional grating, which gives rise to resonant Bragg diffraction of γ -rays. If regularity of the grating persists over a large volume of the crystal, the multiple scattering of radiation occurs. Mutual interference of the propagating and Bragg reflected waves produces a resultant wavefield the structure of which is of a standing wave type. In this way the standing wave mode of nuclear exciton polariton is realized under conditions of Bragg diffraction. At the exit of the crystal a coherent beam of resonant γ radiation is formed. In general, the Bragg diffraction in large perfect crystals is described by the dynamical theory accounting for the multiple scattering of radiation by atoms. The dynamical theory for nuclear resonant scattering was developed by different groups using different approaches. A detailed account of the dynamical diffraction theory of nuclear resonant diffraction is given by Kagan, Trammell and Hannon in their reviews (Kagan, 1999; Hannon and Trammell, 1999). We shortly summarize the theory based on the solution of the Maxwell equations and apply it to our case.

The existence of the nuclear exciton provides the physical basis for the use of a macroscopic polarization, which is given by the Maxwell equations to treat the radiative effects of the nuclei. The induced nuclear current density represents then a quantum mechanical average over the nuclear ensemble. For a space and time Fourier component of the electric-field vector $\mathbf{E}(\mathbf{k}, \omega)$, which represents the amplitude of a plane monochromatic γ -ray wave having the wave vector \mathbf{k} and frequency ω , the Maxwell wave equation can be written in the following form

$$\left[k^2 - K^2 \right] \mathbf{E}(\mathbf{k}, \omega) - \mathbf{k}(\mathbf{k} \cdot \mathbf{E}(\mathbf{k}, \omega)) = \frac{4\pi i \omega}{c^2} \mathbf{j}(\mathbf{k}, \omega), \quad (5.1.8)$$

where K and k are the radiation wave numbers in vacuum and inside the crystal, respectively, $\mathbf{j}(\mathbf{k}, \omega)$ is the Fourier component of the induced current density. It has contributions from both the electric and nuclear subsystems. But our interest is focused on the pure nuclear reflections. In this case the interference field is created only by nuclear currents and the above equation is in fact the equation for a space time Fourier component of the nuclear polariton where the radiation field and nuclear excitation are related. In the linear in field approximation the excited nuclear current

$\mathbf{j}(\mathbf{k}, \omega) \propto \boldsymbol{\eta} \cdot \mathbf{E}(\mathbf{k}, \omega)$ is proportional to the nuclear susceptibility amplitude. Employing this relationship one can arrive at the Maxwell equation for the field amplitude only. For the two-waves diffraction case the Maxwell wave equation splits into a set of two equations and in the conditions described in the previous section the equations set acquires the form

$$\begin{aligned} \left(\frac{k_0^2}{K^2} - 1 \right) E_0^\pi &= \tilde{\eta}_{00} E_0^\pi + \tilde{\eta}_{01} E_1^\sigma \\ \left(\frac{k_1^2}{K^2} - 1 \right) E_1^\sigma &= \tilde{\eta}_{10} E_0^\pi + \tilde{\eta}_{11} E_1^\sigma \end{aligned} \quad , \quad (5.1.9)$$

where E_d^s is the scalar electric field amplitude of a definite wave polarization and propagation direction, k_0 and k_1 are the complex wave numbers describing the coherent waves inside the crystal and $\tilde{\eta}_{dd}^{ss'}(\omega)$ are the nuclear susceptibility amplitudes considered above (radiation frequency $\omega = TE/\hbar$), the amplitudes labeled by tilde include the electronic susceptibility amplitudes. Electrons add their contribution only into 00 and 11 scattering channels. The complex wave numbers $k_{0,1}$ differ from the absolute value of the wave vector in vacuum K by only small complex corrections

$$\begin{aligned} k_0 &= K(1 + \varepsilon_0) \\ k_1 &= K(1 + \varepsilon_1) \end{aligned} \quad . \quad (5.1.10)$$

In the vicinity of the Bragg angle $\varepsilon_1 = \alpha/2 + \varepsilon_0/\beta$, where $\alpha = -2 \sin 2\theta_B \Delta\theta$ is the angular parameter proportional to the deviation $\Delta\theta$ from the Bragg angle θ_B and β is asymmetry parameter, $\beta = -1$ in the case of symmetric Bragg diffraction. With the account of the relations Eq. (5.1.10) we arrive at the following equations set (neglecting the small order values)

$$\begin{aligned} 2\varepsilon_0 E_0 &= \tilde{\eta}_{00} E_0 + \eta_{01} E_1 \\ (-2\varepsilon_0 + \alpha) E_1 &= \eta_{10} E_0 + \tilde{\eta}_{11} E_1 \end{aligned} \quad , \quad (5.1.11)$$

where polarization indexes are omitted. The equations (5.1.11) have a solution for the scalar field amplitudes only if the determinant formed by their coefficients vanishes

$$\begin{bmatrix} \tilde{\eta}_{00} - 2\varepsilon_0 & \eta_{01} \\ \eta_{10} & \tilde{\eta}_{11} + 2\varepsilon_0 - \alpha \end{bmatrix} = 0. \quad (5.1.12)$$

Eq. (5.1.12) determines the dispersion of the electromagnetic waves in the crystal, giving the complex value ε_0 as a function of the radiation frequency ω and of the angular deviation α from the exact Bragg position. There are two roots of the Eq. (5.1.12)

$$\varepsilon_0^{(1,2)} = \frac{1}{4} \left\{ \left(\tilde{\eta}_{00} - \tilde{\eta}_{11} + \alpha \right) \right\} \mp \sqrt{\left(\tilde{\eta}_{00} + \tilde{\eta}_{11} - \alpha \right)^2 - 4\eta_{10}\eta_{01}}. \quad (5.1.13)$$

Thus one should consider the two standing wave solutions for the interference wavefields WF1 and WF2, each corresponds to a particular dispersion correction $\varepsilon_0^{(1)}$ or $\varepsilon_0^{(2)}$. Substituting ε_0 from Eq. (5.1.13) into Eq. (5.1.11) one can find solutions for the relevant pairs of the scalar amplitudes. Since Eqs. (5.1.11) are homogeneous one has to use in addition the boundary conditions for the scalar amplitudes. Finally one arrives at the solutions for the WF amplitudes where the latter are modulated in the direction perpendicular to the reflecting planes in such a way that the *WF1 experiences an anomalously weak nuclear absorption*, while *the WF2 on the contrary - an anomalously strong absorption*. In the limit of a semi-infinite crystal only the WF1 survives. A strong suppression of inelastic scattering channels for this wavefield is favoring an enhanced γ -ray emission nearly without the internal conversion, see Refs. (Afanas'ev & Kagan, 1965; Smirnov, 1986). The solution for the emitted radiation in this case is as follows

$$E(\alpha, \omega) = \frac{\eta_{10}}{2\varepsilon_0^{(1)} - \tilde{\eta}_{00}} E_{SR}, \quad (5.1.14)$$

where $E_{SR} = \sqrt{I_{SR}/\Delta\omega}$ is the scalar amplitude of the SR with I_{SR} as the intensity of SR within the frequency range $\Delta\omega$ selected by the monochromator system.

For nuclear resonant Bragg reflections the emission from a crystal containing a nuclear array exhibits a combined angular and energy dependence.

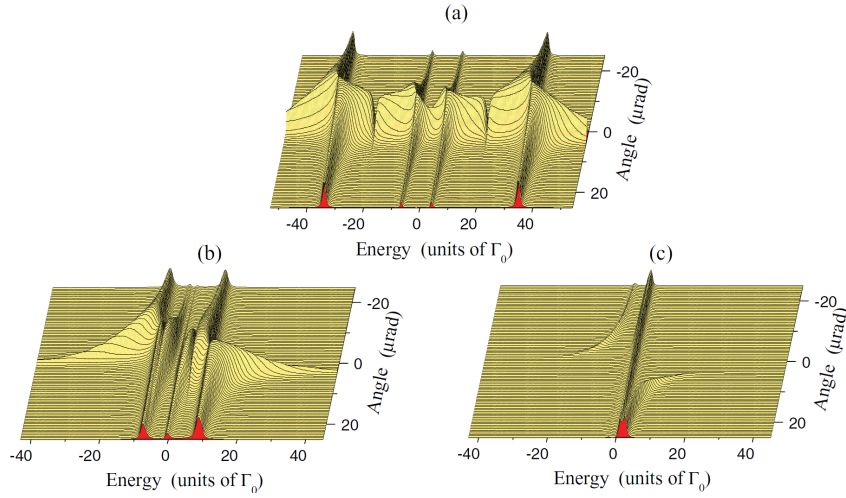


Figure 5.1.4

Evolution of the γ -ray emission landscape. The internal magnetic field at ^{57}Fe nuclei positions is: a) 330 kOe, b) 50 kOe, c) 2 kOe.

A three-dimensional landscape of a Bragg reflection in the vicinity of the nuclear resonance and of the Bragg angle is formed. In the case of the IB crystal the landscape undergoes dramatic changes while heating the crystal from room to Néel temperature. The transformation of the energy-angular landscape is seen from Fig. 5.1.4. The emission intensity functions $I(\alpha, \omega) = |E(\alpha, \omega)|^2$ are displayed there for the actual scattering geometry (see Fig. 5.1.3) in the case of the pure nuclear reflection (333) for three different values of the internal magnetic field: 330 kOe ($\nu \approx 87$), Fig. 5.1.4a, 50 kOe ($\nu \approx 13$), Fig. 5.1.4b, and 2 kOe ($\nu \approx 0.5$), Fig. 5.1.4c. The energy scales cover the range of characteristic hyperfine interaction in $^{57}\text{FeBO}_3$ and the angular scales cover the characteristic range of nuclear Bragg reflection (333) in the iron borate single crystal. The four well separated crests, extended along the angular coordinate are seen in Fig. 5.1.4a, each belongs to one of the allowed transitions with $M = \pm 1$ at the relevant transition energies $TE_{1,3,4,6}$, see Table 5.1.1. The angular scale is centered at the Bragg angle. Far from the Bragg angle the four isolated resonance peaks (i.e., resonance lines) are formed. In approaching the Bragg angle the resonances exhibit an impressive broadening: the resonance lines with widths of several tenths of Γ_0 are getting overlapped in this angular range. This is an exciting result of a strong coherent enhancement of the radiative channel (van Bürck *et al.*, 1980; Schvyd'ko and Smirnov, 1989). Because of the resonance broadening the inter-

resonance interference starts playing the essential role even at room temperature. On the overlapping slopes of the 1st and the 3rd lines, as well as of the 4th and the 6th lines the deep and sharp valleys (i.e., minima of the scattered intensity) are observed which are due to the resonance absorption of γ radiation at the energies $TE_{2,5}$. For the transitions $M = 0$ the nuclear diffraction is cancelled due to destructive interference of the constituting waves in geometric space.

When due to the crystal heating the internal field decreases down to 50 kOe, the role of the inter-resonance interference rises significantly, Fig. 5.1.4b. The effect of the interference is seen in a much broader angular range. The interference causes a strong asymmetry in both energy and angular distribution of the emitted radiation. Beyond the Bragg angle range the energy spectrum contains only three peaks at the lower angles, - the 3rd line is suppressed over there, while at the higher angles the four lines are present but with the strongly weakened inner ones. Within the Bragg angle range a complicated interference pattern is observed where one can still distinguish the four lines of about equal strength. On the energy scale, off the resonance range far extended wings attract attention. They are also present on the former figure. The wings represent an axial symmetric configuration. Such a symmetry is due to varying conditions of the interference of the waves scattered by nuclei and is related to the fact that the real part of the nuclear amplitude is uneven function of the energy deviation from resonance.

Finally, we come near to the Néel point with the magnetic field of only 2 kOe (Fig. 5.1.4c). The multi-line spectrum of the emitted radiation has significantly collapsed here. In the vicinity of the Bragg angle a pseudo single line resonance structure is observed, which is created by the destructive inter-nuclear interference (in geometrical space) as well as by a strong inter-resonance (in energy domain) and intra-resonance (in spin-domain) interference of radiation components discussed in the previous section.

As seen in Fig. 5.1.4 emission occurs over a range of settings of the crystal around the Bragg angle. To reveal the details of the interference pattern in the following section we have analyzed the angular function of the coherent emission and determined the angular breath of strong emission for different magnitudes of the internal magnetic field. In addition the spectral composition and the time distribution of γ -ray photons radiated by the nuclear array in SM source were examined.

5.1.5 Angular, energy and time distributions of ^{57}Fe SM radiation

Initially we discuss the geometrical properties of the interference pattern. First of all we wish to know how the intensity of the γ radiation emitted by the crystal depends on its angular setting in the vicinity of the Bragg angle. To estimate the theoretical angular width of the emission function for a perfect crystal we can neglect the angular width of the incident beam, assuming a plane wave is incident on the crystal. To find in this way the *emission angular function* we have to integrate the two dimensional emission function $I(\alpha, \omega)$ (for its definition see text after Eq. (5.1.14)) over frequency, assuming SR intensity to be frequency independent value $I_{SR}(\omega) = \text{const}$ over the whole range of the nuclear resonance. The *emission angular function* is then given by the following integral

$$I(x) = \int_{-\infty}^{+\infty} dv I(x, v) , \quad (5.1.15)$$

where in the intensity function the angular and frequency variables are replaced adequately: $x = \Delta\theta \propto \alpha$ and $v = \hbar\omega/(\Gamma_0/2)$. One should underline that the expression of Eq. (5.1.15) gives the emission angular dependence integrated over the whole resonance range. The emission angular functions for different magnitudes of the internal magnetic field are displayed in Fig. 5.1.5. The curve on the bottom panel of Fig. 5.1.5 having a symmetric shape represents the angular dependence of emission at room temperature. The center of angular range of pronounced emission is shifted with respect to the angle given by the original Bragg reflection law by $15.5 \mu\text{rad}$. This shift is due to refraction of the incident beam at the entrance into the crystal. The width of the reflectivity curve is very small, $5 \mu\text{rad}$.

When heating the crystal towards Néel temperature the breadth and shape of the emission angular function is drastically changed. Three main features can be recognized (Smirnov, 2009):

- significant decrease of the emitted intensity,
- strong broadening of the angular range of emission,

- creation of the double hump structure of the angular curves with the dip exactly at the Bragg angle corrected for refraction.

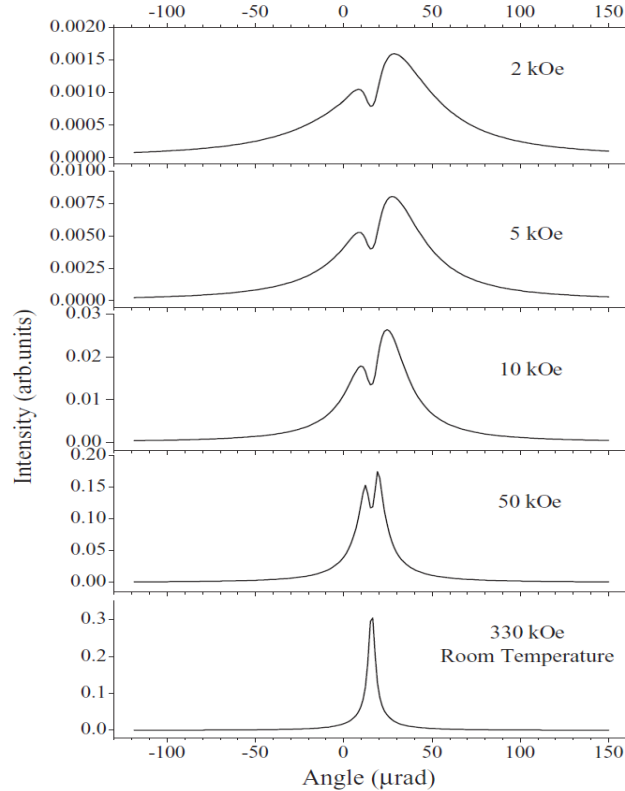


Figure 5.1.5

The emission angular dependence of γ radiation from the IB crystal integrated over the whole resonance range. The angular setting of the IB crystal is changed in the vicinity of Bragg angle for pure nuclear reflection (333). The angular functions are displayed for different values of the internal magnetic field decreasing from the bottom to the top in approaching Néel temperature.

At the lowest field (i.e., the highest temperature of the crystal) the emission intensity is only of the order of 10^{-2} of the intensity at room temperature. Such diminution of the coherent emission near Néel temperature was expected because of the destructive nature of interference at this temperature.

Along with the decrease of the coherent emission the angular range of emission is being significantly enlarged: from $\approx 5 \mu\text{rad}$ at the field of 330 kOe (the bottom panel in Fig. 5.1.5) up to $\approx 60 \mu\text{rad}$ at the field of 2 kOe (the upper panel in Fig. 5.1.5). This happens because the strong off-resonance wings of nuclear scattering (located mainly in the narrow angular interval around the exact Bragg position, i.e., around the peak of the rocking curve, see Figs. 5.1.4a,b) become heavily suppressed by destructive interference when temperature approaches T_n (Fig. 5.1.4c). On the

contrary, the wider angular distribution of the on-resonance scattering is less affected by destructive interference (Fig. 5.1.4c). Thus, it provides the wider rocking curve around T_n . It is of interest to note that a further decrease of the field and of the related emission intensity is not accompanied any longer by a change of the shape and the width of the angular curve. A kind of saturation is reached in the breadth of the angular range of emission of γ rays over the entire resonance region near the Néel point.

Fig. 5.1.4c shows that the outer wings of the landscape falls abruptly in the narrow angular interval near the Bragg angle. Computer analysis of the emission function shows that the wings are shifted out of the immediate Bragg range more and more as the collapse of the hyperfine structure occurs. They start therefore to give their contributions to the emitted radiation only when the angle of incidence is shifted from the central zone to the sides. This is the reason for the formation of the double hump structure and the appearance of the dip in the emission angular function.

The angular distribution of the emitted γ radiation is determined both by the emission angular function and by the instrumental function, i.e., by the angular distribution of synchrotron radiation in the incident beam. When the angular divergence of the exciting radiation is large in comparison with the angular width of the range of emission, the emission occurs throughout the whole allowed range. If the SR intensity is a constant value in this range, the angular distributions of the emitted γ radiation just repeat those depicted in Fig. 5.1.5. In the opposite case of very small divergence of the exciting radiation in comparison with the angular width of emission, the angular distribution of γ radiation reproduces the instrumentation function form. To get the angular distribution of the emitted radiation in an intermediate case one must find the product of the emission angular function $I(x)$ and of the instrumental function at an arbitrary angle of incidence x_p of the exciting synchrotron radiation. An example of the angular distribution of the emitted radiation is shown in Fig. 5.1.6, assuming the instrumental function to be of Gaussian form

$$F(x, x_p) = \frac{1}{\sigma\sqrt{2\pi}} \exp\left\{-\frac{(x-x_p)^2}{2\sigma^2}\right\}. \text{ The nuclei are excited by SR exactly at the dip of}$$

the emission angular function, $x_p = 15.5 \mu\text{ rad}$ and $2\sigma = 10 \mu\text{ rad}$. The angular

distribution of γ radiation emitted in the vicinity of Néel temperature for the internal magnetic field of 2 kOe is compared with the instrumental angular function. As seen in the figure, under the considered real conditions, the angular breadth of the emitted radiation exceeds slightly the angular width of the instrumental function. The top of the distribution is slightly modulated by the emission angular function.

We turn now to the energy distribution of the emitted γ radiation for a fixed angle of incidence of the exciting SR beam. At the beginning we consider a simple model of the destructive inter-resonance interference. As shown in ref. Smirnov (2000), due to the combined multispace interference only two resonance lines survive close to Néel temperature. They belong to the 3rd and 6th resonances in the original hyperfine structure in the $^{57}\text{FeBO}_3$. The energies of the relevant transitions nearly coincide and the strengths of the lines are almost equal. Thus the spectrum in our model can be presented by the sum of two Lorentzians, each renders a single line radiation emitted at a separate resonance transition,

$$L(\nu, \nu_1 - \nu_2) = \sum_{k=1,2} \left| A_k \frac{1}{(\nu - \nu_k) - i} \right|^2 \quad \text{with } A_1 = -A_2 \quad . \quad (5.1.16)$$

As $\nu_2 \rightarrow \nu_1$, what corresponds to a collapse of the hyperfine structure, the emission intensity (as the integrand in Eq. (5.1.15)) vanishes. Under these conditions the double peak structure is being transformed into a pseudo-single line, which shape is given approximately by the following expression

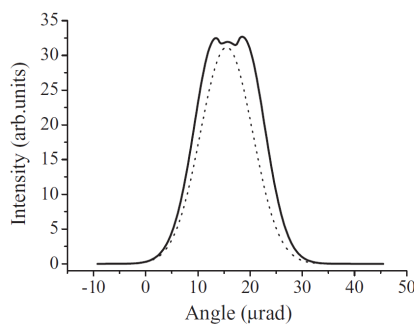


Figure 5.1.6

Angular distribution of the emitted γ radiation - solid line; angular distribution of the exciting synchrotron radiation -dots (see text). The first distribution is scaled in intensity for comparison with the second one. The crystal is set at the position of angular dip (top panel in Fig. 5.).

$$L(\nu, \delta) = \frac{\delta^2}{\left[(\nu - \nu_1)^2 + 1 \right]}, \quad (6.1.17)$$

where $\delta = \nu_1 - \nu_2$. Thus the energy distribution is presented in our model by a *Lorentzian-squared function*. The line width in this case is less than Γ_0 , namely $:0.64\Gamma_0$. One should note that the *interference is constructive at the energies lying in between the resonance ones ν_1 and ν_2* , while, in contrast, it is destructive on both left and right outer sides of resonance region (the amplitudes in Eq. (5.1.16) tend to cancel each other over there). Whence, γ -ray emission completely disappears when $\delta \rightarrow 0$ (above Néel temperature). However, in the real case the application of a small external magnetic field restores the antiferromagnet structure of the crystal and γ -ray coherent emission resumes (Chumakov *et al.*, 1986). Due to coherent effects the real width of the energy distribution Γ_{coh} can be larger than Γ_0 .

To obtain the energy distribution of the emitted γ radiation at the angle of incidence of x_p one should calculate the following integral

$$\tilde{I}_{x_p}(\nu) = \int_{-\infty}^{+\infty} dx F(x, x_p) \cdot I(x, \nu) \quad . \quad (5.1.18)$$

All the values entering into Eq. (5.1.18) are defined above. Several energy distributions of γ radiation emitted near Néel temperature at different angles of incidence of the SR are displayed in Fig. 5.1.7. The central part of the emission angular function around $x_p = 15.5 \mu\text{rad}$ is shown on the upper panel in Fig. 5.1.7, where the considered angular interval is limited by the L,R bars. It is mostly the region in between the two humps of the angular curve. The divergence of the exciting SR beam is taken as $5 \mu\text{rad}$.

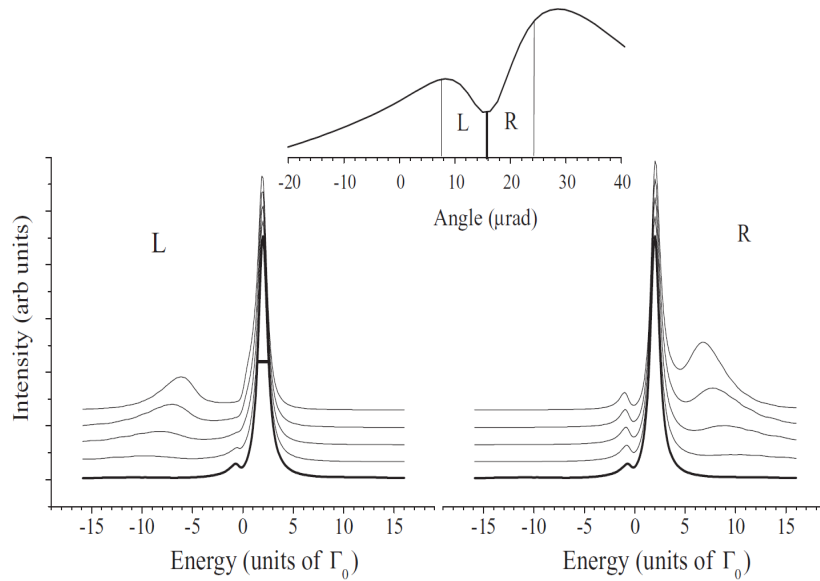


Figure 5.1.7

Energy distributions of the emitted γ radiation at different angles of incidence of the exciting SR in the vicinity of the dip zone of the emission angular function for the (333) reflection and for the internal magnetic field of 2 kOe. The dip zone (taken from Fig. 5.1.5) is shown on the upper panel. The energy distributions on the lower panels refer to the left and the right sides of the dip zone, L and R respectively, as shown on the upper panel. The energy distribution at the exact dip position is displayed on both L,R panels - bold line curves. Each next distribution corresponds to an angular shift of the crystal from the dip position by $5 \mu\text{rad}$. For better visualization the energy spectra are equally spaced along the vertical axis.

The step in change of the angle of incidence is of the same value. The energy distributions of the emitted γ radiation are shown on the lower panels. The distributions corresponding to the shifts towards the lower hump of the emission angular function (to the left of the dip zone) are denoted by L and those towards the higher hump (to the right of the dip zone) are denoted by R . The energy distribution of the emitted γ rays in the case of excitation of the nuclear array at the exact dip position is represented by the bold-line curve on both L and R graphs.

The nature of the double hump structure in the emission angular function prompts the idea to select just the dip zone for obtaining a single line SM radiation spectrum. Indeed, as seen from the figure, in this range it is predominantly a single line having a width close to Γ_0 (horizontal bar on the half-height). A strongly suppressed satellite is noticed on the left-hand side of the main peak. When moving off the center of the angular curve to its left hump a broader line is being formed in the range of the lower energies of the radiation spectrum. Its relative contribution is rising as the angular shift is increasing. When moving off the center of the angular

curve towards its right hump the changes of the radiation spectrum are mostly the same but now a broader line appears at the right-hand side of the central maximum and the small satellite is not smoothing out as in the L distributions. Appearance of the side broad lines in both L and R spectra is due to excitation of the nuclear array at the angles of incidence at which the wings the emission landscape in Fig. 5.1.4c are already touched.

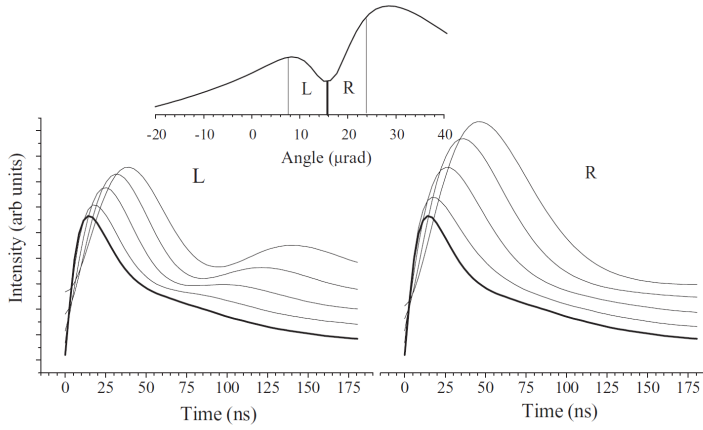


Figure 5.1.8

Time distributions of the emitted γ radiation at different angles of incidence of the exciting SR in the vicinity of the dip zone of the emission angular function for the (333) reflection and for the internal magnetic field of 2 kOe. The dip zone (taken from Fig. 5.1.5) is shown on the upper panel. The time distributions on the lower panels refer to the left and the right sides of the dip zone, L and R respectively, as shown on the upper panel. The time distribution at the exact dip position is displayed on both L,R panels - bold line curves. Each next distribution corresponds to an angular shift of the crystal from the dip position by $5 \mu\text{rad}$. For better visualization the time distributions are equally spaced along the vertical axis.

Finally we come to the angular resolved time distributions of the emitted γ radiation. They were calculated by performing the following integration

$$\tilde{I}_{x_p}(t) = \int_{-\infty}^{+\infty} dx F(x, x_p) \left| \int_{-\infty}^{+\infty} dv E(x, v) \exp\{ivt/2t_0\} \right|^2, \quad (5.1.19)$$

where t is real time and $t_0 = \hbar/\Gamma_0$ is the natural lifetime of the excited nuclear state. The inner integral represents the inverse Fourier transform of the energy distributions of the emitted radiation amplitudes. The obtained time distributions are displayed in Fig. 5.1.8. This figure is delineated in the same way as the former one. All time dependences overthere correspond to the energy distributions shown in Fig. 5.1.7. The time dependence of the emitted γ radiation in the case of excitation of the nuclear

array at the exact dip is marked by the bold lines on both L and R graphs. The non-exponential shape of this dependence reveals the true nature of a single line spectrum obtained nearby the Néel point. In fact it is a *pseudo-single line formed in the process of the combined interference of radiation paths in the geometric space, and in energy and spin domains*. In particular, the γ -ray waves emitted by nuclei in the unit cell right upon excitation cancel each other, because these waves are of equal amplitudes and opposite in sign due to the phase shift between them of π at the zero time. The relative phase between the waves is changing due to a difference in their carrier frequencies with time towards their constructive interference, therefore a quantum beat pattern could be observed. However, at the same time the coherent decay of the excited state is proceeding, so that the quantum beat and decay processes are overlapped in time. In our model of interference of the two Lorentzian lines, see Eq. (5.1.16), using the inverse Fourier transform, we can obtain the following time dependence

$$I(t) = 2[1 - \cos(\omega_1 - \omega_2)t] \exp(-t/t_0), \quad (5.1.20)$$

where quantum beating and decay are presented by the pre-exponential factor and the exponential one, respectively. Quantum beat period here is $T = 2\pi/\omega_0/(\omega_1 - \omega_2)$. The resultant pattern depends strongly on the relation between the characteristic times of the two processes, the beat period T and the natural decay time t_0 . *In the case where the beat period and decay time are of the same order the two processes compete.*

In the real case one should consider the relation between the beat period and the characteristic time of the coherent emission t_{coh} . In the vicinity of Néel temperature the beat period T can be several times larger than t_{coh} , since in this temperature range the hyperfine splitting is already fractional of breadth of the coherent resonance line. The transition from destructive to constructive interference proceeds here slower than the decay. In this approximation the following time dependence is valid: $I(t) \approx t^2 \exp(t/t_{coh})$. The form of the time dependences in Fig. 5.1.8 is still determined by the competing processes. Increase of the intensity due to positive-going inter-resonance interference is compensated by the speeded up coherent emission. This competition results in the formation of the emission maximum in the time dependences. When approaching the times of fully constructive

interference most of the stored energy is released already through the incoherent channels (Chumakov et al, 1990).

When moving from the central angular zone towards the humps the time distributions are determined in addition to the discussed reasons by the interference of the narrow central component with the broader lines at the sides in L and R graphs of Fig. 5.1.7.

5.1.6 Summary and conclusion

Electronically forbidden but nuclear-allowed Bragg reflections can be employed to generate the recoilless γ radiation by exciting nuclear array to its isomer level with the help of the synchrotron radiation. Pure nuclear reflections exist owing to a strong spin dependence of nuclear scattering in the presence of hyperfine fields in crystals. This way a source of Mössbauer radiation alternative to the radioisotope sources can be realized. The coherent excitation of the nuclear array leads to the creation of nuclear exciton polariton states which generate at the exit of the crystal the coherent γ radiation free of a non-resonant contribution.

A particular case of pure nuclear reflection is considered where a single line ^{57}Fe Mössbauer radiation is generated. It is accomplished in an antiferromagnet $^{57}\text{FeBO}_3$ crystal (Iron Borate (IB) crystal) heated up to the vicinity of its Néel temperature.

When considering the interference of radiation while nuclei in the unit cell of the IB crystal de-excite one can find 48 contributions into the interference amplitude. Two contributions come from the de-excitation of the two nuclei present in the unit cell. Each of them contains six contributions in the energy domain where nuclear levels are split due to combined magnetic and electric hyperfine interaction in the IB crystal. Finally near Néel point where the magnetic dipole and electric quadrupole interactions in the IB crystal are of comparable strength the nuclear sublevels in the excited state become strongly mixed in spin projections. The two projections of nuclear spin are allowed at each sub-level. Therefore each of the 6 contributions in the energy domain involves in addition the 4 contributions in the spin domain. Thus the combined multi-path interference in geometric space, in energy, and spin domains

results in the formation of a pseudo single line resonance structure which provides a basis for performing a single line synchrotron Mössbauer (SM) source.

Mutual interference of the propagating and Bragg reflected waves inside the crystal produce a resultant wavefield (WF) with standing wave type structure. In this way the standing wave mode of the nuclear exciton polariton is realized under conditions of Bragg diffraction. One obtains two solutions for the WF amplitudes. Both are modulated in the direction perpendicular to the reflecting planes in such a way that the *WF1 experiences an anomalously weak nuclear absorption*, while the *WF2 on the contrary - an anomalously strong absorption*. In the limit of a semi-infinite crystal only the WF1 survives. A strong suppression of inelastic scattering channels for this wavefield is favoring an enhanced γ -ray emission nearly without internal conversion. At the exit of the crystal a coherent beam of resonant γ radiation is formed.

For nuclear resonant Bragg reflections the emission from a crystal containing a nuclear array exhibits a combined angular and energy dependence. In the case of the IB crystal the dependence undergoes a dramatic change in heating the crystal from room to Néel temperature. Near Néel point its shape is transformed significantly both in energy and in angular dimensions. The multi-line spectrum of the emitted radiation collapses while the angular range of emission extends. In the vicinity of Bragg angle a pseudo single line resonance structure is formed which is created by the inter-nuclear interference (in geometrical space) as well as by a strong inter-resonance (in energy domain) and intra-resonance (in spin-domain) interference of radiation components.

The emission angular function, which represents the emission intensity for different angular settings of the crystal near Bragg angle in the approximation of a plane incident wave, strongly broadens and transforms to a double-hump structure with a central dip in between of the peaks. The breadth of the angular distribution increases by more than one order of magnitude in heating the crystal from room to Néel temperature. However, in the very vicinity of Néel temperature the saturation in angular breadth sets in. Most interesting is the double hump shape of the angular distribution in this range. The two emission branches originate due to the Lorentzian form of the scattering amplitude. Off resonance, the nuclear scattering amplitude is approximately real. The latter being an uneven function of energy deviation off resonance is responsible for existence of the two wings for the emission function on

the angular-energy plane in Fig. 5.1.4 (see also ref. van Bürck *et al.*, 1980). There is a gap in the vicinity of Bragg angle where the wings are negligibly weak. Just in this angular range the spectrum of the emitted radiation consists predominantly of a single line having a width about the natural resonance linewidth Γ_0 . The time distribution reveals the true structure of the single line spectrum of the emitted radiation. In fact the single line consists of two unresolved lines of the hyperfine structure in the vicinity of Néel temperature. Due to the transition from the destructive mode of interference between the hyperfine components to the constructive one an initial rise of intensity is observed. However, competing process of nuclear de-excitation prevents reaching the conditions of the entirely constructive interference. And when finally the times of the constructive interference come most of the energy stored by nuclei turned out to be released already through the incoherent channels (Chumakov *et al.*, 1990). By this reason the time distributions exhibit a broad maximum of low intensity.

The analysis of the coherent emission of γ rays from crystal of iron borate, and namely, of the emission angular function, the energy and time distributions of the emitted radiation is necessary for further elaboration of the ^{57}Fe Synchrotron Mössbauer Source - the device which provides a collimated beam of intense and polarized γ radiation in an energy bandwidth of nano-electronvolts, the nuclear resonance natural level width.

5.2 Angular dependencies of spectral and temporal distributions of Nuclear resonance radiation of synchrotron-based ^{57}Fe Mössbauer source.

V. Potapkin^{1,3*}, A.I. Chumakov^{1,2}, G.V. Smirnov², R. Rüffer³, C. McCammon³, L. Dubrovinsky³

¹*European Synchrotron Radiation Facility, BP 220, F-38043 Grenoble, France*

²*Russian Research Center "Kurchatov Institute", 123182 Moscow, Russia*

³*Bayerisches Geoinstitut, Universität Bayreuth, D-95440 Bayreuth, Germany*

**-corresponding author*

published in *Physics Review A* (2012) **86** 053808

5.2.1. Abstract

We have experimentally studied emission of γ -ray photons by synchrotron-radiation-excited ^{57}Fe nuclei in iron-borate crystal. The crystal was set in the vicinity of the Bragg angle for pure nuclear diffraction of synchrotron radiation. The electronically forbidden but nuclear-allowed reflection (333) was employed to extract nuclear scattering signal. The isolation of nuclear scattering was possible due to two natural reasons. First, in contrast to phase in Rayleigh scattering, the phase in nuclear resonant scattering depends on the direction of the magnetic moment. Second, the iron atom spins in $^{57}\text{FeBO}_3$ crystal are antiferromagnetically ordered. Being flash like excited by synchrotron radiation nuclei in the crystal emits afterwards their own recoil-free radiation within a narrow angular span. The emission angular dependence was measured with highly collimated beam by setting the crystal in different angular positions near the Bragg angle. At room temperature the angular dependence of the emission intensity has a form a single symmetric maximum. But when approaching the Néel temperature, the angular dependence of the emission intensity has transformed dramatically in shape and width. The maximum strongly broadens, splits and acquires a double-hump shape. The energy and time distributions of the emitted radiation appeared to be strongly dependent on the crystal setting within the emission angular range. The experimental measurements are fully consistent with theoretical

predictions. The obtained results can be used in developing of new synchrotron radiation based technique with neV resolution.

5.2.2. Introduction

A nuclear array in a crystal represents for γ radiation with energy in the keV-diapason a resonating three-dimensional grating. Therefore spatial interference in resonant scattering of γ rays by the nuclei can occur like in the case of X rays diffraction. When the incident wave meets the planes of nuclei at the correct angle for reflection a reflected wave is built up due to constructive interference.

The flash-like excitation of nuclei by the synchrotron radiation (SR) leaves the nuclei for free de-excitation afterwards. The SR-excitation is shared by all nuclei in accord with the quantum mechanical principle of superposition of states. Such excitation state can be perceived as a nuclear polarization wave. Inside a crystal, the nuclear polarization wave and the radiation field, which is built up during nuclear de-excitation, are tightly coupled and form together a self-consistent dynamical system, called nuclear exciton polariton or nuclear polariton (Smirnov *et al.*, 2011). As the nuclear polariton is developing, a γ -ray photon can be re-absorbed and re-emitted by nuclei several times. At the border of the crystal, the nuclear polariton generates a beam of the delayed coherent γ radiation in the direction of Bragg reflection. However, when diffraction on electrons of the same atomic planes also occurs, the delayed γ radiation is preceded by a high-intense x-ray pulse providing a huge non-resonant background completely hiding the nuclear signal.

But luckily thanks to the properties of nuclear resonant scattering a way to obtain the pure nuclear signal still exists. The solution is offered by the Bragg reflections which are electronically forbidden owing to the crystal structure but nuclear-allowed due to a specific polarization dependence of nuclear scattering amplitude in the presence of hyperfine interaction. Distinctive case of pure nuclear reflection (PNR) is realized in antiferromagnetic crystals, particularly, in hematite (Smirnov *et al.*, 1969) and iron-borate (Smirnov *et al.*, 1980). In those crystals the sensitivity of nuclear scattering to the orientation of the magnetic field introduces an additional phase π between waves scattered by two ^{57}Fe nuclei in the

crystallographic unit cell and thus it converts the destructive interference (which prevents reflected wave from building up) between the waves to a constructive one. In this way the structural restriction forbidding reflections from the nuclear lattice is removed providing pure nuclear reflection. But since pure nuclear reflection of that kind exists only if the magnetic moments are ordered, the reflection disappears while crossing over Néel temperature. Properties and behavior of the PNR was thoroughly studied over the years, both below (Rütter *et al.*, 1990; Zelepukhin *et al.*, 1985) and in vicinity of Néel temperature (Smirnov *et al.*, 1986, Chumakov *et al.*, 1990). A special case of a pure nuclear reflection was found in (Zelepukhin *et al.*, 1985; Smirnov *et al.*, 1986), which allows for extraction of a single-line nuclear component of SR. Pure nuclear reflectivity within an energy band of about the natural width of the nuclear level was obtained when an $^{57}\text{FeBO}_3$ single crystal was heated in an external magnetic field to the Néel temperature. As it was shown in (Smirnov, 2000) under these conditions a special case of combined magnetic dipole and electric quadrupole interactions is realized in iron borate allowing for pseudo-single line pure nuclear reflection.

In all preceding works the measurements of the spectral properties and the time distributions of the pure nuclear reflections were angular integrated, i.e., performed using quite large divergence of the incident beam. But recently presented theoretical work (Smirnov *et al.*, 2011) shows that the spectral and time distributions of radiation reflected by nuclei in iron borate in vicinity of Néel temperature has a strong dependence on the angle of incidence of synchrotron X-rays.

Here we present an experimental study of energy and time distributions of γ radiation for pure nuclear reflection near Néel temperature T_N . The study was performed differentially over angle, i.e., with negligible divergence of the incident beam. In our measurements a highly perfect antiferromagnetic $^{57}\text{FeBO}_3$ crystal was used. Preliminarily, the emission angular dependence was measured with high precision by setting the crystal in different angular positions relative to the exciting synchrotron radiation beam near the Bragg angle. Further on, the energy and time distributions of the emitted gamma radiation were investigated at the various characteristic angles in the obtained angular dependence. The obtained distributions

were compared with the theoretical predictions. The performed study can be useful for developing of new synchrotron-based techniques with neV resolution (Mitsui *et al.*, 2009; Potapkin *et al.*, 2012).

5.2.3. Experimental Methods

The experiment was conducted during 7/8 mode of the storage ring operation at the Nuclear Resonance Beamline (ID18) (Rüffer & Chumakov, 1996) at the European Synchrotron Radiation Facility. For this mode 7/8 of the storage ring is filled with electron bunches and 1/8 of the storage ring is empty apart from a single bunch in the middle of this region. In 7/8 mode nominal current is 200 mA. 4 mA is being a share of single bunch. The time distributions were measured in 176 ns time interval after a single bunch, which was free from electrons. Measurements of angular dependences and energy distributions were performed using photons generated by all bunches of the storage ring.

The optical scheme of the experiment consisted of several elements. First element was a high-heat-load monochromator (HHLM), which decreases a bandwidth of an undulator synchrotron beam to ~ 2 eV. The second element was high-resolution monochromator (HRM), which decreases the bandwidth of the beam to ~ 15 meV. The primary role of this cascade of monochromators (HHLM+HRM) is to decrease a heat load on iron borate crystal in order to avoid temperature gradient over the crystal. The third element was compound refractive lens (CRL), which were placed between HHLM and HRM. CRL were used to decrease divergence of the incident beam from 20 to 2 μ rad. Small divergence of the incident beam allows to study angular properties of pure nuclear reflection differentially over angle. The beam after HRM was incident on $^{57}\text{FeBO}_3$.

The crystal was located in furnace, which was mounted on a standard Mössbauer transducer (Fig. 5.2.1). The latter was used to modulate energy of the γ radiation coherently emitted by nuclei in the iron borate crystal. Herewith, $^{57}\text{FeBO}_3$ crystal was moved along the plane parallel to its surface and hence to the reflecting planes of nuclei. The nuclear reflection occurs over a range of crystal settings. Therefore the transducer was mounted on an angular stage, which allowed to change

Synchrotron Mössbauer source.

the crystal setting relative to the incident beam. The relevant angular dependence of the reflection intensity is referred as rocking curve.

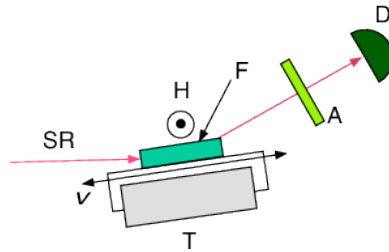


Figure 5.2.1

Schematic view of the experimental set-up. SR - beam after HRM; T, Mössbauer transducer which used for oscillation of the crystal; F - furnace combined with magnets arrangement, which contains $^{57}\text{FeBO}_3$ crystal; H - magnetic field of 110 eO; A - standard single line absorber $\text{K}_2\text{Mg}^{57}\text{Fe}(\text{CN})_6$; D - APD detector.

The beam reflected from the crystal was incident onto a single line absorber (A) and then to detector (D) (Fig. 5.2.1). To monitor the energy distribution of γ radiation emitted by the iron borate crystal we used a standard Mössbauer $\text{K}_2\text{Mg}^{57}\text{Fe}(\text{CN})_6$ single line absorber, which had an area density of resonant ^{57}Fe isotope of 50 mg/cm^2 and line width of $2.1 \Gamma_0$ (Γ_0 is the natural width of the resonance line). All measurements were performed for (333) PNR of the iron borate crystal. Because there is no difference in physics of nuclear scattering between different PNR in $^{57}\text{FeBO}_3$, the obtained results are applicable to any of them, with a correction on the difference in the rocking curve width for each reflection.

The external magnetic field of 110 Oe was applied to the crystal in the direction normal to the scattering plane in order, first, to maximize the reflection coefficient, second, to broaden the magnetic transition region. We used the furnace and the magnets arrangement of a special construction (Potapkin *et al.*, 2012) in order to avoid gradient of the temperature and of the magnetic field. Thanks to the very strong suppression of electronic scattering for PNR (10^{-9}), it was possible to perform all measurements without any gating of the prompt electronic scattering. For more details concerning the experimental setup or crystal environment see Ref. (Potapkin *et al.*, 2012).

5.2.4. Results and Discussion

Fig.2 shows the rocking curve measured at room temperature (a) and at 348.9 K (b), i.e., slightly above $T_N = 348.35$ K. At room temperature, the full width at half-maximum (FWHM) of the angular dependence (Fig. 5.2.2a) was : $10.5(2) \mu\text{rad}$. The theory predicts FWHM of : $5.9(2) \mu\text{rad}$ at room temperature. When the $^{57}\text{FeBO}_3$ crystal was heated approximately to its Néel temperature the rocking curve width grew by a factor of 3, from $10.5(2)$ to $32.1(2) \mu\text{rad}$. Furthermore, the rocking curve acquired double-peak structure (Fig. 5.2.2b). The angular dependence near T_N becomes asymmetric; the peak at the smaller angles is less than that at the bigger angles.

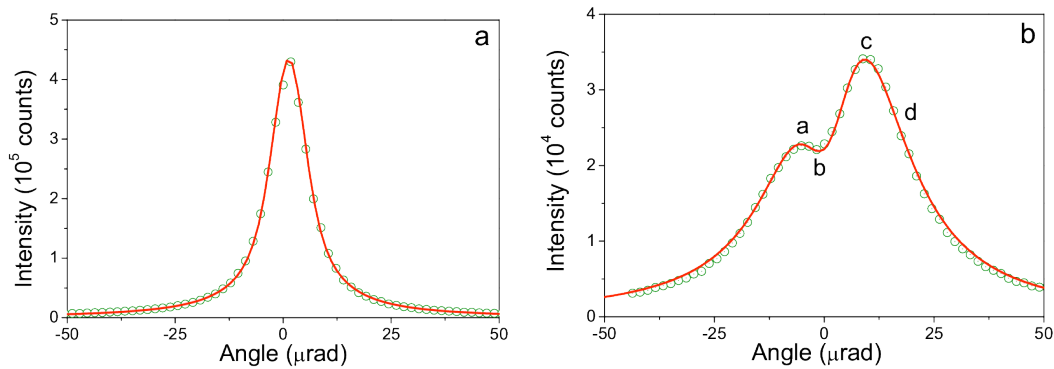


Figure 5.2.2

Angular dependence of the reflected radiation for iron borate (333) pure nuclear reflection of IB crystal (a) at RT (b) 348.9 K. Circles shows experimental points, solid line shows theoretical fit. On figure 2(b) letters (from a to d) mark angular position of the crystal relative to the incident beam in which energy and time distribution was measured.

To compare the experimental results with the theoretical predictions, the experimental data were fit with the use of code based on the theoretical formalism (Smirnov *et al.*, 2011). The two variable parameters were used in the fitting of rocking curves, namely, the internal magnetic field H_{int} and the parameter $\Delta\Theta$ which includes divergence of the incident beam and possible bending of the crystal. In the experiment divergence of the incident beam was fixed. Thus, variation of $\Delta\Theta$ could simulate only bending of the real crystal with respect to the perfect one.

The best fit for the rocking curve at room temperature was obtained with $\Delta\Theta = 5.3(2) \mu\text{rad}$ (H_{int} was fixed to 330 kOe, which is the room temperature value of H_{int} in

Synchrotron Mössbauer source.

H_{int} the iron borate crystals). The increase of the effective divergence from $2 \mu\text{ rad}$ to $5.3 \mu\text{ rad}$ reveals the slight crystal bending. In vicinity of the Néel temperature the best fit for the rocking curve was reached with $H_{\text{int}} = 12 \text{ kOe}$ and $\Delta\Theta = 5.9(2) \mu\text{ rad}$. The obtained value of internal magnetic field was used as fixed parameter for fitting the energy and the time distributions of the emitted γ radiation in the range of the Bragg angle near the Néel temperature.

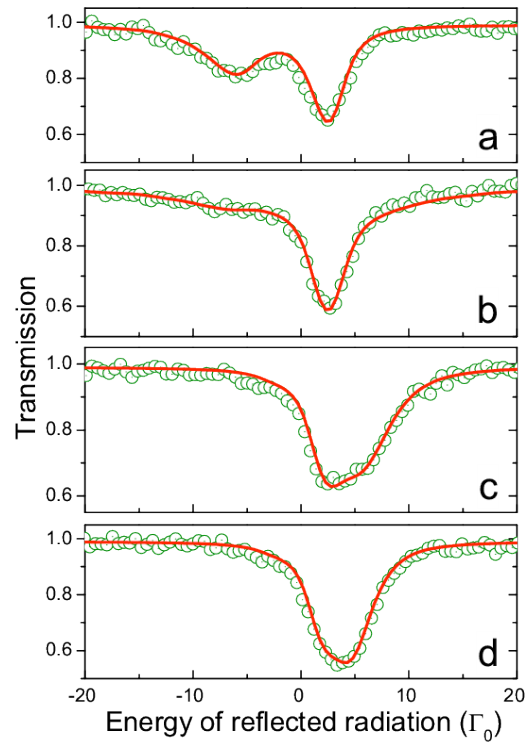


Figure 5.2.3

Energy distributions of nuclear Bragg diffraction for iron borate (333) reflection measured in different angular position of the crystal relative to the incident beam. Olive circles - experimental points, red line - theoretical fit. Energy distribution was measured using standard Mössbauer $\text{K}_2\text{Mg}^{57}\text{Fe}(\text{CN})_6$ single line absorber. Measurements performed at four angular positions (Fig. 5.2.2b): small peak (a), minimum (b), big peak (c) and the right slope of the big peak (d).

The measurements of energy and time distributions were performed at a series of angular positions along the rocking curve. Here we present the measurements taken at the four angular positions indicated in (Fig. 5.2.2b): small peak (a), minimum (b), big peak (c) and the right slope of the big peak (d). Mössbauer spectra of the single line absorber A measured in the given angular positions are displayed in Fig. 5.2.3. With the account for the absorber line contribution the

obtained spectra characterise the energy distributions of gamma radiation emitted at the given angles. The energy distribution in minimum (b) exhibits only one line (Fig. 5.2.3b). For brevity we will call it the main line. The FWHM of this line is : $2 \Gamma_0$ (10 neV). This value was found by subtracting the width of the single line absorber from the measured FWHM. In the angular range of the lower peak of the rocking curve (Fig. 5.2.2a position a), the main line is accompanied by a satellite line (Fig. 5.2.3a) with a smaller energy. The lines are separated by energy interval (ΔE) $\approx 9 \Gamma_0$. With increase of deviation from the Bragg angle the intensity of the low energy satellite increases.

In the angular range of the higher peak of the rocking curve a satellite with the energy larger than the energy of main line appears, see, for example, the two energy distributions taken at the peak and at its right slope (Figs. 5.2.3c,d). The theory predicts that energy of this satellite should be very close to the energy of the main line. Due to the limited energy resolution in the experiment the satellite was not resolved in the measured energy distributions of γ radiation. Only the growing asymmetry of the main line (Fig. 5.2.3c) from the side of bigger energies indicates the presence of the satellite. The difference in energy between the main line and the satellite is $\approx 2.5 \Gamma_0$. The satellite height is rising as the deviation from the Bragg angle increases. In the angular position 'd' Fig. 5.2.2 the satellite even dominates the main line. The energy distribution of the emitted radiation in this angular range looks just like a single broad line (Fig. 5.2.3d).

Fig. 5.2.4 shows the time distributions of the emitted γ radiation in the same angular positions of the crystal relative to incident beam. In the range of smaller angles, for example on the top of the lower peak (position 'a' Fig. 5.2.2), the time distribution (Fig. 5.2.4a) exhibits quantum beats (Rütter *et al.*, 1990), where positions of the maxima are controlled by separation of the main line and the satellite in the energy spectrum (Fig. 5.2.3a). In this particular case the time distribution follows the dependence (Smirnov *et al.*, 2011):

$$I(t) \propto [(1 - \cos(\Delta E * t/\hbar)] \exp(-t/\tau), \quad (5.2.1)$$

where, τ is an effective decay time, which is determined by the coherent gamma-ray emission. The period of quantum beats given by equation $\Delta T = 2\pi\hbar/\Delta E$ is ≈ 98 ns.

Synchrotron Mössbauer source.

Therefore, for the two lines with $\Delta E = 9 \Gamma_0$ the first bump should be located at ≈ 49 ns and second bump at ≈ 147 ns. This is approximately what the measured time distribution shows (Fig. 5.2.4a).

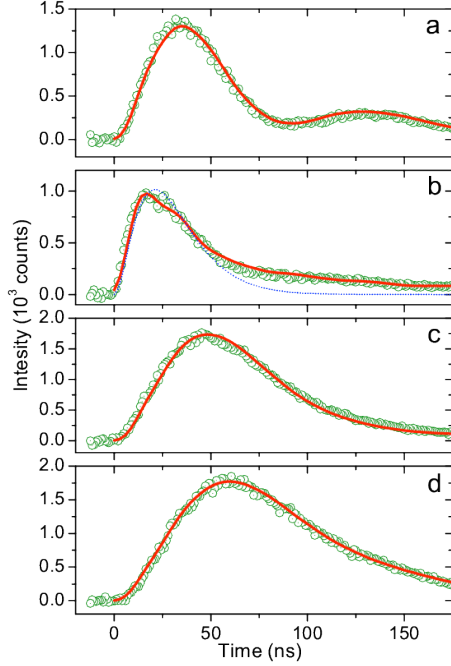


Figure 5.3.4

Time distributions of nuclear Bragg diffraction for iron borate (333) reflection measured in different angular position of the crystal relative to the incident beam. Olive circles shows experimental points, red line - theoretical fit, blue dash line shows fit to data using Eq. (5.2.2). Measurements performed at four angular positions (Fig. 5.2.2b): small peak (a), minimum (b), big peak (c) and the right slope of the big peak (d).

In this case, the quantum beats are dumped due to a shortened lifetime - τ , which is related to an enlarged width of the energy lines Γ as $\tau * \Gamma \approx \hbar$. That's why beats attenuate faster. In the minimum of the rocking curve (position 'b' Fig. 5.2.2) the time distribution does not show an exponential decay (Fig. 5.2.4b), which is expected in case of a Lorentz-like line. This indicates that single line is not a simple Lorentz-like line. In the minimum, the time distribution can be approximated by the dependence (Smirnov *et al.*, 2011):

$$I(t) \propto t^2 \exp(-t/\tau). \quad (5.2.2)$$

In this case bump position is defined by value of τ , i.e., $t_{max} = 2\tau$. The fit to data by Eq. 5.2.2 is plotted by a dash line on Fig. 5.2.2b. Thus, the time distribution in the

minimum of the rocking curve is an overdamped beats case, where quantum beats are overdamped by exponential decay.

In the range of bigger angles, for example in big peak position or right slope (positions 'c' and 'd' on Fig. 5.2.2b) the time distribution shows an intermediate case (Figs. 5.2.4c,d) between overdamped beats case and quantum beats case. There time dependences already do not follow Eq. (5.2.2). In this case, position of the bump is still possibly mainly determined by τ .

One variable parameter was used in the fitting of energy and time distributions of reflected radiation, namely, the angle of incidence Θ_0 of the exciting synchrotron X radiation. The good fit to all the energy and time distributions was obtained, see Fig. 5.2.3 and Fig. 5.2.4. This indicates a good agreement between the experimental results and the theoretical prediction.

The time dependence would follow the Eq. 5.2.1 if the main line is created in the process of destructive interference between two emission lines, in case where energy difference between two lines, i.e. ΔE converge to 0. In such case resulting line doesn't follow Lorentzian distribution. In first approximation, main line can be described by squared Lorentzian distribution (Smirnov *et al.*, 2011):

$$L^2(E) \propto \left(\frac{\Gamma}{(E - E_0)^2 + \Gamma^2} \right)^2, \quad (5.2.3)$$

where Γ is the width of each of the interfering lines and E_0 is a value of resonance energy. However, if the main line would exactly follow the squared Lorentzian distribution, then for main line with width $\approx 2\Gamma_0$, i.e., for $\tau \approx 70$ ns, peak (t_{max}) in time spectra should be at ≈ 140 ns and not at ≈ 25 ns like we have at measured time spectrum (Fig. 5.2.4b). Because, it turns out that in reality the main line is following more complicated dependence. The shift of the peak to lower times indicates that tails of main line dependence drop slower than for squared Lorentzian distribution.

5.2.5. Summary

We have studied properties of gamma radiation emitted by nuclei in iron borate crystal set in the vicinity of Bragg angle for it pure nuclear reflection. It is found that the emission intensity measured at different angular positions of the crystal

relative to the exciting synchrotron radiation beam exhibits extraordinary behavior near the Néel temperature. Approaching Néel temperature, the angular dependence of the emission intensity transforms drastically in shape and width. The rocking curve strongly broadens, splits and acquires a double-peak shape. On the other hand, the energy and time distributions of the emitted radiation strongly depend on the crystal setting in the emission range. In particular, the energy distribution measured in the minimum between the two peaks consist of only one line with width of ~ 10 neV. Analysis of time distribution showed that in first approximation that line obey squared Lorentzian distribution. The obtained results are in very good agreement with theoretical predictions. The results obtained in this work are highly important to for developing of new synchrotron based techniques with requirements for neV bandwidth of incoming radiation.

Acknowledgegments

Authors are grateful to J.-P. Celse for his help with preparation for the experiment. Also we would like to thank Alexy Bosak and Ilya Sergueev for useful scientific discussion during paper preparation.

5.3 The ^{57}Fe Synchrotron Mössbauer source at the ESRF

Vasily Potapkin,^{a,b*} Aleksandr I. Chumakov,^{a,c} Gennadii V. Smirnov,^c Jean-Philippe Celse,^a Rudolf Ruffer,^a Catherine McCammon^b and Leonid Dubrovinsky^b

^aEuropean Synchrotron Radiation Facility, BP 220, F-38043 Grenoble, France,

^bBayerisches Geoinstitut, Universität Bayreuth, D-95440 Bayreuth, Germany, and

^cNational Research Centre "Kurchatov Institute", 123182 Moscow, Russia.

*-corresponding author

Published in *journal of Synchrotron Radiation* Vol 19 part 4 p. 559-569

5.3.1 Abstract

We describe the design of a ^{57}Fe Synchrotron Mössbauer Source (SMS) for energy-domain Mössbauer spectroscopy using synchrotron radiation at the Nuclear Resonance beamline (ID 18) at the European Synchrotron Radiation Facility (ESRF). The SMS is based on a nuclear resonant monochromator employing pure nuclear reflections of an iron borate ($^{57}\text{FeBO}_3$) crystal. The source provides ^{57}Fe resonant radiation at 14.4 keV within a bandwidth of 15 neV, which is tunable in energy over a range of about ± 0.6 μeV . In contrast to radioactive sources, the beam of gamma radiation emitted by the SMS is nearly fully resonant and fully polarized, has high brilliance and can be focused to a 10×5 μm^2 spot size. Applications include, among others, the study of very small samples under extreme conditions, for example at ultrahigh pressure or combined high pressure and high temperature, and thin films under ultrahigh vacuum. The small cross section of the beam and its high intensity allow for rapid collection of Mössbauer data. For example, the measurement time of a spectrum for a sample in a diamond anvil cell (DAC) at ~ 100 GPa is around 10 min; whereas such an experiment with a radioactive point source would take more than one week and the data quality would be considerably lower. The SMS is optimized for highest intensity and best energy resolution, which is achieved by collimation of the incident synchrotron radiation beam and thus illumination of the high-quality iron borate crystal within a narrow angular range around an optimal position of the rocking curve. The SMS is permanently located in an optics hutch and is operational immediately after moving it into the incident beam. The SMS is an in-line

monochromator, i.e., the beam emitted by the SMS is directed nearly exactly along the incident synchrotron radiation beam. Thus, the SMS can be easily utilized with all existing sample environments in the experimental hutches of the beamline. Due to a very strong suppression of electronic scattering for pure nuclear reflections ($\sim 10^{-9}$) SMS operation does not require any gating of the prompt electronic scattering. Thus, SMS can be utilized in any mode of storage ring operation.

5.3.2 Introduction

Conventional Mössbauer spectroscopy has been a valuable tool for decades in studying the magnetic and electronic properties of various materials. However, the technique is not well suited to the study of samples with diameters less than $\sim 100\ \mu\text{m}$. Focusing of radiation from radioactive sources is extremely difficult (Yoshida *et al.*, 2009), and results in a low count rate and a reduction of spectral quality due to an increase of the background. This leads to longer measuring times in order to obtain reasonable quality spectra, and even precludes some studies under extreme conditions, for example the investigation of minerals relevant to the deep Earth at pressures of more than 100 GPa. Thus, the absence of focusing possibilities retards progress in research fields where micron-scale samples are involved, for example, high-pressure geophysics and geochemistry.

The time-domain analog of traditional Mössbauer spectroscopy is realized via time-resolved nuclear forward scattering of synchrotron radiation. Synchrotron radiation has very high brilliance and allows for extreme focusing; hence NFS is an excellent tool to study micron-sized samples. However, NFS is not well suited to study highly complex phases, which contain iron in different spin states, valence states and crystallographic sites. The time spectrum of NFS results from an interference of waves coherently scattered by all iron atoms in the sample; therefore it also contains the cross-terms of the scattering amplitudes of iron atoms in different states. Thus, in order to derive the hyperfine parameters for one iron state or site, one needs to fit the hyperfine parameters of all states. In contrast, absorption, by nature is an in-coherent process, results in an energy spectrum, which is linear superposition of constituent components. In most cases this enables the fitting of each iron site or state independently from all others; hence energy-domain Mössbauer spectroscopy is more suitable for studying highly complex phases. Thus for studies of micron-scale

absorbers with complex Mössbauer spectra, the optimum approach would be to employ high-resolution energy-domain Mössbauer spectroscopy in combination with high brilliance and extreme focusing of synchrotron radiation. In short, what is needed is a synchrotron-based source of Mössbauer radiation.

Such a source can be designed for ^{57}Fe using the properties of pure nuclear reflections of an iron borate crystal. For reflections of this type electronic diffraction is forbidden, but nuclear diffraction is allowed because of a specific polarization factor of nuclear resonant scattering in the presence of hyperfine interactions (Smirnov *et al.*, 1969). Due to magnetic hyperfine splitting of the ^{57}Fe nuclear levels in the ground and the first excited states, the energy spectrum of the reflected radiation consists of several lines. Under these conditions the nuclear array in a crystal behaves as a multiline radiator. This is, of course, an inconvenient property for performing spectroscopic measurements. However, when the iron borate crystal is heated close to its Néel temperature of 348.35 K, the energy spectrum of the reflected radiation collapses to a single line (Smirnov *et al.*, 1986). Under these conditions, a particular case of hyperfine interaction is realized where magnetic dipole and electric quadrupole hyperfine interactions are strongly mixed (Smirnov *et al.*, 2000). The combined multipath quantum interference in space, energy, and spin domains results in the formation of a pseudo-single-line resonance structure in iron borate (Smirnov *et al.*, 2011), which provides the basis for the creation of a single-line Synchrotron Mössbauer Source (SMS). The spectrum of the emitted radiation has an energy bandwidth close to the natural line width of the Mössbauer resonance. The possibility to develop such a source was demonstrated at the European Synchrotron Radiation Facility (ESRF) in 1997 (Smirnov *et al.*, 1997). Later, the same approach was successfully implemented at SPring-8 (Mitsui *et al.*, 2007a; Mitsui *et al.*, 2007b; Mitsui *et al.*, 2007c; Mitsui *et al.*, 2009).

For energy-domain Mössbauer spectroscopy, one needs to scan the energy by changing the relative velocity of the source and the sample using the Doppler effect. In SMS experiments, several methods exist to achieve the Doppler effect. The simplest is to move the sample (Smirnov *et al.*, 1997; Mitsui *et al.*, 2007a; Mitsui *et al.*, 2007b); however this approach is not convenient for most experiments where generally a complicated and/or a heavy sample environment is used. Another possibility is to use an additional silicon crystal before the sample and to achieve the

Doppler shift through motion of this crystal (Mitsui *et al.*, 2007c). This removes the limitation on the sample environment; however the displacement of the Si crystal results in a periodic displacement of the reflected beam and, thus, compromises the focusing. Finally, the Doppler shift can be achieved by moving the iron borate crystal in the plane of the crystal surface (Mitsui *et al.*, 2009). This allows for both preserving the extreme focusing and employing complicated and/or heavy sample environments.

Pure nuclear reflection of the iron borate crystal can be used as either the source of radiation for Mössbauer spectroscopy (Smirnov *et al.*, 1997, Mitsui *et al.*, 2007a; Mitsui *et al.*, 2007c) or as the analyzer of radiation passed through the sample (Mitsui *et al.*, 2007b; Mitsui *et al.*, 2009). The first approach allows for an efficient focusing of the beam on the sample in both horizontal and vertical directions. In contrast, when the crystal is used as an analyzer, the focusing of the beam in one direction is usually omitted, because the iron borate crystal would not accept the highly divergent (focused) beam (Mitsui *et al.*, 2007b; Mitsui *et al.*, 2009), which would lead to a larger spot size and lower count rate. On the other hand, the second approach allows for an easy change in the experiment from collecting SMS spectra to nuclear inelastic scattering (NIS) or NFS, because the change of the technique does not require re-adjustment of the focusing optics and the sample. In contrast, using the iron borate crystal as the source normally implies that both the focusing optics and the sample have to be re-aligned (Smirnov *et al.*, 1997, Mitsui *et al.*, 2007a; Mitsui *et al.*, 2007c).

In this paper, we describe the SMS constructed at the Nuclear Resonance beamline (ID18) (Rüffer & Chumakov, 1996) of the ESRF. The source is optimized for highest intensity and best energy resolution. These qualities are achieved firstly by making use of a highly perfect crystal, secondly by providing a high stabilization of its angular position, and thirdly by using an incident beam of small angular divergence (the necessity of these conditions discussed in paragraph 5.3.2.5). Furthermore, the source is optimized both for extreme focusing and for practical convenience: the iron borate crystal is used as a source, which allows for focusing in both directions. Moreover, the SMS is built as an in-line monochromator: the beam emitted by the source is directed nearly exactly along the incident synchrotron beam; therefore the focusing optics and the sample position require only a small (if any) re-adjustment when moving from SMS to NIS, NFS, or diffraction techniques. This also

allows for easy use of any possible sample environment in the downstream experimental hutches (as high-pressure high-temperature setup, ultra-high vacuum system, cryomagnet, *etc.*). The source is designed to be permanently ready for operation, without complicated and time-consuming preparation. For this purpose, it is located in the optics hutch and is operational immediately after moving it to the incident beam position.

5.3.3 Synchrotron Mössbauer Source

5.3.3.1. Iron borate crystal

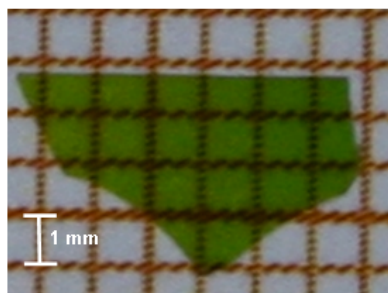


Figure 5.3.1

The high quality single crystal platelet of $^{57}\text{FeBO}_3$ on millimeter graph paper.

The key element of the source that provides neV resolution is the iron borate $^{57}\text{FeBO}_3$ single crystal enriched in the ^{57}Fe isotope up to 95%, grown by Kotrbová *et al.* (1985). One of the high-quality crystals is shown in Fig. 5.3.1. The size of the crystalline platelet is $\sim 5 \times 3 \text{ mm}^2$ and the thickness is $\sim 35 \mu\text{m}$. Iron borate is a canted antiferromagnet with a Néel temperature of 348.35 K. In this crystal, all (NNN) reflections with odd N (*i.e.*, (111), (333), *etc.*) are forbidden for electronic diffraction, while on the other hand they are allowed for nuclear diffraction. These are the so-called pure nuclear reflections. The planes (NNN) are parallel to the platelet surface. Therefore, the considered reflections are the symmetric ones.

5.3.3.2. Pure nuclear reflections

The electronically forbidden but nuclear allowed reflections are employed to extract the nuclear scattering signal. This is possible because of the large difference in the polarization dependence of the electronic and nuclear scattering amplitudes and the antiferromagnetic ordering of iron atom spins in the FeBO_3 crystal. The sensitivity of nuclear scattering to the orientation of the magnetic field introduces an additional phase π between waves scattered by two nuclei in the crystallographic unit cell and thus it converts the destructive interference between the waves to a constructive one (Smirnov *et al.*, 1969). In this way the structural restriction forbidding reflections from the nuclear lattice is removed.

In the presence of hyperfine splitting of the nuclear levels, however, the crystal functions as a multiline nuclear radiator. Such a source is obviously not convenient for spectroscopic studies. Yet a special case of combined magnetic dipole and electric quadrupole interactions can be realized in iron borate close to its Néel temperature in the presence of a weak external magnetic field, where a single line spectrum of emitted radiation can be obtained (Smirnov *et al.*, 1986; Smirnov, 2000; Smirnov *et al.*, 1997; Mitsui *et al.*, 2009). The energy width of the emitted line is close to the natural width of the Mössbauer resonance and is very sensitive to the temperature and magnetic field applied across the crystal (Smirnov *et al.*, 2011). Therefore, in order to avoid inhomogeneous broadening of the source (for an optimal operation of the SMS), a high degree of homogeneity of both temperature and external magnetic field over the iron borate crystal is required.

5.3.3.3. Furnace

The design of the furnace is optimized for homogenous temperature distribution. Fig. 5.3.2a shows a general view of the furnace with the attached magnet holder. Heating is provided by two thermo-foils, which are attached from the inside to the bottom part and to the upper cover (Fig. 5.3.2b). In order to decrease air convection, the furnace has a small and enclosed heating volume with Kapton foils to cover the windows. The temperature gradient was estimated by comparison of the time spectra of radiation reflected from different parts of the crystal. The time spectra were observed to be rather sensitive to temperature, while the estimation did not

reveal any temperature gradient within an accuracy of 0.03 K over 0.2 mm. The total weight of the furnace with attached magnets is 44 g.

The temperature is measured by a Pt100 temperature sensor, which is located inside the crystal holder, close to the bottom heating foil. The stability of the temperature control is about 0.01 K.

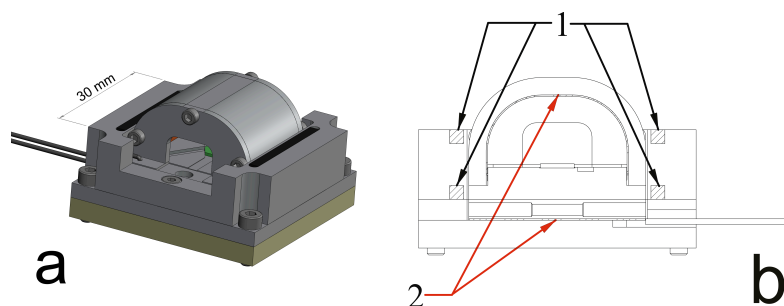


Figure 5.3.2

The furnace for the iron borate crystal: (a) a general view of the furnace; (b) a cross section of the furnace: 1 – the array of four permanent magnets; 2 – the heating elements located in both the crystal support and in the furnace cover.

5.3.3.4. Magnetic field

An external magnetic field is applied to the iron borate crystal for two reasons: firstly, an external magnetic field is required in order to align the magnetic hyperfine field in the plane of the crystal at the scattering plane. This orientation corresponds to a maximum reflection coefficient. Iron borate is a canted antiferromagnet, and the external field needs to be applied perpendicular to the scattering plane in order to correctly orient the magnetic hyperfine field. Secondly, the application of an external magnetic field flattens the temperature dependence of the magnetization near the Néel point (otherwise this dependence is too steep) and extends the magnetization to slightly above the Néel point. This enables easier control of the magnetic hyperfine field, and, therefore, of the spectrum of the reflected radiation.

The external magnetic field should be close to homogeneous over the iron borate crystal, because a variation of the external magnetic field causes a change in the shape of the temperature dependence of magnetization. Correspondingly, a variation of the external magnetic field also leads to a change in the internal magnetic field of the crystal. Using results presented in Zelepukhin *et al.* (1985) we calculated that a variation of external field of 5 Oe leads to the same variation in internal field as resulting from a change in crystal temperature of 0.015 K. Our results show that the

minimum step over temperature which leads to variations in energy and time distributions of SMS radiation (i.e., to detectable change of the internal magnetic field) is 0.03 K. Therefore, the accuracy of internal magnetic field control in the temperature scale should be at least ± 0.015 K or in the magnetic field scale ± 5 Oe.

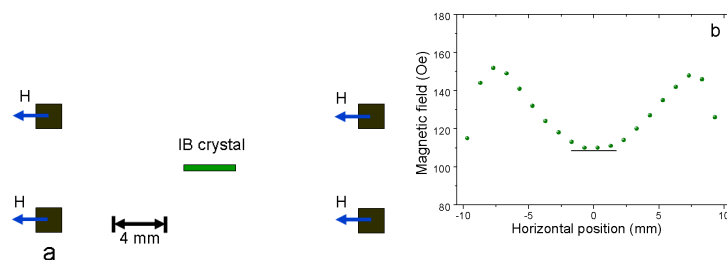


Figure 5.3.3

(a) Geometric arrangement of the permanent magnets. (b) The dependence of the magnetic field (H) on the horizontal position along the crystal surface in the direction perpendicular to the incident beam. The horizontal bar, on both pictures denotes the location of the iron borate crystal.

The external magnetic field on the iron borate crystal is provided by four permanent $\text{Nd}_2\text{Fe}_{14}\text{B}$ magnets located outside the furnace (Fig. 5.3.2b). Calculations show that the array of four magnets provides a significantly more homogeneous field than the one resulting from only two magnets. A schematic view of the magnet arrangement is shown in Fig. 5.3.3a, where the iron borate crystal is located in the centre of symmetry of the magnet system. The average value of the external magnetic field over the crystal is 110 Oe, with a variation over the crystal of ± 4 Oe or $\pm 3\%$ (Fig. 5.3.3b), which is within the requirements of the field homogeneity (± 5 Oe)

5.3.3.5. Angular position

The intensity of a pure nuclear reflection is a nontrivial function of both the energy of the incident radiation and the angle of incidence. Because the energy bandwidth of the incident synchrotron radiation greatly exceeds the energies of the hyperfine interaction, the reflected beam contains all components of the hyperfine structure. Thus, the rocking curve measured in the experiment, i.e., the dependence of the intensity of the reflected beam on the angle of incidence, is the energy-integrated function. Similar to characteristic of hyperfine splitting the shape and width the rocking curve of the iron borate crystal significantly depends on temperature. When the crystal is heated from room temperature to its Néel transition, the angular width of the rocking curve increases by more than one order of magnitude. As found in

Smirnov *et al.* (2011), the rocking curve strongly broadens near the Néel temperature and transforms to a double-hump structure with a central dip between the peaks. The angular position of the dip corresponds to the exact Bragg angle. Near the Néel temperature, the angular width ceases to increase and approaches a finite maximum value (Smirnov *et al.*, 2011).

Examples of the rocking curve measured close to the Néel temperature are shown in Fig. 5.3.4a. The large (~ 40 μrad) angular width of the nuclear reflection is undoubtedly related to the transformation of the Mössbauer diffraction spectrum in the vicinity of the Néel temperature (Smirnov *et al.*, 2011). For instance, it cannot be attributed to a possible curvature of the crystal. This has been verified by measurements at the same temperature of the rocking curve for electronic Umweg reflections (see below). The intrinsic angular width of Umweg reflections can be very narrow; therefore the width of an Umweg reflection measured in the experiment is essentially a convolution of the angular divergence of the incident beam and the effective crystal curvature. Fig. 5.3.4a shows that this value (~ 10 μrad) is much less than the width of the rocking curve of nuclear reflection.

The energy spectrum of radiation reflected by the excited nuclear array strongly depends on the angular position of the crystal relative to the incident beam (see Fig. 7 in Smirnov *et al.* (2011) or 5.1.7 Chapter 5.1). In terms of Mössbauer spectroscopy, this spectrum represents the instrumental function of the SMS. At the centre of the dip between the peaks of the rocking curve (i.e., at the exact Bragg position), the spectrum of the reflected radiation consists predominantly of a single line having a width of about the natural resonance line width Γ_0 (Smirnov *et al.*, 2011). Thus, this angular position provides the optimal instrumental function of the source. When the crystal is detuned from the exact Bragg angle, the tails of the single line appear at the lower and/or the upper part of the energy spectrum (Smirnov *et al.*, 2011). In this case the instrumental function, besides the single line component, contains additional satellite peak(s), which can lead to the appearance of artifacts in the measured Mössbauer spectra.

In the experiment, a finite divergence of the incident beam and/or a certain bending of the crystal lattice may lead to a noticeable weakening of the dip in between the peaks of the rocking curve and hence can cause some angular averaging of the instrumental function over incidence angles with a corresponding deterioration

of its quality. Thus, in order to preserve a good quality of the instrumental function and a high intensity, one needs to have a high quality iron borate single crystal, a small divergence of the incident beam, and a sufficiently accurate rotational stage for precise and stable angular positioning of the crystal.

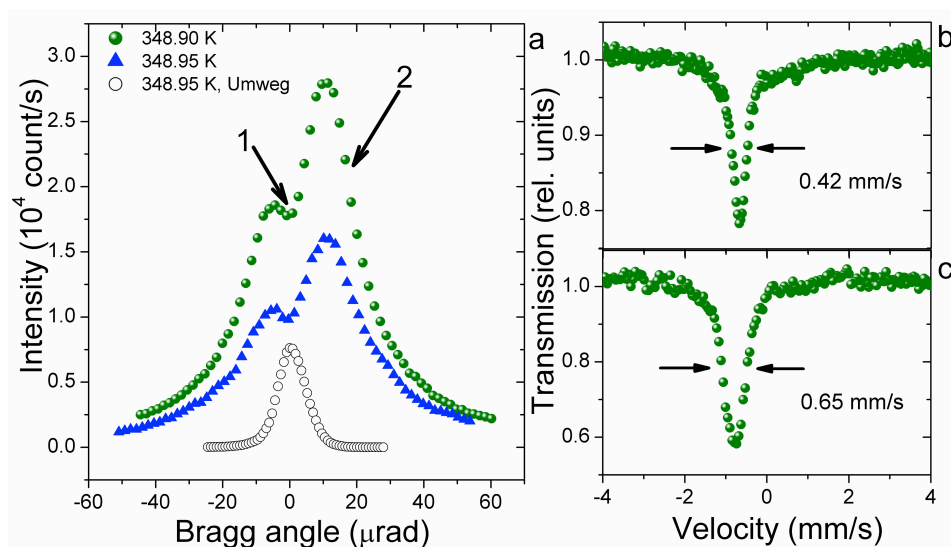


Figure 5.3.4

(a) The rocking curves of pure nuclear (333) reflection (in absolute vertical scale) and of the electronic Umweg reflection (arbitrary vertical scale) of the $^{57}\text{FeBO}_3$ crystal for temperatures in the vicinity of the Néel point. The arrows show the angular positions where the Mössbauer absorption spectra were measured. (b) and (c) The Mössbauer absorption spectra of the single line absorber measured at angular positions 1 and 2, respectively, at a temperature of the iron borate crystal of 348.90 K.

Approaching the Néel temperature, the angular width of the rocking curve increases. Accordingly, the dip between the two peaks of the rocking curve where the single line instrumental function can be obtained, becomes more distinct and broad, making it easier to maintain the crystal at the optimal angular position. Furthermore, the broadening of the rocking curve is accompanied by a narrowing of the energy spectrum of radiation reflected by the crystal at the exact Bragg angle (Smirnov *et al.*, 2011). Thus, increasing temperature improves the instrumental function of the SMS. However, this improvement is accompanied by a strong decrease of the intensity of the reflected radiation; therefore a reasonable compromise between the quality of the instrumental function and the count rate has to be found. Under otherwise equivalent conditions, a good quality of the crystal and a proper collimation of the incident beam should allow one to achieve this compromise at higher intensity.

Fig. 5.3.4a shows the rocking curves of the (333) reflection for two different temperatures in the vicinity of the Néel point. The first rocking curve (green circles) is obtained at the temperature 348.90 K where an optimal compromise between the energy width of the instrumental function and the intensity of the reflected beam is achieved. The second rocking curve shown in Fig. 5.3.4a (blue triangles) is measured at a temperature 0.05 K above the previous one. This small change of temperature increases the width of the rocking curve from 33 μrad to 37 μrad , which slightly relaxes the requirements for collimation of the beam, quality of the crystal, and angular stability. However, this lowering of the tolerance to angular distortions is accompanied by $\sim 40\%$ loss of intensity. Thus, even small improvements of the beam collimation and crystal quality could provide a tremendous gain in the efficiency of the SMS.

The instrumental functions of the SMS were evaluated using a single line $\text{K}_2\text{Mg}^{57}\text{Fe}(\text{CN})_6$ absorber with an area density of the resonant ^{57}Fe isotope of 0.50 mg/cm^2 and a line width of $2.1 \Gamma_0$ ($\Gamma_0 = 0.097 \text{ mm/s}$). Fig. 5.3. 4b shows the absorption spectrum measured when the iron borate was set to the angular position at the centre of the dip on the rocking curve (Fig. 5.3.4a). The obtained line width of $4.3 \Gamma_0$ testifies that the line width of the instrumental function at the optimal angular position is about $2.2 \Gamma_0$ (after absorber width deconvolution).

At the angular positions of both peaks of the rocking curve, the instrumental function acquires undesirable satellite peaks. The same effect happens when the iron borate crystal is not of sufficient quality: the double-peak structure is washed out and the instrumental function measured at the exact Bragg angle acquires satellite peaks due to the effective angular averaging. Under these conditions, a single line absorption spectrum can be obtained at the “backup” angular position at the high-angle slope of the rocking curve (Fig. 5.3.4a). However, the energy width of the instrumental function at the backup position is larger: the measured line width of $6.7 \Gamma_0$ (Fig. 5.3.4c) shows that the line width of the instrumental function is about $4.6 \Gamma_0$ (after absorber width deconvolution).

5.3.3.6. Umweg reflections

Even if a particular reflection is forbidden for electronic diffraction, the X-ray beam may find a way for multiple scattering in the crystal lattice. The X-rays may

experience diffraction on two or more sets of crystalline planes so that the beam is reflected in the same direction as if the reflection would be allowed. Such “bypass” reflections are called Umweg reflections (Renninger, 1937). These reflections are characterized by a broad energy bandwidth typical for electronic diffraction. The Umweg reflections may add intense non-resonant radiation to the reflected beam, thus creating a strong non-resonant background in the Mössbauer spectrum. In order to avoid this background, one needs to escape Bragg conditions for one or more sets of planes involved in Umweg reflections while preserving the Bragg condition for pure nuclear reflection. This can be achieved by rotating the iron borate crystal around the axis of the scattering vector, i.e., by scanning the azimuthal angle of the crystal. For the crystal of iron borate, the azimuthal dependence of the (NNN) Umweg reflections has six-fold symmetry and 12 symmetry points, which correspond to the $[11\bar{2}]$ and $[10\bar{1}]$ crystallographic directions. Fig. 5.3.5 shows the azimuthal dependence of the Umweg reflections in the vicinity of the $[10\bar{1}]$ direction for the (111) pure nuclear reflection. For this measurement, the crystal was heated well above its Néel temperature, where nuclear scattering was completely suppressed and the monitored intensity originated only from electronic scattering of the Umweg reflections. Near the $[10\bar{1}]$ symmetry point, the tails of the neighboring Umweg reflections fortunately cancel each other out (Fig. 5.3.5). Thus, at this particular azimuthal position the non-resonant background in the absorption Mössbauer spectra taken with the SMS is suppressed almost completely.

The intensity of prompt electronic scattering in Umweg reflections is much higher than the intensity of resonant scattering of pure nuclear reflections and may be used to advantage. In particular, with Umweg reflections it is much easier to align the sample inside the DAC to the beam and to adjust focusing optics.

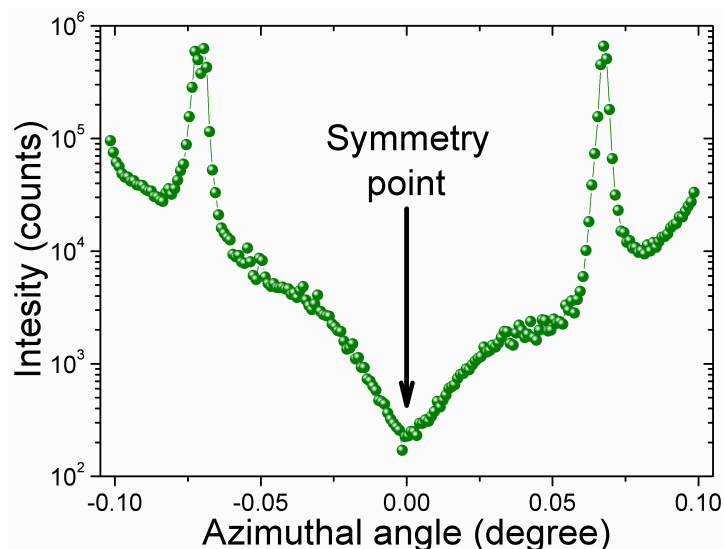


Figure 5.3.5

The azimuthal dependence of Umweg reflections for the pure nuclear (111) reflection of the iron borate crystal in the vicinity of the azimuthal position along the $[10\bar{1}]$ crystallographic direction. The data were taken at 353.15 K.

5.3.3.7. Energy modulation.

The furnace with the iron borate crystal is mounted on a standard Mössbauer transducer, which moves the crystal in the plane parallel to the crystal surface. There are several approaches to understand how the energy modulation of the reflected beam occurs: considering the SMS as a monochromator, one notes that the motion of the crystal along its surface does not change the energy of the X rays. Indeed the utilized pure nuclear (NNN) reflections are symmetric. Therefore, the incoming and outgoing beams form equal angles with the plane of motion and the Doppler shift in frequency of the incoming radiation is compensated by exactly the opposite Doppler shift of outgoing radiation. Thus the frequency of the incoming radiation is transmitted to the same frequency of the outgoing radiation. In the case of electronic scattering the atomic scattering amplitude is constant within the range of the Doppler shift. However, nuclei can only be excited by the frequency equal to their own resonant frequency. By moving nuclei with different velocities, one can effectively change the resonant frequency of the nuclei. The bandwidth of the resonant energy is much less than the range of the Doppler shifts. On the other hand, the bandwidth of incoming radiation is larger than the Doppler shift range. Therefore, nuclei being moved with different velocities effectively select from the incoming beam the

radiation components with different frequencies. In this way the energy modulation of the reflected radiation is achieved. Alternatively, one may consider the SMS as a coherent radiator of nuclear gamma rays. The ^{57}Fe nuclei of the iron borate crystal are excited by the white spectrum of incident radiation for any velocity of the moving crystal. After excitation, the nuclei emit nuclear gamma radiation. The energy of this radiation is equal to the energy of the nuclear resonant transition. Similar to a conventional radioactive source, the translational motion of the iron borate crystal case a Doppler shift and leads to the energy modulation of the emitted radiation.

In contrast to other approaches to obtain the Doppler shift (Mitsui *et al.*, 2007c), moving the iron borate crystal along the plane of the crystal surface has an important advantage: this motion does not cause a spatial displacement of the reflected beam. Therefore, the energy modulation does not compromise focusing and does not shift the beam relative to the sample (Mitsui *et al.*, 2007d).

From the point of view of oscillatory dynamics, ideally the furnace should be located at the centre of inertia of the moving frame of the transducer. However, this requirement is difficult to combine with the diffraction geometry. To allow for diffraction, the furnace is attached to the moving frame above the transducer (Fig. 5.3.6). Under such conditions the frame is obviously not balanced, i.e., its centre of mass is shifted upwards from the axis of the transducer. This shift leads to the appearance of an inertial force torque. Under these conditions, the translation movement of the frame would be accompanied by rocking motions, which would result in a variation of the angle between the incident radiation and the crystal during the crystal motion. This would cause (i) broadening of the instrumental function and (ii) oscillations of the intensity of the reflected beam. Obviously, the quality of Mössbauer spectra with such a source would be significantly lower; firstly, because of diminished energy resolution and secondly, because the base line (i.e., the Mössbauer spectrum collected without sample) would no longer be flat.

In order to avoid these drawbacks, the frame is balanced by a counterweight which is mounted on the bottom side of the frame below the transducer. The distances from the axis of the transducer to the counterweight and to the furnace are equal.

For adjustment of the mass of the counterweight, the furnace is exchanged by a silicon crystal with a mass equal to the mass of the furnace. The angular stability of the frame during its translational motion is evaluated by monitoring the intensity of

the beam reflected by the silicon crystal as a function of the velocity of the frame. With a properly adjusted mass of the counterweight, the measured base line is straight. In order to reach the highest sensitivity of the adjustment, the base line is measured at the half-maximum position of the rocking curve of the silicon crystal.

After adjustment of the counterweight, the estimated residual variation of the angular position of the frame is about $1 \mu\text{rad}$. This is 10 times smaller than the width of the angular range near the exact Bragg angle of the pure nuclear (333) reflection of the iron borate crystal where the single-line spectrum of the instrumental function can be achieved.

5.3.3.8. Mechanics of the SMS

In order to operate the SMS, the following rotations and translations of the iron borate crystal are required: firstly, one needs a very accurate rotation stage to adjust the Bragg angle of the crystal. Secondly, in order to avoid Umweg reflections, an azimuthal rotation is needed. Finally, the tilt rotation of the crystal is needed to keep the reflected beam in the vertical plane. All these rotational stages should be precise and stable. In addition, two translations (a horizontal and a vertical one) are needed to adjust the crystal position relative to the incident synchrotron radiation beam.

Fig. 5.3.6 shows a schematic view of the mechanics of the SMS. The bottom part is a large 2-circle segment (Huber 2-circle segments 5203.80), and the iron borate crystal is located at the centre of rotation of this segment. One circle is utilized for Bragg angle adjustments and is equipped with a 20:1 gear box. The accuracy of angular positioning of this rotation stage is about $0.5 \mu\text{rad}$. The other circle is utilized for tilt angle adjustments; the accuracy of angular positioning of this stage is about $2 \mu\text{rad}$. The vertical translation stage (Huber z-stage 5103.A20-90) is mounted on the 2-circle segment; the accuracy of linear positioning provided by this stage is better than $5 \mu\text{m}$. On the vertical translation stage a wedge is mounted which supports the stage of azimuthal rotation. The wedge angle is equal to the Bragg angle of the chosen pure nuclear reflection of the iron borate crystal. The 1-circle goniometer (Huber 1-circle goniometer 409) is used for azimuthal rotation and is equipped with a 10:1 gear box. The accuracy of angular positioning provided by this rotation stage is about $5 \mu\text{rad}$. The Mössbauer transducer (Wissel MVT-1000) equipped with the frame and the

furnace is mounted on the azimuthal stage. The entire mechanics are mounted on a horizontal translation stage which is used to adjust the horizontal position of the crystal relative to the beam and to move the entire setup in and out of the beam. The accuracy of linear positioning provided by this stage is about $5\ \mu\text{m}$.

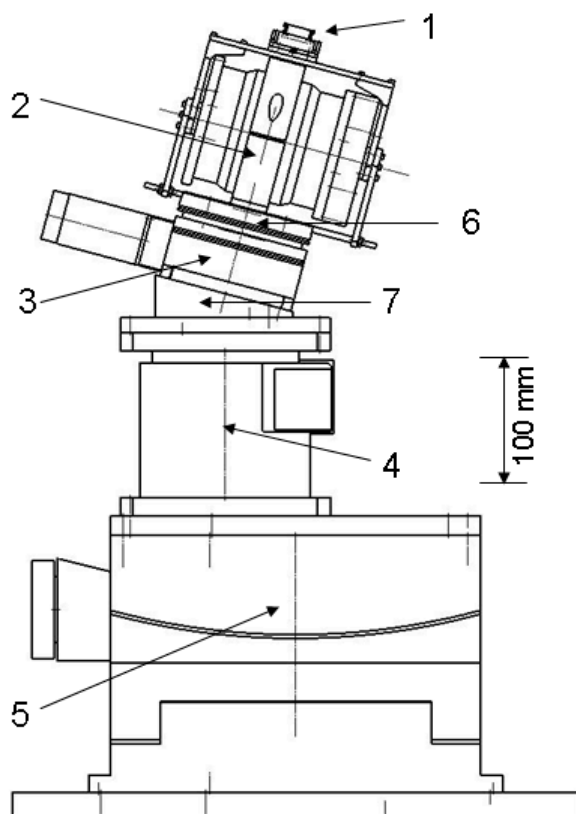


Figure 5.3.6

The mechanics of the Synchrotron Mössbauer Source: (1) furnace; (2) transducer; (3) 1-circle goniometer for azimuthal rotation; (4) vertical translation stage; (5) 2-circle segment for Bragg and tilt rotations; (6) counterweight of the frame; (7) wedge.

5.3.4 Optical scheme

5.3.4.1. In-line setup

Apart from the iron borate crystal, the optical scheme of the SMS includes two additional optical elements. The first optical element is an additional monochromator. The beam after the high-heat-load monochromator is so intense that it may produce a temperature gradient over the surface of the iron borate crystal. In order to avoid the temperature gradient, an additional monochromator is needed whose purpose is to decrease the energy bandwidth of the beam incident to the iron borate crystal and thus

to decrease the heat load. For this purpose the bandwidth can be chosen to be only moderately (not extremely) small. Under these conditions, the additional monochromator can be relatively easily optimized for an essentially high throughput. Therefore, the inclusion of the additional monochromator essentially does not decrease the intensity of the beam provided by the source. The second additional optical element is a deflector. The deflector is needed in order to make the SMS an in-line monochromator. The deflector rotates the beam incident to the iron borate crystal in the vertical plane so that the beam emitted by the crystal is directed nearly horizontally, almost exactly along the synchrotron radiation beam from the high-heat-load monochromator.

The choice of the additional monochromator and deflector depends on the utilized pure nuclear reflection. In this paper, we describe the in-line optical schemes for the (111) and (333) pure nuclear reflections of the iron borate crystal.

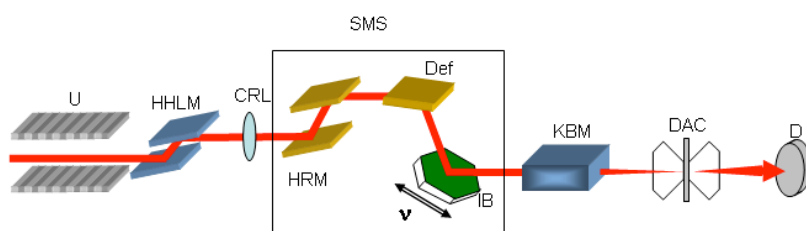


Figure 5.3.7

The optical scheme for a high-pressure experiment with DAC using the Synchrotron Mössbauer Source based on the (333) pure nuclear reflection. U – undulator; HHLM – high-heat-load monochromator; CRL – compound refractive lens; SMS – the Synchrotron Mössbauer Source: HRM – high resolution monochromator, Def – Si (311) deflector, IB – the iron borate crystal inside the furnace with the four magnets and mounted on the Mössbauer transducer; KBM - Kirkpatrick-Baez mirrors; DAC – diamond anvil cell; D – avalanche photo diode detector.

(333) reflection: The pure nuclear (333) reflection of iron borate is convenient for the deflector reflection (311) of silicon. For 14.4 keV radiation, the Bragg angle of the silicon (311) reflection is 15.23 degree and nearly matches that of the iron borate (333) reflection (15.49 degree). Thus, the angle between the beam from the SMS and the horizontal plane is only 0.52 degrees. This enables the beam to reach all downstream experimental hutches and to use all sample environments available at the beamline. This deflector can be easily combined with any additional in-line monochromator. This is a significant advantage of the SMS based on the (333) pure nuclear reflection of iron borate. In this work we use an in-line high-resolution

monochromator (HRM) with a bandwidth of $\sim 15\text{meV}$. It is a double crystal monochromator with two asymmetric (975) reflections of silicon crystals.

Fig. 5.3.7 shows a typical optical scheme for a high-pressure experiment with a DAC using SMS based on the (333) pure nuclear reflection. The undulator (U) is the source of the synchrotron radiation beam. The high-heat-load monochromator (HHLM) decreases the energy bandwidth of the beam to $\sim 2\text{ eV}$, and the compound refractive lens (CRL) is used to decrease the divergence of the beam incident to the SMS. The high-resolution monochromator (HRM) decreases the energy bandwidth of the beam further to $\sim 15\text{ meV}$. The deflector (Def) directs the beam to the iron borate crystal (IB) where the final monochromatization within $\sim 10\text{ neV}$ occurs. The beam from the SMS is focused by the Kirkpatrick-Baez mirrors (KBM) on the sample located in the DAC. The gamma radiation transmitted through the sample is monitored by the avalanche photo diode detector (D).

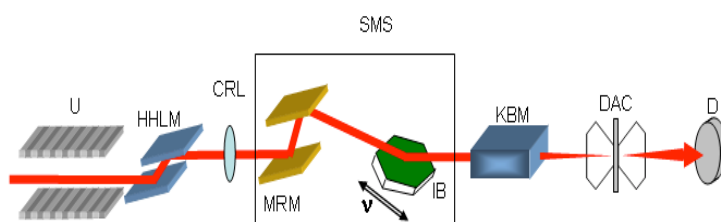


Figure 5.3.8

The optical scheme for a high-pressure experiment with a DAC using Synchrotron Mössbauer Source (SMS) based on the (111) pure nuclear reflection. U - undulator; HHLM - high-heat-load monochromator; CRL - compound refractive lens; SMS - the Synchrotron Mössbauer Source: MRM - deflector and medium resolution monochromator with $\sim 100\text{meV}$ bandwidth, IB - the iron borate crystal inside the furnace equipped with four magnets and mounted on the Mössbauer transducer; KBM - Kirkpatrick-Baez mirrors; DAC - diamond anvil cell; D - avalanche photo diode (APD) detector.

(111) reflection: Another reasonable option for the SMS is the (111) pure nuclear reflection. The angular width of this reflection is three times larger than that of the (333) one. Therefore, the requirements for the angular stability, crystal quality, and collimation of the incident beam are more relaxed. As described above, under otherwise equivalent conditions this helps to achieve a narrower instrumental function and higher intensity. However, the Bragg angle of the (111) reflection is three times smaller than that of the (333) one. Therefore, the area illuminated by the incident beam on the surface of the iron borate crystal is three times larger. Thus, higher quality iron borate crystals are required. Furthermore, for the (111) reflection of iron borate there is no convenient reflection of silicon for the deflector with a sufficiently

close Bragg angle. The deflector for the (111) reflection can be obtained using two reflections: Si(422) and Si(531). The difference between the Bragg angles of these reflections is 5.111 degrees while the Bragg angle of the iron borate (111) reflection is 5.108 degrees. Thus, the beam reflected by the {Si(422) + Si(531)} deflector and the iron borate (111) reflection deviates from the horizontal plane by an angle less than $100\ \mu\text{rad}$. This makes the SMS based on the (111) pure nuclear reflection an in-line monochromator. This deflector also decreases the energy bandwidth to $\sim 100\ \text{meV}$. Thus, it acts both as a deflector and an additional monochromator. The advantage of this setup is that one may combine the SMS experiment with any other technique such as inelastic scattering or diffraction: the beam after the SMS based on the (111) pure nuclear reflection matches the path of the incident synchrotron radiation beam within an accuracy of $100\ \mu\text{rad}$. Thus, one can move the SMS out of the beam and exchange it with any other in-line monochromator without readjusting the focusing optics or sample position.

Fig. 5.3.8 shows the typical optical scheme for a high-pressure experiment with a DAC using the SMS based on the (111) pure nuclear reflection. The medium resolution monochromator (MRM) with silicon reflections Si(422) and Si(531) serves as both an additional monochromator and a deflector. All elements before and after the SMS are the same as for the setup based on the (333) pure nuclear reflection.

Although most of the problems encountered during source development have been solved, there is one unexpected effect that occurs, namely, bending of the initially flat iron borate crystal. The bending appears after about one week of operation and only when the crystal is heated up to its Néel temperature. Although the initial crystal state recovers after a period of relaxation, the bending effect compromises system stability and requires further investigation.

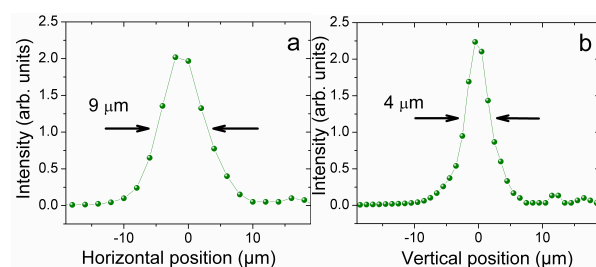


Figure 5.3.9

The profiles and sizes of the focal spot in (a) horizontal and (b) vertical directions. The arrows show the full widths at the half maximum of the profiles.

5.3.4.2. Focusing

In order to focus the beam after the SMS we use Kirkpatrick-Baez mirrors (KBM) (Hignette *et al.*, 2001) consisting of graded Ru/B₄C multilayers on a silicon substrate. The active lengths of the mirrors (150 mm) are essentially large in order to accommodate the entire beam. The focal lengths of the mirrors are 950 mm (for vertical focusing) and 630 mm (for horizontal focusing). The KBM system allows one to focus the beam after the SMS to a spot of about $10 \times 5 \mu\text{m}^2$ with 60% throughput. The profiles and the sizes of the focal spot in horizontal and vertical directions are shown in Fig. 5.3.9.

5.3.5 Properties of the SMS radiation

5.3.5.1. Polarization

Synchrotron radiation is nearly fully linearly polarized; therefore the beam emitted by the SMS is also polarized. For the incident synchrotron radiation, the vector of the electric wave field lies in the horizontal plane. Pure nuclear reflections of the iron borate crystal rotate polarization vectors by 90 degrees. Thus, the beam after the iron borate crystal is also linearly polarized, but the vector of the electric wave field lies in the vertical plane. The polarization of the beam makes the Mössbauer spectra measured with the SMS extremely sensitive to the direction of the electric field gradient (EFG) and of the magnetic field on nuclei. In studies of single crystals, this sensitivity allows for determination of the geometry of the electric field gradient and hyperfine magnetic field. In studies of powder samples, the polarization of the SMS radiation leads to a sensitivity to texture in the sample. For isotropic orientation of crystallites (no texture), the spectra measured with the SMS are identical to those measured with non-polarized radiation. However, in the case where texture is present, the SMS spectra will be different. For quadrupole splitting, preferred orientation of the EFG causes area asymmetry in doublet components. For magnetic splitting, preferred orientation of the magnetic field changes the relative intensity of the spectral lines corresponding to nuclear transitions with a change of the nuclear magnetic moment projection $\Delta m = \pm 1$ and those with a change of the magnetic moment projection $\Delta m = 0$.

5.3.5.2. Shape of the instrumental function

The energy spectrum of gamma radiation from a radioactive source is a Lorentzian distribution:

$$L(E) \propto \frac{\Gamma_0 / 2}{(E - E_0)^2 + (\Gamma_0 / 2)^2},$$

where Γ_0 is the natural width of nuclear resonance, E is the energy of radiation and E_0 is the resonance energy. In contrast, the energy spectrum of radiation emitted by the SMS is the result of the interference of two spectral lines (each with a Lorentzian distribution) with almost equal resonance energies during the collapse of the magnetic hyperfine structure (Smirnov *et al.*, 2011). Therefore, the energy spectrum of radiation emitted by the SMS is a squared Lorentzian distribution (Smirnov *et al.*, 2011):

$$L^2(E) \propto \left(\frac{\Gamma / 2}{(E - E_0)^2 + (\Gamma / 2)^2} \right)^2,$$

where Γ is the width of each of the interfering lines. The knowledge of the exact shape of the energy distribution is important for correct fitting of the measured spectra.

5.3.5.3. Suppression of electronic scattering

For pure nuclear reflection electronic scattering is suppressed almost completely to a level of 10^{-9} . Therefore, non-resonant radiation is a negligible part of the source radiation. For example, in the case of a setup based on the (111) reflection of iron borate, the fraction of non-resonant quanta in the source radiation is around ~1-2%. In the case of a setup based on the (333) reflection, the non-resonant fraction is less than ~0.01%. This is illustrated by the time distribution of photons reflected by $^{57}\text{FeBO}_3$ shown in Fig. 5.3.10. At zero time when synchrotron radiation excites the crystal, there are no prompt quanta of electronic scattering and thus, there is no need to gate electronic scattering. SMS spectra are therefore free from artifacts relating to gating

(Seto *et al.*, 2009), and moreover, SMS can work in any mode of storage ring operation.

5.3.6 Applications

The SMS is well suited to studies of small (micron size) samples which are difficult or impossible to measure with a conventional radioactive source. Therefore, one of the most straightforward applications of the SMS is high-pressure studies with DACs. Using the SMS described in this paper, the spin states of iron in the geologically relevant system of magnesium silicate perovskite $(\text{Mg}_{1-x}\text{Fe}_x)(\text{Si}_{1-y}\text{Al}_y)\text{O}_3$ have been studied as a function of composition and pressure in a range relevant to the lower mantle of the Earth (Potapkin *et al.* submitted).

Data collection time for a Mössbauer spectrum of a sample in a DAC using the SMS is typically three orders of magnitude shorter than using a radioactive source. For example, the measurement of a good quality Mössbauer spectrum of the silicate perovskite sample mentioned above took about 10 min, compared to more than one week using a radioactive point source for the same sample (Potapkin *et al.*, submitted). Moreover, the statistical accuracy of the spectrum measured with a radioactive source is usually lower due to the strong non-resonant background produced by Compton scattering of the high-energy components of the radioactive source. In contrast, the spectrum measured with the SMS is practically free from the non-resonant background, allowing for a higher quality of the spectrum.

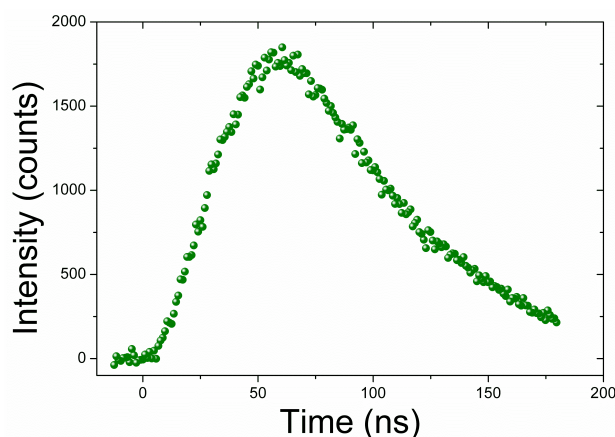
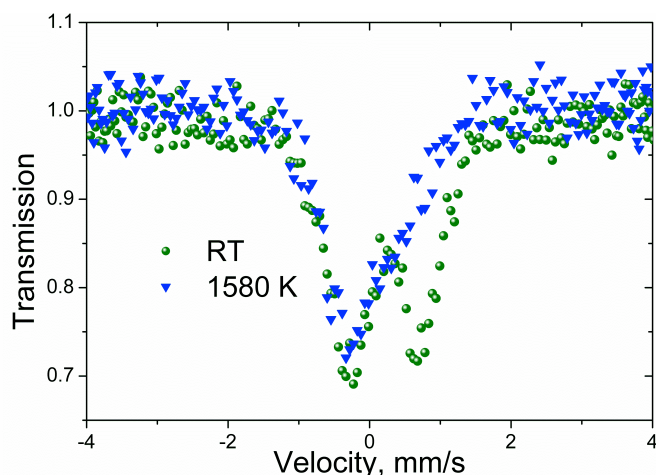


Figure 5.3.10

The time distribution of the photons reflected by $^{57}\text{FeBO}_3$ near its Néel temperature. Zero time corresponds to the moment when the synchrotron radiation excites the crystal.

**Figure 5.3.11**

Spectra of $(\text{Mg}_{0.8}\text{Fe}_{0.2})\text{O}$ ferropericlase at a pressure of 29 GPa at room temperature (green circles) and at 1580 K (blue triangles).

The short measuring time is even more important for combined high-pressure and high-temperature measurements using laser heating. At present, it is difficult for laser heating systems to maintain a stable temperature for long periods of time; hence application of a laser heating system for conventional Mössbauer spectroscopy using a radioactive source is extremely challenging. Thus, the SMS is essentially the only tool available to collect energy-domain Mössbauer spectroscopy at the combined conditions of high temperature and high pressure.

Using the SMS, we have studied several systems at combined conditions of high temperature and high pressure. Fig. 5.3.11 shows two examples of measured SMS spectra of $(\text{Mg}_{0.8}\text{Fe}_{0.2})\text{O}$ ferropericlase. The sample was pressurized in a DAC to 29 GPa and heated using a double-sided laser system to 1580 K, and the measurement time was 10 minutes per spectrum. The room temperature spectrum (green circles) shows a Fe^{2+} doublet, while the spectrum collected at 1580 K (blue triangles) shows a strongly asymmetric singlet. The singlet results from the strong decrease of quadrupole splitting in Fe^{2+} ions with increasing temperature, while the asymmetry is likely due to a temperature gradient in the sample.

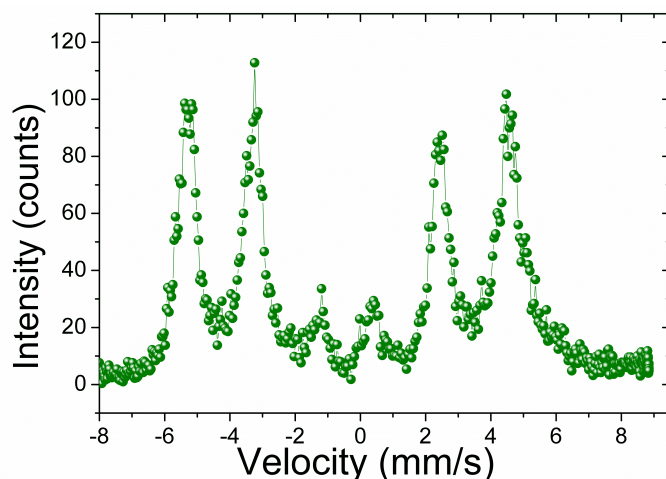


Figure 5.3.12

The SMS spectrum of a ^{57}Fe film with a thickness of 8 nm measured in grazing-incidence geometry during a period of 5 min.

Another application where a small beam size is critical is surface studies, which are usually performed in grazing incidence geometry (i.e., when the incidence angle is close to the critical angle of total external reflection). In order to test the feasibility of such research using the SMS, a ^{57}Fe film on a polished MgO (001) substrate, with a thickness of 8 nm was prepared. The magnetization direction for this film was in the plane of the film and in a direction parallel to [110] axis of the substrate that had an angle of 45 degree to the scattering plane. Fig. 5.3.12 shows the spectrum of radiation scattered from the film measured at the incident angle of 0.35 degrees, which is slightly larger than the critical angle of total external reflection (0.22 degrees). Under such conditions, reflection occurs when the energy of the incident beam is close to the resonant energy. In contrast to Mössbauer spectroscopy in transmission geometry where the spectrum dips below the baseline at resonance energies, in the given reflection geometry the spectrum peaks at resonance energies above an almost negligible baseline (essentially zero); hence the signal-to-noise ratio is extremely high. Thus, a spectrum with a sufficiently high statistical accuracy can be collected during a short time: the spectrum shown in Fig. 5.3.12 was measured during only 5 minutes. In this geometry vertical focusing is needed, otherwise the size of the beam spot is much larger than the sample.

The Nuclear Resonance beamline ID18 is equipped with a UHV facility (Stankov *et al.*, 2008), which allows for *in situ* investigations of surfaces and thin

films. In combination with the UHV facility, the SMS provides the possibility for *in situ* Mössbauer spectroscopy of surfaces and thin films in the energy-domain.

5.3.7 Conclusions

The SMS for energy-domain Mössbauer experiments has been constructed at the Nuclear Resonance beamline ID18 of the ESRF. The bandwidth of radiation provided by the SMS is $\sim 3 \Gamma_0$, the intensity is $\sim 2 \times 10^4$ photons/s and the typical scanning velocity range is about ± 12 mm/s (± 0.6 μeV). In contrast to conventional radioactive sources, the SMS gives the possibility to focus the beam to tens of μm . It is an in-line monochromator, permanently located in the optics hutch and operational immediately after moving it into the incident beam position. The source can be used with all existing sample environments in the experimental hutches downstream of the beamline.

The implementation of this device opens the possibility for studying systems with complex hyperfine structure under extreme conditions, for example under high-pressure. Furthermore, SMS allows for very short collection times of several minutes, which enables use of laser heating. Several high-pressure and high-pressure/high-temperature studies have already been performed. The almost 100% recoilless resonant radiation delivered by the source and its high brightness allows a broad field of SMS applications. Furthermore, SMS can be utilized in any mode of storage ring operation.

Acknowledgments:

The authors would like to thank Ilya Sergeev for help during experiments, for providing computer code for data treatment and for scientific discussions; Marcin Zajac for providing the ^{57}Fe film sample and for help with the surface measurements; Konstantin Glazyrin, Innokenty Kantor, Anastasia Kantor and Ilya Kuppenko for help with the high-pressure/laser-heating studies, Joel Chavanne for modeling of the magnetic system and for providing small permanent magnets, Jean-Pierre Vassalli and Benoit Picut for fabrication of the silicon crystals, and Richard Brand for implementing the version of the computer code NORMOS modified to fit the Mössbauer spectra measured with SMS.

5.4 No spin transition of ferric iron in the lower mantle

V.Potapkin^{1,2}, C.McCammon^{2*}, L.Dubrovinsky², K.Glazyrin², A. Kantor², I. Kuppenko², C. Prescher², R. Sinmyo², G. Smirnov³, S. Popov³, A. Chumakov^{1,3} and R.Rüffer¹

¹European Synchrotron Radiation Facility, BP 220, F-38043 Grenoble, France

²Bayerisches Geoinstitut, Universität Bayreuth, D-95440 Bayreuth, Germany

³National Research Center "Kurchatov Institute", 123182 Moscow, Russia

*-corresponding author

published in *Nature Communication* (2013) **4** 1427

5.4.1. Abstract

Iron has the ability to adopt different electronic configurations (spin states) in the dominant lower mantle phase, magnesium silicate perovskite, which can significantly influence mantle properties and dynamics. Previous studies have suggested that ferric iron (which constitutes at least half of the iron in lower mantle silicate perovskite (McCammon, 1997; Frost *et al.*, 2004; McCammon, 2005)) undergoes a high-spin to low-spin transition (Zhang *et al.*, 2006; Stackhouse *et al.*, 2007; Catalli *et al.*, 2010; Hsu *et al.* 2011; Catalli *et al.*, 2011) which has been suggested to be the cause of some observed seismic velocity anomalies (Catalli *et al.*, 2011; Hsu *et al.* 2011). Here we apply a new synchrotron-based method of Mössbauer spectroscopy to four different compositions of lower mantle silicate perovskite at high pressure and high temperature and demonstrate unambiguously that Fe³⁺ remains in the high-spin state at conditions throughout the lower mantle. Our results rule out the possibility that lateral heterogeneities of geophysical parameters in the mid-lower mantle (bulk sound speed, electrical conductivity) can be explained by iron spin transitions in silicate perovskite, and advocate instead a compositional or thermal variation.

5.4.2. Introduction

The structure of iron-containing magnesium aluminum silicate perovskite (hereafter referred to as FeAlPv) contains two sites, a large 8-12 coordinated site ("A") which is primarily occupied by Mg²⁺ and Fe²⁺, and a smaller octahedral site ("B") which is dominantly occupied by Si⁴⁺ and to a lesser extent by Al³⁺. Although there is disagreement in Fe³⁺ spin transition pressures reported by previous studies, broadly a high-spin (HS) (five unpaired *d* electrons) to low-spin (LS) (one unpaired *d*

electron) transition is predicted when Fe^{3+} occupies the B-site, while $\text{Fe}^{3+}_{\text{A}}$ is predicted to remain in the high-spin state at all pressures throughout the lower mantle (Zhang *et al.*, 2006; Stackhouse *et al.*, 2007; Catalli *et al.*, 2010; Hsu *et al.* 2011; Catalli *et al.*, 2011). Even though Fe^{3+} is predicted to occupy exclusively the A-site in lower mantle compositions of FeAlPv (Vanpeteghem *et al.*, 2006), a HS-LS transition of Fe^{3+} was reported to occur in FeAlPv at high pressure, potentially due to exchange of Fe^{3+} from the A- to the B-site (Catalli *et al.*, 2011, Fujino *et al.*, 2012). Up to now, however, only methods which do not provide an unambiguous interpretation of the data have been used, so we have developed a new method which enables individual spin and valence states to be identified, which provides a clear answer to the question of whether Fe^{3+} undergoes a HS-LS transition in FeAlPv.

5.4.3. Experimental Methods

5.4.3.1. Introduction

Detecting spin transitions of Fe^{3+} in FeAlPv presents a significant challenge. X-ray emission spectroscopy provides information on the bulk spin number, but cannot separate individual contributions. In contrast energy domain ^{57}Fe Mössbauer spectroscopy generally enables an unambiguous resolution of all hyperfine parameters which can be used to infer spin states; however high pressure measurements using conventional radioactive point sources require extremely long counting times (generally more than one week per spectrum). Third generation synchrotron sources offer a solution in the form of time-domain Mössbauer spectroscopy (i.e., nuclear forward scattering); however this method is not well suited to materials with a large number of components (such as FeAlPv) due to the non-uniqueness of fitting models. To solve this problem, we have developed an energy-domain synchrotron Mössbauer source (SMS), which offers a number of advantages: high flux, a beam diameter of a few microns and zero background. SMS allows for rapid measurement of energy-domain Mössbauer spectra under extreme conditions with a quality generally sufficient to unambiguously deconvolute even highly complex spectra (further details of the method are given in the Supplementary Information).

In order to investigate the spin state of iron in lower mantle silicate perovskite, we studied four different silicate perovskite samples: $\text{Mg}_{0.63}\text{Fe}_{0.37}\text{Si}_{0.63}\text{Al}_{0.37}\text{O}_{3+\delta}$ sample #1 (~80% $\text{Fe}^{3+}/\Sigma\text{Fe}$); $\text{Mg}_{0.63}\text{Fe}_{0.37}\text{Si}_{0.63}\text{Al}_{0.37}\text{O}_{3+\delta}$ sample #2 (~70% $\text{Fe}^{3+}/\Sigma\text{Fe}$);

$\text{Mg}_{0.78}\text{Fe}_{0.2}\text{Al}_{0.05}\text{Si}_{0.97}\text{O}_{3+\delta}$ (~50% $\text{Fe}^{3+}/\Sigma\text{Fe}$); $\text{Mg}_{0.94}\text{Fe}_{0.06}\text{SiO}_{3+\delta}$ (~20% $\text{Fe}^{3+}/\Sigma\text{Fe}$). We collected SMS spectra at room temperature and pressures up to 122 GPa using diamond anvil cells, with or without laser annealing of the samples. Details of sample synthesis and experiment methodology are given in the Supplementary Information.

5.4.3.II. Methods

^{57}Fe Synchrotron Mössbauer source (SMS) spectra were collected on beamline ID18 at the European Synchrotron Radiation Facility (ESRF) during operation in uniform mode (7/8 filling) with the beam focused to roughly $10\times 10\ \mu\text{m}^2$ using a Kirkpatrick–Baez mirror. Further details of the SMS method are given in the Supplementary Information. The velocity scale was calibrated relative to α -Fe foil, and spectra were collected over 10-60 min each. Spectra were fitted using the program MossA (Prescher *et al.*, 2012). The dimensionless effective Mössbauer thicknesses were approximately 40 and 20 for the $\text{Mg}_{0.63}\text{Fe}_{0.37}\text{Si}_{0.63}\text{Al}_{0.37}\text{O}_3$ perovskite samples #1 and #2, and 8 and 3 for the $\text{Mg}_{0.78}\text{Fe}_{0.2}\text{Al}_{0.05}\text{Si}_{0.97}\text{O}_3$ and $\text{Mg}_{0.94}\text{Fe}_{0.06}\text{SiO}_3$ perovskite samples, respectively. Further details of sample synthesis and experimental methodology are given in the Supplementary Information.

5.4.4. Results and Discussion

SMS spectra of $\text{Mg}_{0.63}\text{Fe}_{0.37}\text{Si}_{0.63}\text{Al}_{0.37}\text{O}_3$ perovskite, which contains iron dominantly as Fe^{3+} , are extremely well resolved (Fig. 5.4.1). We fit the data to three quadrupole doublets, one assigned to Fe^{3+} and two assigned to Fe^{2+} (high QS and low QS) based on their centre shifts. Visually there appears to be no change to the Fe^{3+} doublet over the entire pressure range (Fig. 5.4.1 and Supplementary Fig. 5.4.S4).

The hyperfine parameters (centre shift [CS] and quadrupole splitting [QS]) in all samples studied are the same within experimental error, and there is no change in $\text{Fe}^{3+}/\Sigma\text{Fe}$ for individual samples over the entire pressure range of the experiment (Fig. 5.4.2). The hyperfine parameters of the Fe^{3+} doublet are consistent with the high-spin state (Gütlich *et al.*, 2011), and their smooth variation with pressure indicates that Fe^{3+} does not undergo any spin transitions within the entire pressure range. Notably the QS value reported for low-spin Fe^{3+} from both experimental (Catalli *et al.*, 2010; Catalli *et al.*, 2011) and theoretical (Hsu *et al.*, 2011) studies (red dashed line, Fig. 5.4.2a) is more than twice our observed values.

The hyperfine parameters of the low QS Fe^{2+} doublet (blue doublet in Fig. 5.4.1) corresponds to the high-spin state (McCammon *et al.*, 2008), while the doublet with high quadrupole splitting (black doublet in Fig. 1) corresponds either to intermediate-spin (IS) Fe^{2+} (McCammon *et al.*, 2008) or a distortion of the site occupied by high-spin Fe^{2+} (Hsu *et al.*, 2011). Irrespective of the interpretation of the Fe^{2+} spin state, our conclusions regarding the absence of a spin transition in Fe^{3+} remain the same.

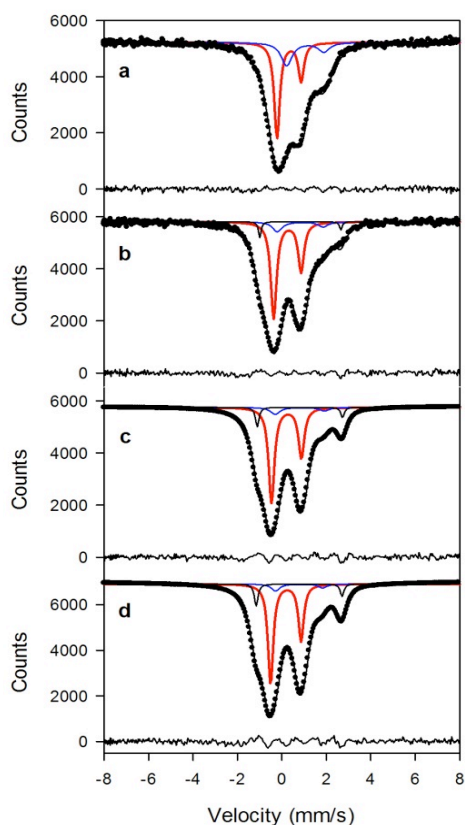


Figure. 5.4.1: SMS spectra of $\text{Mg}_{0.63}\text{Fe}_{0.37}\text{Si}_{0.63}\text{Al}_{0.37}\text{O}_3$ perovskite sample #1 at room temperature showing their evolution with pressure (a) 2.5 GPa; (b) 37.9 GPa; (c) 67 GPa; (d) 93 GPa. The data were fit to one Fe^{3+} doublet (red) and two Fe^{2+} doublets (blue and black), and the fit residual is shown below each spectrum. Area asymmetry is due to preferred orientation of the sample, and the velocity scale is given relative to α -iron.

Single-crystal X-ray refinements (Glazyrin *et al.*, 2011) and crystal chemical calculations (see Supplementary Information) have shown that Fe^{3+} occupies only the A-site of the perovskite structure in our samples; hence our data demonstrate that Fe^{3+}_A does not undergo a high-spin to low-spin transition up to at least 122 GPa. This conclusion is in agreement with results from experimental (Catalli *et al.*, 2010; Catalli

et al., 2011) and theoretical (Zhang *et al.*, 2006; Stackhouse *et al.*, 2007; Hsu *et al.*, 2011) studies. However several studies (Catalli *et al.*, 2010; Catalli *et al.*, 2011; Fujino *et al.*, 2012) have suggested that the reduced volume of LS Fe³⁺_B could lead to a redistribution of Fe³⁺ from the A- to the B-site in the perovskite structure within the lower mantle. To test this hypothesis, we laser annealed our samples at a number of pressures and collected SMS spectra both during and after heating. Visually SMS spectra collected after laser annealing showed no change to those taken before heating (Supplementary Fig. 5.4.S5) and hyperfine parameters remain unchanged (star symbols; Fig. 5.4.2). We therefore conclude that there is no exchange of Fe³⁺ between the A- and the B-site at lower mantle pressures and temperatures, in agreement with the results of a complementary study using high-pressure single-crystal X-ray diffraction with laser heating undertaken on the same composition as two of our samples (Glazyrin *et al.*, 2011).

The coupled substitution $\text{Mg}^{2+}_{\text{A}} + \text{Si}^{4+}_{\text{B}} \leftrightarrow \text{Fe}^{3+}_{\text{A}} + \text{Al}^{3+}_{\text{B}}$ is considered to be the dominant mechanism for incorporation of Fe³⁺ into FeAlPv in the lower mantle (Vanpeteghem *et al.*, 2006; Brodholt *et al.*, 2000; Saikia *et al.*, 2009); hence Fe³⁺ is expected to only occupy the A-site in the perovskite structure for lower mantle compositions. Electrical conductivity measurements of single-phase Mg_{0.9}Fe_{0.1}SiO₃ perovskite and a pyrolite mantle assemblage all show a decrease in conductivity above 50 GPa (Ohta *et al.*, 2008; Ohta *et al.*, 2010a; Ohta *et al.*, 2010b), comparable to the electrical conductivity decrease caused by HS-LS spin crossover of Fe²⁺ in (Mg,Fe)O (Yoshino *et al.*, 2011). The drop in silicate perovskite conductivity has been attributed to a HS-LS transition of Fe³⁺ (Ohta *et al.*, 2008; Ohta *et al.*, 2010a; Ohta *et al.*, 2010b); however the small proportion of Fe³⁺ in the Mg_{0.9}Fe_{0.1}SiO₃ perovskite sample (~ 10%), the results from this study and a companion study (Glazyrin *et al.*, 2012) that there is no shift of Fe³⁺ from the A-site to the B-site at lower mantle conditions, and the overwhelming evidence that no Fe³⁺ spin transition occurs when Fe³⁺ occupies the A-site in FeAlPv implies that the drop in electrical conductivity cannot be attributed to a spin transition of Fe³⁺. A more likely explanation is the pressure-induced HS-IS transition of Fe²⁺ in FeAlPv observed using X-ray emission spectroscopy (Badro *et al.*, 2004) and nuclear resonance methods (McCammon *et al.*, 2004; Lin *et al.*, 2004).

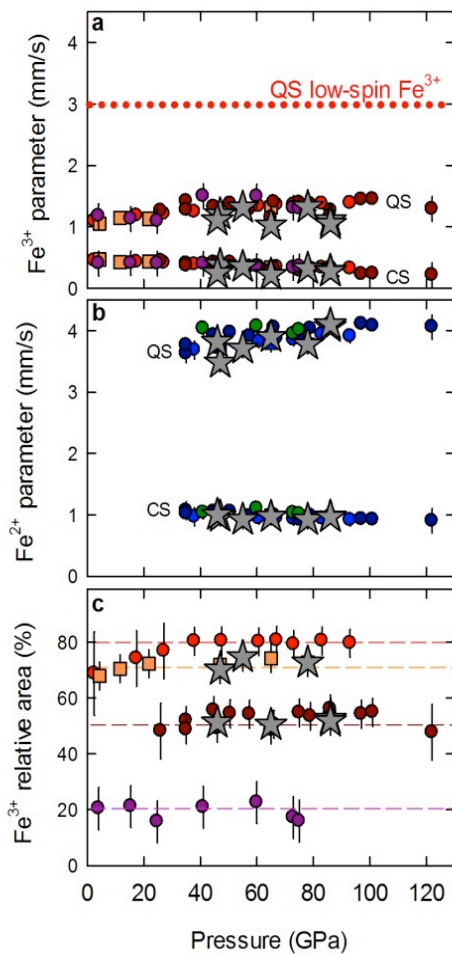


Figure 5.4.2:

Pressure variation of FeAlPv hyperfine parameters (centre shift [CS] and quadrupole splitting [QS]) (a) high-spin Fe³⁺; (b) high QS Fe²⁺. Sample data are indicated as follows: Mg_{0.63}Fe_{0.37}Si_{0.63}Al_{0.37}O₃ perovskite sample #1 (red and blue circles); Mg_{0.63}Fe_{0.37}Si_{0.63}Al_{0.37}O₃ perovskite sample #2 (orange and blue squares); Mg_{0.78}Fe_{0.2}Al_{0.05}Si_{0.97}O₃ perovskite (brown and dark blue circles); Mg_{0.94}Fe_{0.06}SiO₃ perovskite (purple and green circles). The expected quadrupole splitting for low-spin Fe³⁺ is shown as a horizontal red dashed line. (c) Pressure variation of Fe³⁺/ΣFe as determined from the relative areas: perovskite sample #1 (red circles); Mg_{0.63}Fe_{0.37}Si_{0.63}Al_{0.37}O₃ perovskite sample #2 (orange squares); Mg_{0.63}Fe_{0.37}Si_{0.63}Al_{0.37}O₃ perovskite (brown circles); Mg_{0.94}Fe_{0.06}SiO₃ perovskite (purple circles). Horizontal lines are guides for the eye. Values obtained after laser heating of Mg_{0.63}Fe_{0.37}Si_{0.63}Al_{0.37}O₃ perovskite sample #2 and Mg_{0.78}Fe_{0.2}Al_{0.05}Si_{0.97}O₃ perovskite are indicated by grey stars. In all cases, parameters remained unchanged from those before heating within experimental error, demonstrating that there is no high-spin to low-spin transition in Fe³⁺ at the pressure-temperature conditions of the lower mantle.

Electromagnetic induction data offer an important complement to seismic data with respect to lower mantle modeling, since the former are more sensitive to

temperature and iron content, while the latter better constrain the mineralogy (Verhoeven *et al.*, 2009). Laboratory electrical conductivity data of the relevant minerals are an important component of the approach, and it is crucial that they are representative of behavior in the depth range of interest. Earlier laboratory-based electrical conductivity models incorporating FeAlPv conductivity values at the top of the lower mantle reported that electrical conductivity in the lower mantle is relatively homogeneous (Xu *et al.*, 2000), while a more recent model incorporating the latest experimental conductivity values found a decrease in electrical conductivity between 1300 and 1800 km depth (Ohta *et al.*, 2010). Indeed a recent one-dimensional inversion of 32 years of geomagnetic data shows a decrease in conductivity below 1400 km, and a three-dimensional inversion of the same dataset shows variations of more than one order of magnitude in the mid part of the lower mantle, some of which are correlated with fast and slow regions of seismic tomography models (Tarits *et al.*, 2010). Based on the results of this study we can rule out the possibility that seismic anomalies in the mid-lower mantle region are caused by a Fe³⁺ spin transition in FeAlPv, and compressibility studies have already shown that there is no pressured-induced change to elasticity in this depth range for Fe²⁺-rich silicate perovskite (McCammon *et al.*, 2008; Saikia *et al.*, 2009; Lundin *et al.*, 2008). Such variations in electrical conductivity are more likely caused by compositional or temperature heterogeneity, but may also be due to minor phases such as water or carbonates (Tarits *et al.*, 2010). A final resolution of the controversy surrounding iron spin transitions in FeAlPv through Mössbauer spectroscopy (this work) and single crystal X-ray diffraction (Glazyrin *et al.*, 2012) provides an important step in developing quantitative models for joint inversion of electromagnetic and seismic data that place improved constraints on lower mantle mineralogy, composition and thermal state.

Acknowledgements

We acknowledge the European Synchrotron Radiation Facility for provision of synchrotron radiation facilities (ID18) and we would like to thank Jean-Philippe Celse for additional technical assistance and Ilya Sergueev for help with data analysis software. The project was partly supported by funds from the German Science Foundation (DFG) Priority Programme SPP1236, the PROCOPE exchange programme, and the German Federal Ministry for Education and Research (BMBF).

5.4.5. Supplementary Information

5.4.5.I. Synchrotron Mössbauer source

Energy-domain Mössbauer spectroscopy provides direct access to hyperfine parameters from which iron valence and spin state can be determined. It has a large advantage compared to nuclear forward scattering (NFS) and X-ray emission spectroscopy (XES) in that each contribution occupies a nearly unique energy range which generally enables an unambiguous resolution of all components. In contrast, NFS and XES provide bulk information which combines the effects of all contributions. This advantage of Mössbauer spectroscopy makes it an ideal tool to study systems where iron exists in different spin and valence states, and different crystallographic positions.

Conventional energy-domain Mössbauer spectroscopy uses radioactive sources whose brilliance is very low; hence high-pressure studies using diamond anvil cells (DACs) require long measuring times since beam focusing is not possible in a laboratory setting. This reduces the quality of the results due to pressure gradients, increased background, and restricts the maximum pressure at which measurements are possible. These problems can be solved by combining the advantages of high-brilliance third generation synchrotrons (high flux, extreme focusing of the beam) with the resolution of energy-domain Mössbauer spectroscopy to produce a synchrotron source of Mössbauer radiation.

A synchrotron Mössbauer source (SMS) provides a high-brilliance beam of synchrotron radiation with an energy bandwidth of ~ 15 neV. In addition, SMS has several further properties that a radioactive source does not possess. The SMS beam is polarized up to 99%, and it consists 100% of recoilless radiation with zero background. These properties enable rapid and precise measurements of Mössbauer spectra of samples under extreme conditions.

The possibility to develop such a source was first demonstrated at the nuclear resonance beamline ID18 (Rüffer & Chumakov 1996) at the European Synchrotron Radiation Facility (ESRF) in 1997 (Smirnov *et al.*, 1997).

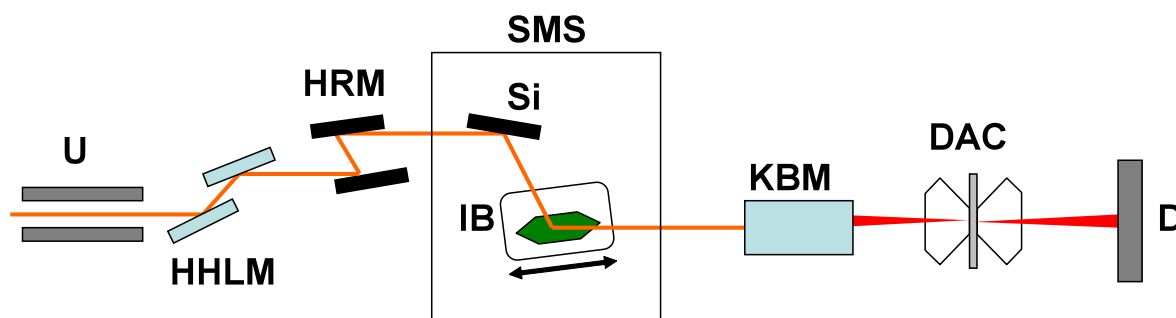


Figure 5.4.S1

Optical scheme for SMS experiment for high-pressure studies. U - undulator; HHLM – high-heat load monochromator; HRM – high resolution monochromator; SMS: Si – Si (311) crystal; IB – enclosed furnace (mounted on a velocity transducer) with the iron borate crystal inside; KBM - Kirkpatrick-Baez mirrors; DAC – diamond anvil cell; D – avalanche photo diode detector.

Fig. 5.4.S1 shows the experimental setup. The synchrotron beam is emitted the undulator (U), passes through high-heat load monochromator (HHLM) with energy bandwidth of ~ 2 eV, and a high-resolution monochromator (HRM) with energy bandwidth of ~ 15 meV. This cascade of monochromators is required to decrease the heat load on the iron borate crystal in order to prevent a temperature gradient. The SMS itself is a monochromator composed of two crystals. The key element of the source is an iron borate crystal (FeBO_3) enriched in the ^{57}Fe isotope. The crystal is used in (333) pure nuclear reflection. For such reflection, electronic diffraction is forbidden, while nuclear diffraction is allowed. The crystal is placed in an external magnetic field of ~ 110 Oe and heated close to its Néel temperature of $\sim 75.65^\circ\text{C}$. Under these conditions the hyperfine magnetic structure collapses to a single line. The crystal therefore reflects synchrotron radiation within an energy bandwidth of ~ 20 neV. Further details of the physics of the process are given in (Smirnov *et al.*, 2011). The furnace is enclosed and special arrangements of the magnets are used in order to ensure homogenous heating and magnetic field for stable operation. The furnace with the crystal inside is mounted on a velocity transducer in order to modulate the energy. The purpose of the Si (311) crystal is to direct the beam exiting the SMS in a direction parallel to the incoming synchrotron beam, which allows for a more convenient installation of different types of sample environment such as DAC, cryostat, furnace, etc. The SMS is followed by a focusing mirror (KBM), which allows focusing of the

synchrotron beam to a roughly $10 \times 10 \mu\text{m}$ spot size on the sample located in the DAC. The transmitted γ -quanta are monitored by an avalanche photo diode detector.

During the SMS experiment the linewidth of the source is controlled before and after each sample measurement using $\text{K}_2\text{Mg}^{57}\text{Fe}(\text{CN})_6$, whose Mössbauer spectrum consists of a single line (Fig. 5.4.S2). The velocity scale is calibrated using $25 \mu\text{m}$ thick natural α -iron foil (Fig. 5.4.S3).

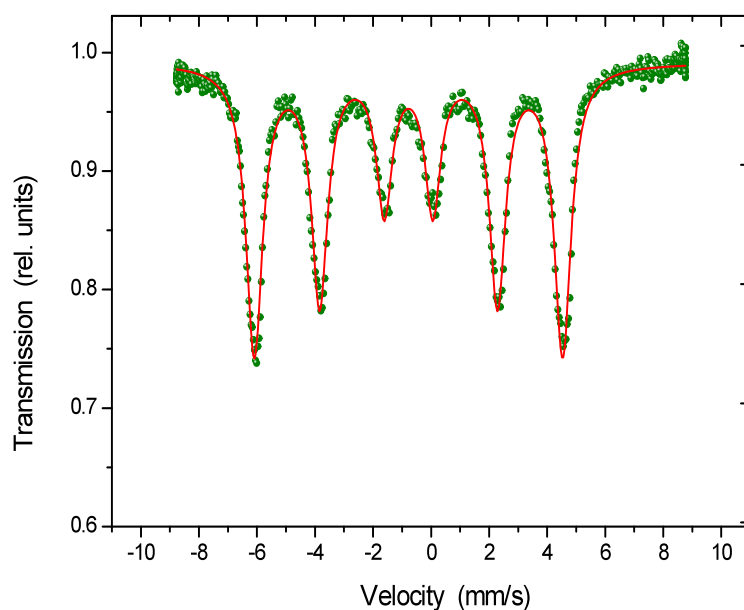
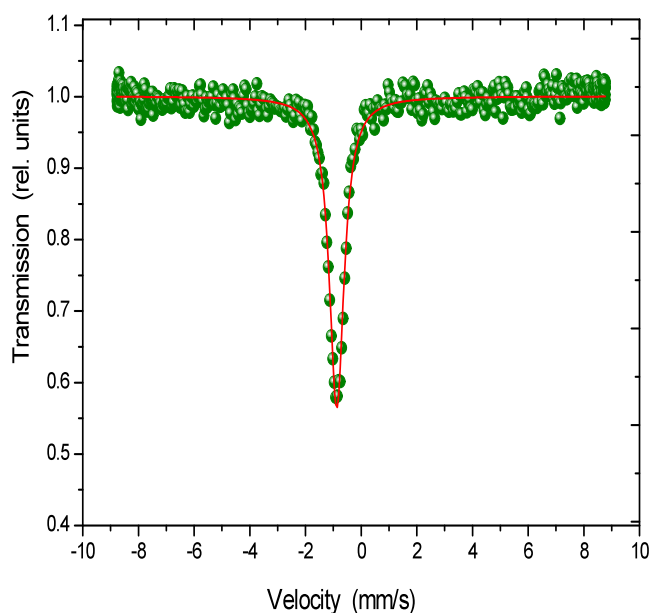


Figure 5.4.S2

SMS spectrum of $\text{K}_2\text{Mg}^{57}\text{Fe}(\text{CN})_6$ used to monitor the source linewidth.

**Figure 5.4.S3**

SMS spectrum of 25 μm thick natural α -iron foil used for energy calibration.

5.4.5.II. Sample synthesis

All silicate perovskite samples were synthesized using a multianvil press. The experiments were performed using Cr_2O_3 -doped MgO octahedra fitted with a LaCrO_3 heater in combination with tungsten carbide cubes following the methodology described in (Keppler & Frost, 2005). Chemical compositions were measured using an electron microprobe (S4850) or a field emission scanning electron microscope (S4949 and S5083). Details of each experiment are given in Table 5.4.S1.

Table 5.4.S1. Experimental details and sample compositions

Run number	S4850	S4949	S5083
Starting material	$\text{Mg}(\text{OH})_2$, SiO_2 , Al_2O_3 , Fe_2O_3	MgO , SiO_2 , Al_2O_3 , Fe_2O_3	MgO , SiO_2 , Fe_2O_3
Pressure (GPa)	25	26	26
Temperature ($^\circ\text{C}$)	1300	1800	1800
Run duration (min)	30	30	50
Capsule	Pt	Re	Re

Run product	Pv, Al-rich hydrous phase, quenched	Pv	Pv
Cation proportions (for 3 O)			
Mg	0.63(1)	0.78(2)	0.94(3)
Fe	0.37(1)	0.20(2)	0.06(1)
Al	0.37(1)	0.05(1)	-
Si	0.63(1)	0.98(2)	1.00(2)
Fe ³⁺ /ΣFe	0.80(5) (sample #1) 0.70(5) (sample #2)	0.50(5)	0.20(8)

5.4.5.III. DAC experiments

Samples for DAC experiments were carefully selected from the run products to be homogeneous under an optical microscope. Small plate-like pieces of the material (typical dimensions $\sim 30 \times 30 \times 15 \mu\text{m}^3$) were loaded together with ruby chips (pressure marker) into the sample chambers of DACs available at Bayerisches Geoinstitut. Diamonds with culets of diameter 120, 250, and 300 μm were used in different experiments depending on the pressure range. The sample chamber was prepared by drilling a hole in a pre-indented rhenium gasket, and the hole was filled with the sample material and the quasi-hydrostatic pressure medium, Ne.

5.4.5.IV. Laser heating

We used a modified and enhanced version of the portable laser heating setup described previously (Dubrovinsky, L. *et al*, 2009; Dubrovinsky, L. *et al*, 2010). The setup was installed on beamline ID18 and consists of a SPI laser system (SPI100, wavelength 1064 nm, 100 W) coupled by an optical fiber to a UniHead system, which allows simultaneous visual observation of the sample, laser heating and evaluation of temperature. In order to ensure homogeneous heating of the samples, a laser spot with a diameter of about 50 μm was used. In order to guarantee homogeneous heating we flattened the power profile of the laser beam using a special optical device (π -shaper) mounted on the UniHead.

Samples were heated for at least 10 min at each pressure during continuous laser operation mode. Thermal radiation from the heated sample was collected by an Ocean Optics QE65000 spectrometer, and the resulting spectra were fitted to the Planck radiation function (Bassett & Weathers, 1986), which gave temperatures between 2000 and 2400 K.

5.4.5.V. SMS spectrum fitting

SMS spectra can be fitted using the same approach for conventional energy domain Mössbauer spectra provided the following criteria are met: (a) the source lineshape is implemented as a normalized squared Lorentzian (instead of a normalized Lorentzian):

$$I(E) = \pi\Gamma \left\{ \frac{\Gamma/(2\pi)}{(E - E_0)^2 + (\Gamma/2)^2} \right\} \quad (5.4.6.S.1)$$

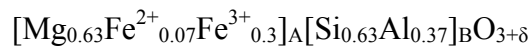
(b) the full transmission integral is used to fit the data due to the high absorption and the lack of non-resonant background; and (c) component areas of doublets and sextets are not fixed to ideal values (i.e., 1:1 for quadrupole doublets and 3:2:1:1:2:3 for magnetic sextets) due to the polarized nature of the synchrotron source and possible existence of texture or preferred orientations in the samples loaded in DACs.

We fit all of the SMS spectra to three quadrupole doublets, one with small centre shift (average value ~ 0.35 mm/s) corresponding to Fe^{3+} , and two with larger centre shift (average value ~ 1 mm/s) corresponding to Fe^{2+} . We applied the conventional constraint of equal widths but allowed the area ratios of component doublets to vary, with all area ratios of doublets within a single spectrum constrained to be the same based on the reasonable assumption that the principal directions of the electric field gradient for both the A and the B sites are the same based on the crystallography of the perovskite structure.

Cation site distribution in the perovskite structure

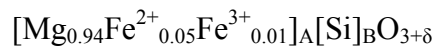
Run S4850 - $(\text{Mg}_{0.63}\text{Fe}_{0.37})(\text{Si}_{0.63}\text{Al}_{0.37})\text{O}_3$ perovskite:

We conducted full structural refinements of a single crystal of silicate perovskite synthesized using identical starting materials and experimental procedure (with the exception that iron was not ^{57}Fe enriched) using *in situ* X-ray diffraction data collected in a DAC at pressures up to 80 GPa and temperatures over 1700 K (Glazyrin *et al.*, 2012). All refinements showed that both Fe^{2+} and Fe^{3+} occupied the A-site exclusively at all conditions studied, indicating the following site distribution:



Run S5083 - ($\text{Mg}_{0.94}\text{Fe}_{0.06}$) SiO_3 perovskite:

We selected a single crystal of silicate perovskite from the same high-pressure synthesis run and conducted a full structural refinement using SHELXL97 software on X-ray diffraction data collected at ambient conditions using an Oxford Diffraction Xcalibur diffractometer. Details of the structural refinement will be published elsewhere. The refinement showed that all iron occupied the A-site exclusively, indicating the following site distribution:



Run S4949 - ($\text{Mg}_{0.78}\text{Fe}_{0.2}\text{Al}_{0.05}$) $\text{Si}_{0.97}\text{O}_3$ perovskite:

From the chemical composition and the $\text{Fe}^{3+}/\Sigma\text{Fe}$ ratio, we determined the following site distribution:



All iron occupies only the A-site.

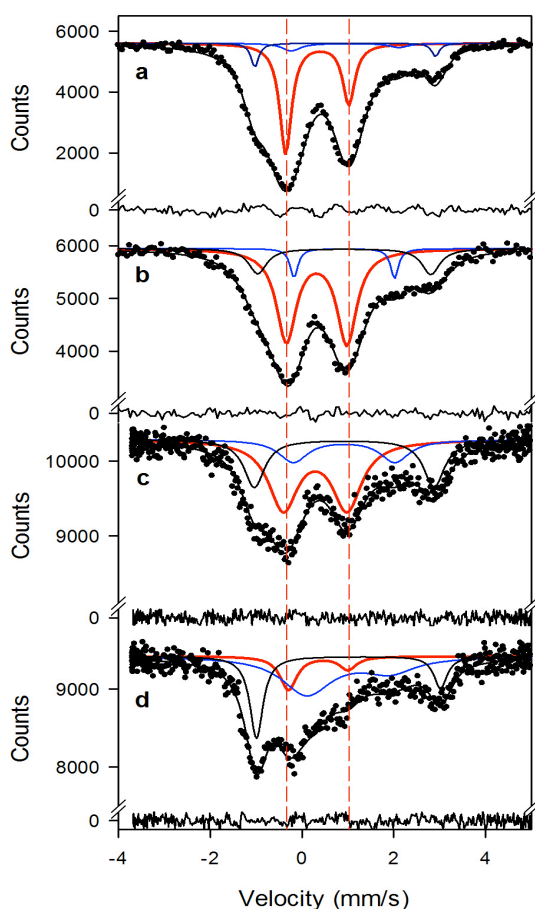


Figure 5.4.6.S4

Room temperature Mössbauer spectra of FeAlPv samples at high pressure: (a) $(\text{Mg}_{0.63}\text{Fe}_{0.37})(\text{Si}_{0.63}\text{Al}_{0.37})\text{O}_3$ perovskite sample #1 at 83 GPa; $(\text{Mg}_{0.63}\text{Fe}_{0.37})(\text{Si}_{0.63}\text{Al}_{0.37})\text{O}_3$ perovskite sample #2 at 78 GPa; $\text{Mg}_{0.78}\text{Fe}_{0.2}\text{Al}_{0.05}\text{Si}_{0.97}\text{O}_{3+\delta}$ perovskite at 75 GPa; $\text{Mg}_{0.94}\text{Fe}_{0.06}\text{SiO}_{3+\delta}$ perovskite at 75 GPa. The spectra were fit to the same model shown in Fig. 5.4.1 (one Fe^{3+} doublet and two Fe^{2+} doublets) with the same colour scheme. Vertical red lines show that the positions of the Fe^{3+} doublets do not change with composition, demonstrating that Fe^{3+} remains in the high-spin state in FeAlPv over a wide composition range.

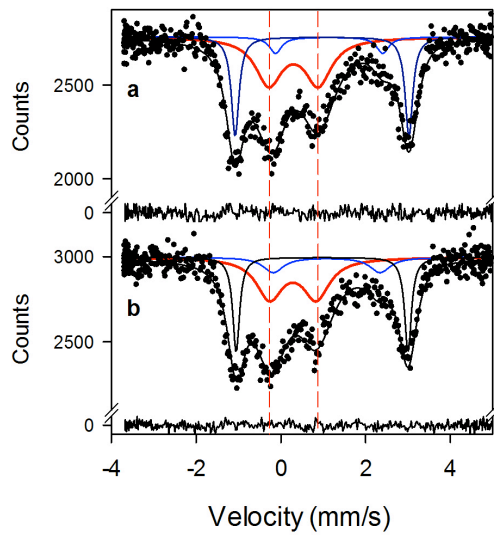


Figure 5.4.6.S5

Room temperature Mössbauer spectra of $\text{Mg}_{0.78}\text{Fe}_{0.2}\text{Al}_{0.05}\text{Si}_{0.97}\text{O}_3$ perovskite at 86 GPa taken (a) before; and (b) after laser heating. Vertical red lines show that the positions of the Fe^{3+} doublets do not change, demonstrating that there is no shift of Fe^{3+} from the A to the B site as a consequence of laser heating, and that Fe^{3+} remains in the high-spin state.

5.5. Portable Double-Sided Laser-Heating System for Energy-Domain Mössbauer Spectroscopy at Synchrotron and Single Crystal Diffraction Experiments with Diamond Anvil Cells

I. Kuppenko^{1,*}, L. Dubrovinsky¹, N. Dubrovinskaia², C. McCammon¹, K. Glazyrin¹, E. Bykova^{1,2}, T. Boffa Ballaran¹, R. Sinmyo¹, A.I. Chumakov³, V. Potapkin^{1,3}, A. Kantor^{1,3}, R. Rüffer³, M. Hanfland³, W. Crichton³, M. Merlini⁴

¹*Bayerisches Geoinstitut, Universität Bayreuth, D-95440 Bayreuth, Germany*

²*Material Physics and Technology at Extreme Conditions, Laboratory of Crystallography, University of Bayreuth, D-95440 Bayreuth, Germany*

³*European Synchrotron Radiation Facility, BP 220, F-38043 Grenoble, France*

⁴*Dipartimento di Scienze della Terra, Università degli Studi di Milano, Via Botticelli 23, 20133 Milano (Italy)*

**-corresponding author*

published in *Review Scientific Instruments* (2012) **83** 124501

5.5.1. Abstract

Diamond anvil cell (DAC) technique coupled with laser heating is a major method to study materials at static multimegabar pressures and at high temperatures. Recent progress in experimental techniques, especially in high-pressure single crystal X-ray diffraction, requires portable laser heating systems, which may heat and move the DAC during data collection. We have developed a double-sided laser heating system for DACs which can be mounted on a ~ 0.1 m² area and has a weight of ~ 12 kg. The system is easily transferable between different in-house or synchrotron facilities and can be assembled and set up during a few hours. The system was successfully tested at the ID09a and ID18 beamlines of the European Synchrotron Radiation Facility (ESRF). We demonstrate application of the system on example of a single crystal X-ray diffraction investigation of $(\text{Mg}_{0.87}\text{Fe}^{3+}_{0.09}\text{Fe}^{2+}_{0.04})(\text{Si}_{0.89}\text{Al}_{0.11})\text{O}_3$ silicate perovskite and energy-domain Mössbauer spectroscopy study of $(\text{Mg}_{0.8}\text{Fe}_{0.2})\text{O}$ ferropericlasite using recently developed Synchrotron Mössbauer Source at high pressures and temperatures.

5.5.2. Introduction

Studies of materials at extreme pressure and temperature conditions are very important for natural sciences such as physics (Lin *et al.*, 2004; Gregoryanz *et al.*,

2005; Dewaele *et al.*, 2008), chemistry and material synthesis (Zerr *et al.*, 2009; Schröder *et al.*, 2011; Palyanov *et al.*, 2011), and especially for geosciences, because they give an opportunity to simulate conditions of the deep Earth's interior (Mikhaylushkin *et al.*, 2007; Kolesnikov *et al.*, 2009; Wu *et al.*, 2009).

The diamond anvil cell technique is a very useful and easy-to-use tool for investigations under high pressure. It was initiated in the late 1950s, and by now has become the most successful method of pressure generation in a multi megabar pressure range (Eremets, 1996; Dubrovinskaia *et al.*, 2010). The laser heating in DACs was first introduced by Ming and Bassett (Ming & Bassett, 1974) and is well described in the literature (Boehler, 2000). There are numerous facilities, including specialized beamlines at the third-generation synchrotrons (Shen *et al.*, 2001; Schultz *et al.*, 2005; Hirose, 2006; Prakapenka *et al.*, 2008), where the DAC laser-heating technique is coupled with different analytical methods for *in situ* investigations such as the Raman spectroscopy or X-ray diffraction (Boehler *et al.*, 2008; Santoro *et al.*, 2005). However, until recent times all these laser-heating systems were linked to certain equipment or to a beamline.

Modern scientific challenges demand higher flexibility in capabilities of research techniques including laser heating in DACs. As a result, since 2009 portable DAC laser-heating systems that can be easily moved between different analytical facilities, including transfer from in-house to a synchrotron or between synchrotron beamlines, began to emerge (Boehler *et al.*, 2009; Dubrovinsky *et al.*, 2009). Still there was no a portable double-sided laser-heating system that would meet all scientific needs. The system described by Boehler *et al.*, (2009) allows double-sided laser heating but requires a rather large space (0.4 m²) for the support. It has never been tested for applications in single crystal studies. Moreover, the design of this system (Boehler *et al.*, 2009) has a drawback – simultaneous temperature and X-ray measurements are not possible because optical components for collecting thermal radiation block and/or shadow the X-ray primary beam or the scattered signal. The system described by Dubrovinsky *et al.*, (2009) was successfully used in routine *in house* experiments (Gu *et al.*, 2011; Parakhonskiy *et al.*, 2011), the *in situ* synchrotron X-ray absorption and diffraction investigations (Narygina *et al.*, 2011), and (with some modifications) in synchrotron single-crystal X-ray diffraction experiments

(Dubrovinsky *et al.*, 2010). Its main disadvantage was one-sided laser-heating and, thus, limited applications for only optically thin samples.

Here we report the development of a double-sided laser heating system for single-crystal diffraction studies and other experiments, which require movement of the DAC during a data collection. The new system provides with a more homogeneous temperature distribution within the sample (*e.g.* it allows higher temperatures without possible destructions due to thermal stresses), and permits the use of thicker samples (thus providing an opportunity to use the system in work with materials which are difficult to heat).

5.5.3. Design of the laser-heating system

The system consists of two major components – the sources of laser light and two universal laser-heating heads (UniHeads) (Fig. 5.5.1). The UniHeads are based on the finite cutting laser head (Precitec KG) and their functions in the portable laser system are to focus incoming laser beams on the sample within the DAC, to provide with a high magnification imaging of the sample in the DAC with coaxial illumination, and to give access for the multiwavelength spectroradiometry for temperature measurements (Shen *et al.*, 2010).

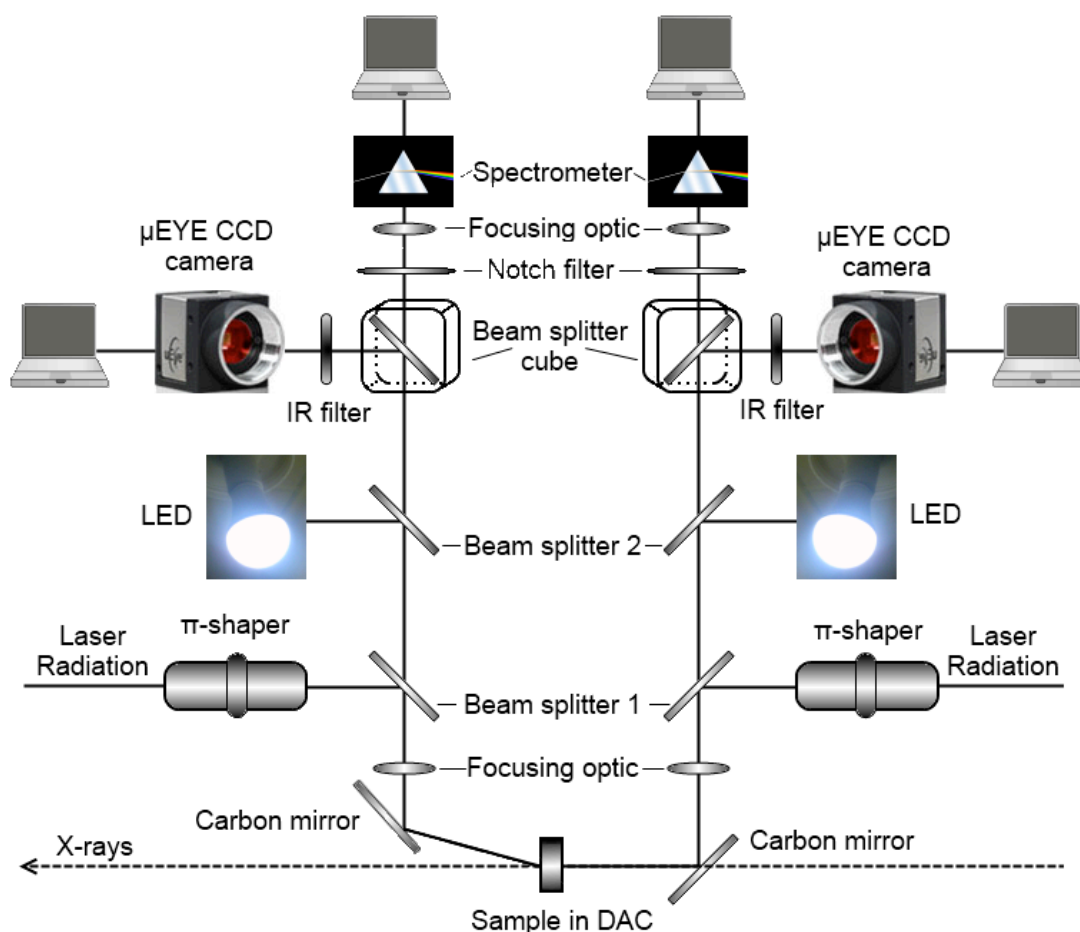


Fig 5.5.1
Schematic diagram of the optical components of UniHeads.

5.5.3.1. Laser

As a laser source we have used two SPI100 modulated fiber lasers with maximum output power of 100 W. The weight of the both lasers is 40 kg and the excitation wavelength is 1071 nm. An additionally integrated red laser source serves as an aid to initial beam targeting. The output of the SPI lasers has a Gaussian power distribution with a diameter of ~ 3 mm at $1/e^2$. The output power level can be monitored and controlled by an external analog interface. The fiber lasers can be operated in a continuous or pulse mode with the frequency up to 100 kHz and minimum time of the pulses of less than 10 μ s. The lasers require no water-cooling and use only a standard electrical plug.

5.5.3.2. Focusing optics and beam targeting

The output 1071 nm laser light is collected by a π -shaper (MolTech GmbH), 90° bended using a specially coated beam splitter (Beam Splitter 1 in Fig. 5.5.1: the reflectivity above 1050 nm is >99.99%, it is transparent in the 400-900 nm wavelength range), and focused by the UniHead set of lenses with an 80-mm working distance. The original 3 mm in diameter laser beam with the Gaussian intensity distribution is converted into a flat top beam with up to ~50 μm FWHM (Prakapenka *et al.*, 2008).

In order to direct the laser beam to the sample and make it coaxial with the incident X-ray beam, we employ carbon mirrors mounted at approximately 45° angle to the UniHeads' axis (Fig. 5.5.1, 2). The carbon mirrors are made out of polished glassy carbon plates of 1 or 2 mm thickness. They are coated at the optical facility Lab of the University of Bayreuth by a 100 nm thick silver film and, on top of the silver layer, by a 5 nm thick silica film. In case of experiments using the X-ray diffraction, the carbon mirror of the downstream UniHead is mounded under an angle which is slightly below 45° (usually about 41-42 °) so that and the mirror appears outside of the path of the direct X-ray beam. Thus, we avoid the undesirable diffraction of X-ray on the carbon mirror. The X-ray scattering from glassy carbon of the upstream mirror is blocked by the DAC's body.

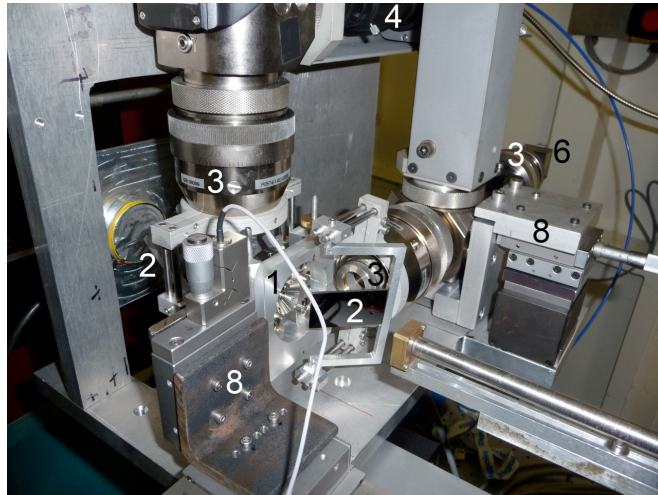
5.5.3.3. Illumination, observation and the spectroradiometry module

The illumination of the sample is realized due to the built-in LED in the UniHead (Fig. 5.5.1). The LED is controlled by an external power supply. For observation of the sample in the DAC the high-resolution $\mu\text{EYE}^{\text{TM}}$ CCD cameras are used. To prevent oversaturation of the cameras by the reflected laser light, KG3 IR filters (SCHOTT GmbH) are exploited. The software of the camera allows enlarging a part of the observed area and tracing a certain position in the image. The UniHead equipped with a modified optical output module for temperature measurements consists of a $\mu\text{EYE}^{\text{TM}}$ CCD camera, a focusing lens projecting a central part (of about 10 μm in diameter) of the image of the heated spot onto the end of the optical fiber, and a beam-splitter cube (50/50, Edmund Scientific Inc) (Pippinger *et al.*, 2011). The

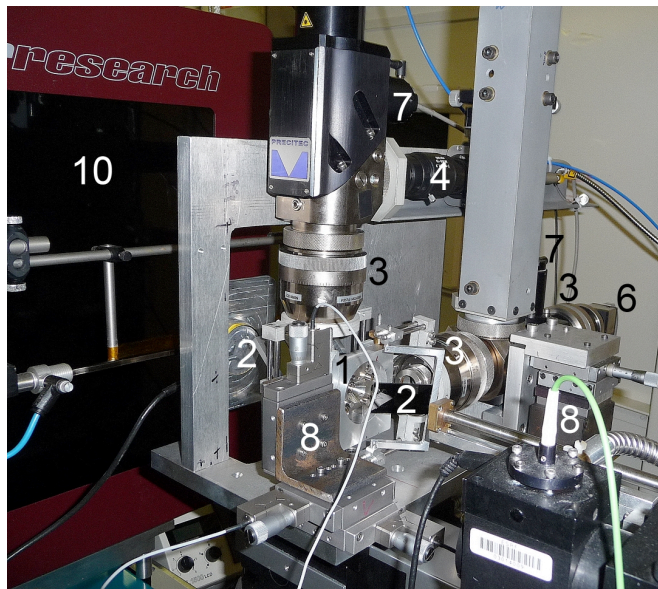
beam-splitter cube is movable and can be fixed in two positions. If it is fixed outside of the optical path, then all the light radiated by the heated spot transmits into the optical fiber. The cube position within the optical path allows 50% of the light to be transferred to the CCD camera for visual observations. In our experiments we used an Ocean Optics QE65000 spectrometer or Acton SP2300 spectrometer (Princeton Instruments) with the PIXIS400 CCD detector. To prevent the incidence of the laser light onto the detector, 1064 nm notch filters (Edmund Optics Inc.) are used. The temperature measurements are performed by the spectroradiometry method (Shen *et al.*, 2010) i.e. by fitting thermal radiation signals in a given wavelength (usually 600 to 850 nm) range to the Planck radiation function. The software developed by A. Kantor and I. Kantor allows on-line monitoring of the temperature. The system response spectra are calibrated by melting of platinum (Pippinger *et al.*, 2011).

5.5.3.4. System alignment

All parts, the UniHeads, a 3D stage for a DAC holder, and the holder with the DAC are mounted on a common aluminum plate (0.35x0.30 m²; the thickness of 0.15 m). In the experiments described below the upstream UniHead was set up horizontally and the downstream UniHead was set up vertically (Fig. 5.5.2). The downstream UniHead is mounted rigidly on the plate and has no degrees of freedom. The sample in the DAC should be aligned with respect to this UniHead using the three-dimensional stage. The red alignment laser of the SPI100 can be used to simplify the process. The upstream UniHead is mounted on its own three dimensional stage and should be aligned to the sample within the DAC afterwards. Focusing of the laser beams on the sample is proceeded due to adjustable lenses of the π -shapers (Prakapenka *et al.*, 2008). The last part of the procedure is the alignment of the spectrometers. For this purpose the end of the optical fiber coming to the spectrometer is connected to the visible (in our experiments 532 nm) diode laser whose spot is focused on the sample. By means of the adjustable screws (Fig. 5.5.2c) of the spectroscopic module the spot is placed exactly at the position of the center of the heated area. According to our experience, the mounting of the system and its alignment requires two to three hours.



a)



b)



Fig. 5.5.2

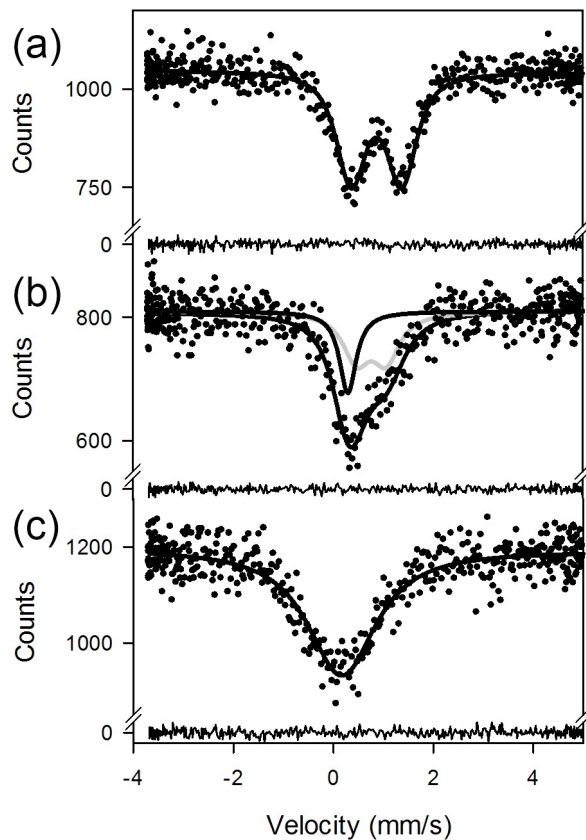
The double-side portable laser-heating system mounted for experiments at ID09a (a,b) and ID18 beam lines at ESRF (c). 1, holder with DAC; 2, carbon mirrors; 3, focusing optics; 4, π -shaper; 5, beam-splitter cube; 6, CCD camera; 7, LED; 8, three dimensional stages; 9, adjustable screws for spectrometer focusing; 10, MAR555 detector.

5.5.4. Examples of application of the portable laser-heating system

5.5.4.1. Mössbauer spectroscopy investigation of $(\text{Mg}_{0.8}\text{Fe}_{0.2})\text{O}$

Hyperfine parameters determined from Mössbauer spectra strongly depend on pressure and temperature. Thus the energy domain ^{57}Fe Mössbauer spectroscopy is not only one of the best methods to study iron's valence and spin state at high pressure, but the probe of choice to test temperature homogeneity in laser-heated DACs. However, conventional energy-resolved Mössbauer spectroscopy utilizes radioactive sources with low brilliance. Therefore high-pressure Mössbauer studies

require too long collection time to be effectively applied for investigations in a laser-heated DAC. Recently developing of a Synchrotron Mössbauer Source (SMS) at the Nuclear Resonance beamline (ID 18) (Chapter 5.2) solved this problem. The SMS allows one to perform energy-domain Mössbauer measurements using synchrotron as a source of gamma radiation. In contrast to radioactive sources, the beam emitted by the SMS is nearly fully resonant, has high brilliance and can be focused to a $10 \times 5 \mu\text{m}^2$ spot size. That opens a possibility for fast and robust measurements in DACs at high pressures and, if coupled with laser heating, at high temperatures. In order to test the double-sided laser heating system with the SMS we selected $(\text{Mg}_{0.8}\text{Fe}_{0.2})\text{O}$ (ferropericlase, Fp20), since its Mössbauer spectra at high pressure and temperature are already known from our previous work using an externally heated diamond anvil cell and a conventional in-house Mössbauer source (Kantor *et al.*, 2009). Pellets of Fp20 of 30 to 40 μm in diameter with the thickness of about 15 μm were loaded along with a Ne medium (Kurnosov *et al.*, 2008) into a pressure chamber (the initial diameter of 100 μm and the height of about 30 μm) made in a Re gasket. The sample was compressed using a symmetric piston-cylinder type DAC produced at BGI. All measurements were carried out at ID 18 using the SMS, and each spectrum took roughly 10 minutes to collect. The Mössbauer spectrum of the high-spin phase ($P < 50$ GPa) consists of a single quadrupole doublet arising from octahedrally coordinated Fe^{2+} (Fig. 5.5.3a) (Kantor *et al.*, 2006). Upon laser heating from only one side (or during double-sided heating when the X-ray beam and the laser spot are not well aligned), the spectrum becomes asymmetric (Fig. 5.5.3b). Since we know from previous experiments on $(\text{Mg}_{0.8}\text{Fe}_{0.2})\text{O}$ that temperature causes a decrease in quadrupole splitting, we interpret the spectrum in Fig. 5.5.3b as indicating a temperature gradient in the sample between the relatively cold material (grey doublet) and a hotter region (black singlet), corresponding to temperatures of 450 K and 1000 K, respectively. During double-sided heating with the correct alignment of the X-ray beam and laser spot, the Mössbauer spectrum becomes more symmetric (Fig. 5.5.3c) at the temperature of 1300 K. We found that temperature gradients also arise from the double-sided laser heating of thick samples (above about 20 μm), where the interior of the sample remains colder than the surface.

**Fig. 5.5.3**

Synchrotron Mössbauer source spectra of $\text{Fe}_{0.2}\text{Mg}_{0.8}\text{O}$ at 29 GPa: (a) room temperature; (b) laser heating with misaligned beam; (c) double-sided laser heating with good alignment. The temperatures determined from the centre shift are 450 K (grey doublet in (b)) and 1000 K (black singlet in (b)) and 1300 K (singlet in (c)). The fit residuals are shown below each spectrum.

5.5.4.2. X-ray single crystal diffraction of Fe,Al rich silicate perovskite in double-side laser heated DAC

Iron and aluminum bearing magnesium silicate perovskite $(\text{Mg,Fe,Si,Al})\text{O}_3$ is likely to be the main component of the Earth lower mantle. Iron and aluminum could significantly affect properties of silicate perovskite, especially due to electronic transitions in Fe^{2+} and Fe^{3+} . Recent single crystal diffraction studies (Dubrovinsky *et al.*, 2010; Boffa-Ballaran *et al.*, 2012) reveal that ferrous and ferric silicate perovskites do not demonstrate any sign of irregular changes in the behavior of the molar volume, lattice parameters, the mean bond distances of the $(\text{Si,Al})\text{O}_6$ octahedra and $(\text{Mg,Fe})\text{O}_8$ -polyhedra which could be related to the high-spin – low-spin (HS-LS) crossover. However, there is one hypothesis which has never been tested before based on single crystal X-ray diffraction data: according to Catalli *et al.*, (2010) high

Crystal Diffraction Experiments with DACs

temperatures at pressures above ~ 40 GPa can promote the reaction $\text{Fe}^{3+(\text{HS})}_{\text{A}} + \text{Al}^{3+}_{\text{B}} \rightarrow \text{Fe}^{3+(\text{LS})}_{\text{B}} + \text{Al}^{3+}_{\text{A}}$ (indices “A” and “B” denote corresponding positions in the silicate perovskite structure). In order to check if such a process is indeed possible we employed the portable double-sided laser heating system at ID09a beam line at ESRF.

Diffraction data were collected using the MAR555 Flatpanel detector, radiation with a wavelength of 0.4149 \AA , the beam size of $10 \times 10 \text{ \mu m}^2$, and the crystal-to-detector distance of about 399 mm. 96 frames in the omega scanning range of $-28 - +20$ degrees were collected (0.5 deg scanning step size) with the exposure time of 1 sec. At each pressure-temperature point data were collected at two different positions of the DAC different by 90° along the compression direction, and the data-sets were merged. The data were processed using the CrysAlis software (Oxford Diffraction (2006) CrysAlis RED, version 1.171.31.8. Oxford Diffraction Ltd., Abingdon, Oxfordshire). Crystal structure refinements on integrated intensities were carried out with the SHELXL-97 WinGX version (Farrugia, 1999; Sheldrick, 2008). Single crystals of $(\text{Mg}_{0.87}, \text{Fe}^{3+}_{0.09}, \text{Fe}^{2+}_{0.04})(\text{Si}_{0.89}, \text{Al}_{0.11})\text{O}_3$ silicate perovskite were synthesized in a multi-anvil apparatus (Dubrovinsky *et al.*, 2010) (the crystal chemical formula based on results of microprobe analysis and Mössbauer spectroscopy). A sample with dimensions of $\sim 0.15 \times 0.10 \times 0.10 \text{ mm}^3$ was loaded along with a Ne medium (Kurnosov *et al.*, 2008) into a pressure chamber made in a Re gasket (initial height of about 30 \mu m and the diameter of 125 \mu m) and compressed using a symmetric piston-cylinder type DAC equipped with the ALMAX type diamonds (80° opening and 250 \mu m culets).

We collected the diffraction data at pressures of 65 GPa to 78 GPa (determined from the Ne thermal equation of state (Fei *et al.*, 2007)) in several sets, namely before, during and after laser heating at 1750(50) K (Table 5.5.1). For each P , T data point we obtained between 105 and 125 unique reflections. Apart from atomic coordinates and isotropic thermal parameters, we refined the occupancy of the B-site by Si and Fe (Si and Al are not distinguishable), and that of the A-site by Mg and Fe (Table 5.5.1). Structural refinements on the integrated intensities converged with values of the R-factors below 5%. We found that (a) the refined amount of iron in the A-site coincides, within uncertainty, with the value determined by microprobe data, (b) laser heating does not affect chemical composition of the silicate perovskite in our

experiments, and (c) high temperature does not promote any exchange chemical reactions between the A- and B-sites (i.e. there is no any sign of Fe entering the B-site during heating). Note that previously reported by us the single-side laser-heating system (Dubrovinsky *et al.*, 2010) allowed collecting less than 70 reflections per run and it precluded the refinement of the sites' occupancy.

Table 5.5.1. Results of the single crystal structural refinement of $(\text{Mg}_{0.87}, \text{Fe}^{3+}_{0.09}, \text{Fe}^{2+}_{0.04})(\text{Si}_{0.89}, \text{Al}_{0.11})\text{O}_3$ silicate perovskite (space group *Pbnm*) at different pressures and temperatures.

P, GPa	T, K	R1, %	Lattice parameters		Atomic parameters
			$a, \text{\AA}$ $b, \text{\AA}$ $c, \text{\AA}$	V $\text{\AA}^3/\text{unit cell}$	$xyzU$ $\text{Si}_B, \text{Fe}_B, \text{Mg}_A, \text{Fe}_A^*$
65.9(5)	298	3.2	4.4875(3) 4.7138(3) 6.4826(23)	137.13(15)	A -0.0183(5) 0.4334(7) 0.25 0.030(1) B 0 0 0 0.025(1) O1 0.1131(14) 0.0326(12) 0.25 0.034(2) O2 0.1832(8) 0.3080(9) -0.0616(14) 0.031(2) 1.01(1) 0.00(1) 0.88(2) 0.12(1)
78(1)	1750(50)	4.4	4.4733(6) 4.7101(5) 6.4874(45)	136.69(20)	A -0.0167(3) 0.4305(5) 0.25 0.026(1) B 0 0 0 0.023(1) O1 0.1183(8) 0.0313(8) 0.25 0.027(1) O2 0.1868(6) 0.3051(6) -0.0603(7) 0.027(1) 1.01(1) 0.00(1) 0.87(2) 0.128(16)
63.2(3)	298	3.7	4.4975(5) 4.7270(4) 6.4996(7)	138.18(11)	A -0.0178(4) 0.4305(5) 0.25 0.016(1) B 0 0 0 0.014(1) O1 0.1135(11) 0.0346(8) 0.25 0.019(1) O2 0.1873(6) 0.3063(7) -0.0578(8) 0.017(2) 1.00(1) 0.00(1) 0.88(2) 0.12(1)

The “ $\text{Si}_B, \text{Fe}_B, \text{Mg}_A, \text{Fe}_A^$ ” means the occupancy of the A- or B-site by a corresponding atom.

5.5.5. Conclusions

We have developed portable laser-heating system that allows homogeneous double-sided heating with *in situ* observations and temperature measurements. The system is easily mounted on various scientific facilities, including synchrotron beamlines. All major components of the system are commercially available that

makes its duplication to be a straightforward task. The ready-to-use system can be assembled and aligned even by a user with a very basic training. The system has been successfully tested for the single crystal X-ray diffraction and the SMS investigations at ESRF.

5.6 Full List of Publications (With a Papers Not Included Into the Thesis)

- [1] I. Kuppenko, L. Dubrovinsky, N. Dubrovinskaia, C. McCammon, K. Glazyrin, E. Bykova, T. Boffa Ballaran, R. Sinmyo, A.I. Chumakov, V. Potapkin, A. Kantor, R. Ruffer, M. Hanfland, W. Crichton, M. Merlini. Portable Double-Sided Laser-Heating System for Mössbauer Spectroscopy and X-ray Diffraction Experiments at Synchrotron Facilities with Diamond Anvil Cells; accepted for publication, *Rev. Sci. Instrum.*
- [2] V. Potapkin, A.I. Chumakov, G.V. Smirnov, R. Ruffer, C. McCammon, and L. Dubrovinsky. Angular, spectral and temporal properties of nuclear radiation ^{57}Fe Synchrotron Mössbauer source. *Phys. Rev. A* (2012) **86** 053808
- [3] V. Potapkin, C. McCammon, L. Dubrovinsky, K. Glazyrin, A. Kantor, I. Kuppenko, C. Prescher, R. Sinmyo, G. Smirnov, A. Chumakov and R. Ruffer, Spin state of iron in lower mantle; accepted for publication, *Nature Communications*.
- [4] V. Potapkin, A.I. Chumakov, G.V. Smirnov, J.-P. Cells, R. Ruffer, C. McCammon and L. Dubrovinsky. The ^{57}Fe Synchrotron Mössbauer source at the ESRF; *Journal of Synchrotron Radiation* (2012) **19** 559-569
- [5] G.V. Smirnov, A.I. Chumakov, V.B. Potapkin, R. Ruffer, and S.L. Popov; Multispace quantum interference in ^{57}Fe Synchrotron Mössbauer source; *Phys. Rev. A* **84** (2011) 053851
- [6] V. Potapkin, A.I. Chumakov, G.V. Smirnov, S.L. Popov, R. Ruffer, L. Dubrovinsky and C. McCammon. Synchrotron Mössbauer source for geophysical studies at the ESRF. *Acta Cryst.* (2010). **A66**, s172-s173.
- [7] V. Potapkin, A.V. Zabolotskii and A.A. Novakova. Formation of an encapsulated Fe_2O_3 nanostructure during mechano-chemical interaction of iron oxide and excess alumina; *Journal of Surface Investigation X-ray, Synchrotron and Neutron techniques* **5** (2009) 786-790
- [8] T.Yu. Kisileva, T.F. Grigor'eva, D.V. Gostev, V.B. Potapkin, A.N. Falkova, and A.A. Novakova; Structure investigation of Fe-Al nanomaterial obtained by mechano-activation and self-propagating high-temperature synthesis; *Moscow University Physics Bulletin* **63** (2008) 55-60.
- [9] A.A. Novakova, T.Yu. Kiseleva, A.N. Falkova, V.B. Potapkin, T.F. Grigorieva, A.P. Barinova and N.Z. Lyakhov; Mechanoactivated interaction of hematite and gallium; *Proceedings of 14th International Symposium on Metastable and Nano-Materials ISMANAM-2007* **26–30** (2007) p. 179.

6. Bibliography

- Agnor C.B., Canup R.M., and Levison H.F. (1999) On the character and consequences of large impacts in the late stage of terrestrial planets formation. *Icarus* **142**, 219-237.
- Afnas'ev A.M. and Y. Kagan (1965) Suppression of Inelastic Channels in Resonant Nuclear Scattering in Crystals, *JETP*, **21**, 215-216.
- Allegre, C. J., J.-P. Poirier, E. Humler, and A. W. Hofmann (1995), The chemical composition of the Earth, *Earth and Planetary Science Letters*, **134**, 515-526.
- Badro J., Fiquet G., Guyot F., Rueff J.-P., Struzhkin V.V., Vankó G., and Monaco G. (2003) Partitioning in Earth's mantle: toward a deep lower mantle discontinuity. *Science* **300**, 789-791.
- Badro J., Rueff J.-P., Vankó G., Monaco G., Fiquet G., and Guyot F. (2004) Electronic transitions in perovskite: Possible non-convecting layers in the lower mantle. *Science* **305**, 383-386.
- Bassett, W., and M. Weathers (1986, Temperature measurement in laser heated diamond anvil cells, *Physica B+C*, **139-140**, 900-902.
- Belyakov V.A. and Y.M. Ayvazian (1968) Direct determination of the structure formed by crystal magnetic field at nuclei of Mossbauer isotopes. *JETP*, **7**, 368-369.
- Belyakov V.A. and Y.M. Ayvazian (1969) Quadrupole diffraction maxima in Mossbauer spectra. *JETP*, **9**, 393-394.
- Bina C.R. (2003) Seismological constraints upon mantle composition. pp. 39-59. In *The Mantle and Core* (ed. R.W. Carlson) Vol. 2 Treatise on Geochemistry (eds. Holland H.D. and Turekian K.K.), Elsevier-Pergamon, Oxford.
- Borovik-Romanov A.S. and V. I. Ozhogin (1960) Weak ferromagnetism in antiferromagnetic single crystal of CoCO_3 . *JETP*, **16**, 1443-1444.
- Boehler, R. (2000) High-pressure experiments and the phase diagram of lower mantle and core materials. *Reviews of Geophysics*, **38**, 221.
- Boehler, R., Santamaría-Pérez, D., Errandonea, D. & Mezouar, M. Melting (2008) Density, and anisotropy of iron at core conditions: new x-ray measurements to 150 GPa. *Journal of Physics: Conference Series*, **121**, 022018.
- Bouvier, A., and M. Wadhwa (2010) The age of the Solar System redefined by the oldest Pb–Pb age of a meteoritic inclusion, *Nature Geoscience*, **3**, 637-641.
- Boffa-Ballaran, T., A. Kurnosova, K. Glazyrina, D.J. Frost, M. Merlini, M. Hanfland, R. Caracas (2012) Effect of chemistry on the compressibility of silicate perovskite in the lower mantle. *Earth and Planetary Science Letters*, **333–334**, 181–190.

- Brand R.A. (1990) NORMOS programs, version 1990. The NORMOS program is available from Wissel GmbH, D-82319 Starnberg, Germany.
- Brodholt, J. P. Pressure-induced changes in the compression mechanism of aluminous perovskite in the Earth's mantle. *Nature*, **407**, 620-622 (2000).
- Burns R.G. (1993) Mineralogical applications of crystal field theory. 2nd edition. Cambridge University Press.
- Catalli, K., S.-H. Shim, V. Prakapenka, J. Zhao, W. Sturhahn, P. Chow, Y. Xiao, H. Liu, H. Cynn, and W. J. Evans (2010) Spin state of ferric iron in MgSiO₃ perovskite and its effect on elastic properties, *Earth and Planetary Science Letters*, **289**, 68-75.
- Catalli, K. *et al.* (2011) Effects of the Fe³⁺ spin transition on the properties of aluminous perovskite - New insights for lower-mantle seismic heterogeneities. *Earth Planet. Sci. Lett.* **310**, 293-302.
- Chambers J.E. (2003) Planet formation, pp. 461-475. In *Meteorites, Comets and Planets* (ed. Davis A.M.) Vol. 1 Treatise on Geochemistry (eds. Holland H.D. and Turekian K.K.), Elsevier-Pergamon, Oxford.
- Chumakov A.I., M. V. Zelepukhin, G. V. Smirnov, U. van Bürck, R. Rüffer, R. Hollatz, H. D. Rüter, and E. Gerdau (1990) Time spectra of a nearly-single-line pure nuclear reflection excited by synchrotron radiation. *Phys. Rev. B*, **41**, 9545-9547.
- Chervin, J. C., B. Canny, J. M. Besson, and P. Pruzan (1995) A diamond anvil cell for IR microspectroscopy, *Rev. Sci. Instrum.*, **66**, 2595.
- Cohen R.E. and Mukherjee S. (2004) Non-collinear magnetism in iron at high pressures. *Phys. Earth Planet. Int.*, **143-144**, 445-453.
- Dewaele, A., Datchi, F., Loubeyre, P. & Mezouar, M. (2008) High pressure-high temperature equations of state of neon and diamond. *Physical Review B*, **77**, 094106.
- Dubrovinsky L., K. Glazyrin, C. McCammon, O. Narygina, E. Greenberg, S. Übelhack, A. I. Chumakov, S. Pascarelli, V. Prakapenka, J. Bock and N. Dubrovinskaia (2009) Portable laser-heating system for diamond anvil cells. *Journal of Synchrotron Radiation*, **16**, 737-741.
- Dubrovinsky L., T. Boffa-Ballaran, K. Glazyrin, A. Kurnosov, D. Frost, M. Merlini, M. Hanfland, V. B. Prakapenka, P. Schouwink, T. Pippinger & N. Dubrovinskaia (2010) Single-crystal X-ray diffraction at megabar pressures and temperatures of thousands of degrees. *High Pressure Research*, **30**, 620-633.
- Dubrovinskaia, N., Dubrovinsky, L., Caracas, R. & Hanfland, M. (2010) Diamond as a high pressure gauge up to 2.7 Mbar. *Applied Physics Letters* **97**, 251903.
- Dziewonski A.M and Anderson D.L (1981) Preliminary Reference Earth Model. *Phys. Earth Planet. Int.* **25**, 297 – 356.

- Eremets, M.I. (1996) *High Pressure Experimental Methods*. 408 (Oxford Science: Oxford, 1996)
- Farrugia, L.J. (1999) WinGX suite for small-molecule single-crystal crystallography. *Journal of Applied Crystallography*, **32**, 837-838.
- Fei, Y., A. Ricolleau, M. Frank, K. Mibe, G. Shen, and V. Prakapenka (2007), High-Pressure Geoscience Special Feature: Toward an internally consistent pressure scale. *Proceedings of the National Academy of Sciences*, **104**, 9182-9186.
- Forman, R. A., G. J. Piermarini, J. D. Barnett, and S. Block (1972), Pressure Measurement Made by the Utilization of Ruby Sharp-Line Luminescence. *Science*, **176**, 284-285
- Frost D.J., Liebske C., Langenhorst F., McCammon C.A., Trønnes G.R, and Rubie D.C. (2004) Experimental evidence for the existence of iron-rich metal in the Earth's lower mantle. *Nature* **428**, 409-412
- Frost, D.J. (2008) The Upper Mantle and Transition Zone. *Elem. Mag.* **4**, 171-176
- Fujino, K. D. Nishio-Hamane, Y. Seto, N. Sata, T. Nagai, T. Shinmei, T. Irifune, H. Ishii, N. Hiraoka, F. Q. Cai, K.-D. (2012) Tsuei. Spin transition of ferric iron in Al-bearing Mg-perovskite up to 200 GPa and its implication for the lower mantle. *Earth Planet. Sci. Lett.*, **317-318**, 407-412 .
- Fyfe, W.S. (1960) The possibility of d-electron coupling in olivine at high pressures. *Geochim. Cosmochim. Acta*, **19**, 141-143
- Garg, A. B., V. Vijayakumar, and B. K. Godwal (2004) Electrical resistance measurements in a diamond anvil cell to 40 GPa on ytterbium. *Rev. Sci. Instrum.*, **75**, 2475-2578.
- Gaffney E.S. and Anderson D.L. (1973) Effect of low-spin Fe²⁺ on the composition of the lower mantle. *J. Geophys. Res.* **78**, 7005-7014
- Gerdau E., Ruffer R., Winkler H., Tolksdorf W., Klages C. P., and Hannon J. P. (1985) Nuclear Bragg diffraction of synchrotron radiation in yttrium iron garnet. *Phys. Rev. Lett.*, **54** , 835-838.
- Glazyrin, K. (2011) Effect of iron oxidation state on the bulk sound velocity of the lower mantle. *Dissertation*. <http://opus.ub.uni-bayreuth.de/volltexte/2011/944/>.
- Glazyrin, K. *et al.* (2012) Iron in oxides, silicates and alloys under extreme pressure-temperature conditions. *Nature Communication* (submitted).
- Goldreich P. and Ward W.R. (1973) The formation of planetesimals. *Astrophys. J.*, **183**, 1051-1062
- Goncharov A.F., Struzhkin V.V., Jacobsen S.D. (2006) Reduced radiative conductivity of low spin (Mg,Fe)O in the lower mantle. *Science*, **312**, 1205-1208

- Goodman J. and Pindor B. (1999) Secular instability and planetesimal formation in the dust layer. *Icarus*, **148**, 537-549
- Greenwood N.N. and Gibb T.C. (1971) Mossbauer Spectroscopy, pp. 314–315, and the references therein, Chapman and Hall, London
- Gregoryanz, E., Degtyareva, O., Somayazulu, M., Hemley, R. & Mao, H.-kwang (2005) Melting of Dense Sodium. *Phys. Rev. Lett.*, **94**, 185502.
- Gu, T., Wu, X., Qin, S. & Dubrovinsky, L. (2011) In situ high-pressure study of FeP: Implications for planetary cores. *Physics of the Earth and Planetary Interiors*, **184**, 154-159.
- Gütlich P., Bill E., Trautwein A. X., (2011) *Mössbauer Spectroscopy and Transition Metal Chemistr*, Springer.
- Haas M., (2007) Polariton effects at propagation of synchrotron radiation in Mössbauer media. *Phys. Lett. A*, **361** , 391-395.
- Haase, J., Goh S. K., Meissner T., Alireza P. L., and Rybicki D. (2009), High sensitivity nuclear magnetic resonance probe for anvil cell pressure experiments. *Rev. Sci. Instrum.*, 80, 073905.
- Hart, S., and Zindler A. (1986) In search of a bulk-Earth composition. *Chemical Geology*, **57**, 247-267.
- Hannon J.P. and Trammell G.T. (1999) Coherent γ -ray optics. *Hyperfine. Interact.*, **123/124** , 127-274.
- Hedlin M.A.H., Shearer P.M., and Earle P.S. (1997) Seismic evidence for small-scale heterogeneity throughout the Earth's mantle. *Nature* **387**, 145-150
- Hignette, O., Peffen, J.-C., Alvaro, V., Chinchio, E., & Freund, A.K., (2001) *SPIE Conference Proceedings* **45**, 4501-4510.
- Hirose, K. (2006) Postperovskite phase transition and its geophysical implications. *Reviews of Geophysics*, **44**, RG3001.
- Horiuchi H., Ito E., and Weidner D.J. (1987) Perovskite-type MgSiO₃: single-crystal X-ray diffraction study. *Am. Mineral.* **72**, 357-360
- Hsu, H., Umemoto, K., Blaha, P. & Wentzcovitch, R. M. (2010) Spin states and hyperfine interactions of iron in (Mg,Fe)SiO₃ perovskite under pressure. *Earth Planet. Sci. Lett.* **294**, 19-26.
- Hsu, H., Blaha, P., Cococcioni, M. & Wentzcovitch, R. M. (2011) Spin-state crossover and hyperfine interactions of ferric iron in MgSiO₃ perovskite. *Phys Rev Lett*, **106**, 118501.
- Huggins F. (1975) The 3d levels of ferrous iron in silicate garnets. *Am. Mineral.*, **60**, 316-319.

- Ingalls R. (1964) Electric-field gradient tensor in ferrous compounds. *Phys. Rev.* **133A**, 787- 795.
- Irifune T. and Ringwood A.E. (1987) Phase transformations in primitive MORB and pyroxene compositions to 25 GPa and some geophysical implications, pp. 221-230. In *High-pressure research in mineral physics* (eds. Manghnani M. and Syono Y.) Terra/American Geophysical Union, Tokyo/Washington.
- Jackson, I., and S. M. Ridgen (2000), *Composition and Temperature of the Earth's Mantle: Seismological Models Interpreted through Experimental Studies of Earth Materials* in "The Earth's mantle : composition, structure, and evolution," 1st ed., edited by I. Jackson, Cambridge University Press, Cambridge, UK.
- Jackson J.M., Sturhahn W., Shen G., Zhao J., Hu M.Y., Errandonea D., Bass J.D. and Fei Y. (2005) A synchrotron Mössbauer spectroscopy study of (Mg,Fe)SiO₃ perovskite up to 120 GPa. *Am. Mineral.*, **90**, 199-205.
- Jagoutz, E., H. Palme, H. Baddenhausen, K. Blum, M. Cendales, G. Dreibus, B. Spettel, V. Lorenz, and H. Wanke (1979), *The abundances of major, minor and trace elements in the earth's mantle as derived from primitive ultramafic nodules in "Proceedings of the Tenth Lunar and Planetary Science Conference, Houston, Texas, March 19-23, 1979,"* Pergamon Press, New York.
- Jones, J. H., and M. J. Drake (1986). Geochemical constraints on core formation in the Earth. *Nature*, **322**, 221-228
- Kagan Y., A. M. Afanas'ev, and V. G. Kohn. (1979) On excitation of isomeric nuclear states in a crystal by synchrotron radiation. *J. Phys. C Solid State Phys.*, **12**, 615-631.
- Kagan Y.. (1999) Theory of coherent phenomena and fundamentals in nuclear resonant scattering. *Hyperfine. Interact.*, **123/124**, 83-126.
- Kaneshima S. and Helffrich G. (1999) Dipping low-velocity layer in the mid-lower mantle: Evidence for geochemical heterogeneity. *Science*, **283**, 1888-1891.
- Kantor, I., Dubrovinsky, L. & McCammon, C. (2006) Spin crossover in (Mg,Fe)O: A Mössbauer effect study with an alternative interpretation of x-ray emission spectroscopy data. *Phys. Rev. B*, **73**. 100101-100104
- Keppler, H. & Frost, D. J. (2005) in *Mineral Behaviour at Extreme Conditions* Vol. 7 *EMU Notes in Mineralogy* (ed R. Miletich) 1-30 (Eötvös University Press, 2005).
- Keppler H., Kantor I., and Dubrovinsky L.S. (2007) Optical absorption spectra of ferropericlasite to 84 GPa. *Am. Mineral.* **92**, 433-436

- Keppeler H., Dubrovinsky L.S., Narygina O.V., Kantor I. (2008) Optical absorption and radiative thermal conductivity of silicate perovskite to 125 Gigapascals. *Science* **322**, 1529-1532.
- Kimura K., Lewis R.S., and Anders E. (1974) Distribution of gold and rhenium between nickeliron and silicate melts: implications for the abundances of siderophile elements on the Earth and Moon. *Geochim. Cosmochim. Acta*, **38**, 683–701.
- Klotz, S., J. C. Chervin, P. Munsch, and G. Le Marchand (2009), Hydrostatic limits of 11 pressure transmitting media, *Journal of Physics D: Applied Physics*, **42**, 075413.
- Kolesnikov, A., Kutcherov, V.G. & Goncharov, A.F. (2009) Methane-derived hydrocarbons produced under upper-mantle conditions. *Nature Geoscience*, **2**, 566-570.
- Kotrbová, M., Kadečková, S., Novák, J., Brádrler, J., Smirnov, G.V., & Shvydko, Yu.V. (1985). *J. of Crystal Growth*, **71**, 607-614.
- Krot A.N., Keil K., Goodrich C.A., Scott E.R.D., and Weisberg M.K. (2003) Classification of meteorites, pp. 83-128. In *Meteorites, Comets and Planets* (ed. A.M. Davis) Vol. 1 *Treatise on Geochemistry* (eds. Holland H.D. and Turekian K.K.), Elsevier-Pergamon, Oxford.
- Kurnosov, A., I. Kantor, T. Boffa-Bolaran, S. Lindhardt, L. Dubrovinsky, A. Kuznetsov, and B. H. Zehnder (2008) A novel gas-loading system for mechanically closing of various types of diamond anvil cells. *Rev. Sci. Instrum.*, **79**, 045110.
- Lewis, J. (2004) *Physics and chemistry of the solar system*, 2nd ed., Elsevier Academic Press, Amsterdam, Boston.
- Li J., Struzhkin V.V., Mao H.-K., Shu J., Hemley R.J., Fei Y., Mysen B., Dear P., Prakapenka V.B., and Shen G. (2004) Electronic spin state of iron in lower mantle perovskite. *Proced. Nat. Acad. Sci.* **101**, 14027-14030.
- Li J., Sturhahn W., Jackson J.M. Struzhkin V.V., Lin J.-F., Zhao J., Mao H.-K. and Shen G. (2006) Pressure effect on the electronic structure of iron in (Mg,Fe)(Si,Al)O₃ perovskite: a combined synchrotron Mössbauer and X-ray emission spectroscopy study up to 100 GPa. *Phys. Chem. Minerals.*, **33**, 575-585
- Lin J.-F., Degtyareva, O., Prewitt, C. T., Dera, P., Sata, N., Gregoryanz, E., Mao, H. K. & Hemley, R. J. (2004) Crystal structure of a high-pressure/high-temperature phase of alumina by in situ X-ray diffraction. *Nature materials*, **3**, 389-393.
- Lin J.-F., Struzhkin V.V., Jacobsen S.D., Hu M.Y., Chow P., Kung J., Liu H., Mao H.K., and Hemley R.J. (2005) Spin transition of iron in magnesiowüstite in the Earth's lower mantle. *Nature*, **436**, 377-380.

- Lin J.-F., Gavriluk A.G., Struzhkin V.V., Jacobsen S.D., Sturhahn W, Hu M.Y., Chow P., and Yoo C.S. (2006) Pressure-induced electronic spin transition of iron in magnesiowustite- (Mg,Fe)O. *Phys. Rev. B* **73**, 113107.
- Lin J.-F., Vankó G., Jacobsen S.D., Iota V., Struzhkin V.V., Prakapenka V.B., Kuznetsov A., and Yoo C.S. (2007) Spin transition zone in Earth's lower mantle. *Science* **317**, 1740-1743.
- Lin J.-F., Watson H., Vankó G., Alp E.E., Prakapenka V.B, Dera P., Struzhkin V.V., Kubo A., Zhao J., McCammon C.A., and Evans W.J. (2008) Intermediate-spin ferrous iron in lowermost mantle post-perovskite and perovskite. *Nature Geoscience*, **1**, 688-691.
- Lin J.-F. , E. E. Alp, Z. Mao, T. Inoue, C. McCammon, Y. Xiao, P. Chow, and J. Zhao (2012) Electronic spin and valence states of iron in the lower-mantle silicate perovskite by synchrotron Mössbauer spectroscopy, *Am. Miner.*, **97**, 592-597,
- Lundin, S. *et al.* (2008) Effect of Fe on the equation of state of mantle silicate perovskite over 1 Mbar. *Phys Earth Planet Interioir*, **168**, 97-102.
- Mao, H. K., J. Xu, and P. M. Bell (1986) Calibration of the Ruby Pressure Gauge to 800 kbar Under Quasi-Hydrostatic Conditions, *J. Geophys. Res.*, **91**, 4673-4676
- McCammon C.A., Rubie D.C., Ross II C.R., Seifert F. and O'Neill H.St.C. (1992) Mössbauer spectra of $^{57}\text{Fe}0.05\text{Mg}0.95\text{SiO}_3$ perovskite at 80 and 298 K. *Am. Mineral.*, **77**, 894-897.
- McCammon, C. A. (1997) Perovskite as a possible sink for ferric iron in the lower mantle. *Nature*, **387**, 694-696.
- McCammon C.A. (2005a) The paradox of mantle redox. *Science*, **308**, 807-808
- McCammon C.A. (2005b) Mantle oxidation state and oxygen fugacity: Constraints on mantle chemistry, structure and dynamics, pp. 221-242. In *Earth's Deep Mantle: Structure, Composition, and Evolution* (eds. Hilst R.D., Bass J., Matas J., and Trampert J.), American Geophysical Union, Washington D.C.
- McCammon C.A., Kantor I.Yu., Narygina O., Rouquette J., Ponkratz U., Sergueev I., Mezouar, M., Prakapenka V., Dubrovinsky L.S. (2008) Stable intermediate-spin ferrous iron in lowermantle perovskite. *Nature Geoscience*, **1**, 684-687
- McDonough, W., and S.-S. Sun (1995) The composition of the Earth, *Chemical Geology*, **120**, 223-253.
- Merrill, L., and W. A. Bassett (1974) Miniature diamond anvil pressure cell for single crystal x-ray diffraction studies, *Rev. Sci. Instrum.*, **45**, 290-294.
- Mikhaylushkin, A. , S.I. Simak, L. Dubrovinsky, N. Dubrovinskaia, B. Johansson, I.A. Abrikosov (2007) Pure Iron Compressed and Heated to Extreme Conditions. *Phys. Rev. Lett.* **99**, 165505.

- Ming, L.-chung & Bassett, W.A. (1974) Laser heating in the diamond anvil press up to 2000°C sustained and 3000°C pulsed at pressures up to 260 kilobars. *Rev. Sci. Instrum.*, **45**, 1115
- Mirzababaev R.M., G. V. Smirnov, V. V. Sklyarevskii, A. N. Artem'ev, A. N. Izrailenko, and A. V. Babkov (1971) Purely nuclear diffraction of resonant gamma-rays due to hyperfine quadrupole interactions. *Phys. Lett.*, **37A**, 441-442.
- Mito, M., M. Hitaka, T. Kawae, K. Takeda, T. Kitai, and N. Toyoshima (2001) Development of Miniature Diamond Anvil Cell for the Superconducting Quantum Interference Device Magnetometer. *Jpn. J. Appl. Phys.*, **40**, 6641-6644.
- Mitsui, T., Seto, M., Kikuta, S., Hirao, S., Ohishi, Y., Takei, H., Kobayashi, Y., Kitao, S., Higashitaniguchi, S., & Masuda, R. (2007a) Generation and Application of Ultrahigh Monochromatic X-ray Using High-Quality ⁵⁷FeBO₃ Single Crystal. *Jpn. J. Appl. Phys.* **46**, 821-825.
- Mitsui, T., Seto, M., Hirao, M., Ohishi, Y., Kobayashi, Y., Higashitaniguchi, Y., & Masuda, R. (2007b) Ultrahigh-Pressure Measurement in the Multimegabar Range by Energy-Domain Synchrotron Radiation ⁵⁷Fe-Mössbauer Spectroscopy Using Focused X-rays. *Jpn. J. Appl. Phys.*, **46**, L382-L384.
- Mitsui, T., Seto, M., Masuda, R., Kiriyama, K., & Kobayashi, K. (2007c) Synchrotron Radiation Mössbauer Spectroscopy Using Doppler-shifted 14.4 keV Single-line ⁵⁷Fe-Mössbauer Radiation. *Jpn. J. Appl. Phys.*, **46**, L703-L705.
- Mitsui, T., Seto, M., & Masuda, R. (2007d) Variable-Frequency Nuclear Monochromator Using Single-Line Pure Nuclear Bragg Reflection of Oscillating ⁵⁷FeBO₃ Single Crystal. *Jpn. J. Appl. Phys.*, **46**, L930-L932.
- Mitsui, T., Hirao, N., Ohishi, Y., Masuda, R., Nakamura, Y., Enoki, H., Sakaki K., & Seto, M. (2009) Development of an energy-domain ⁵⁷Fe-Mössbauer spectrometer using synchrotron radiation and its application to ultrahigh-pressure studies with a diamond anvil cell. *J. Synchrotron Rad.*, **16**, 723-729.
- Morgan, J. W. (1986) Ultramafic Xenoliths: Clues to Earth's Late Accretionary History, *J. Geophys. Res.*, **91**, 12375-12387.
- Murakami M., Ohishi Y., Hirao N., and Hirose K. (2012) A perovskitic lower mantle inferred from high-pressure, high-temperature sound velocity data. *Nature*, **485**, 90-94.
- Murakami, M., K. Hirose, K. Kawamura, N. Sata, and Y. Ohishi (2004) Post-Perovskite Phase Transition in MgSiO₃. *Science*, **304**, 855-858.
- Murthy, V. R. (1991) Early Differentiation of the Earth and the Problem of Mantle Siderophile Elements: A New Approach. *Science*, **253**, 303-306.
- Narygina, O., L. S. Dubrovinsky, H. Samuel, C. A. McCammon, I. Y. Kantor, K. Glazyrin, S. Pascarelli, G. Aquilanti, and V. B. Prakapenka (2011) Chemically

- homogeneous spin transition zone in Earth's lower mantle. *Physics of the Earth and Planetary Interiors*, **185**,107-111.
- Narygina, O. (2010) Investigation of the properties of iron-bearing alloys and silicates and their implications for the Earth's lower mantle and core *Dissertation*. <http://opus.ub.uni-bayreuth.de/opus4-ubbayreuth/frontdoor/index/index/docId/558>
- O'Neill, H. S. C., and H. Palme (2000) *Composition of the Silicate Earth: Implications for Accretion and CoreFormation in "The Earth's mantle : composition, structure, and evolution"* 1st ed., edited by I. Jackson, Cambridge University Press, Cambridge [u.a.].
- Ohta K., Onoda S., Hirose K., Sinmyo R., Shimizu K., Sata N, Ohishi Y, Yasuhara A. (2008) The electrical conductivity of post-perovskite in Earth's D" layer. *Science* **320**, 89-91.
- Ohta, K., Hirose, K., Shimizu, K., Sata, N. & Ohishi, Y. (2010) The electrical resistance measurements of (Mg,Fe)SiO₃ perovskite at high pressures and implications for electronic spin transition of iron. *Phys Earth Planet In.i*, **180**, 154-158.
- Ohta, K. *et al.* (2010) Electrical conductivities of pyrolitic mantle and MORB materials up to the lowermost mantle conditions. *Earth Planet. Sci. Lett.*, **289**, 497-502 .
- Palme, H., and K. Nickel (1985) Ca/Al ratio and composition of the Earth's upper mantle. *Geochimica et Cosmochimica Acta*, **49**, 2123-2132.
- Palme H. and Jones A. (2003) Solar system abundances of the elements, pp. 41-61. In *Meteorites, Comets and Planets* (ed. Davis A.M.) Vol. 1 *Treatise on Geochemistry* (eds. Holland H.D.and Turekian K.K.), Elsevier-Pergamon, Oxford.
- Palme J. and O'Neill H.St.C. (2003) Cosmochemical estimates of mantle composition, pp. 1-38. In *The Mantle and Core* (ed. Carlson R.W.) Vol. 2 *Treatise on Geochemistry* (eds. Holland H.D. and Turekian K.K.), Elsevier-Pergamon, Oxford.
- Palyanov, Y.N., Kupriyanov, I.N., Sokol, A.G., Khokhryakov, A.F. & Borzdov, Y.M. (2011) Diamond Growth from a Phosphorus–Carbon System at High Pressure High Temperature Conditions. *Crystal Growth & Design*, **11**, 2599-2605.
- Pankhurst Q.A., N.S. Cohen, L.F. Barquin, M.R. Gibbs, and G.V. Smirnov (2001) Moment canting and structural anisotropy in amorphous alloys: experiments using synchrotron Mossbauer radiation. *J. Non-Cryst. Solids*, **287**, 81-87.
- Parakhonskiy, G., Dubrovinskaia, N., Bykova, E., Wirth, R. & Dubrovinsky, L. (2011) Experimental pressure-temperature phase diagram of boron: resolving the long-standing enigma. *Scientific Reports*, **1**, 96.

- Pippinger, T., Dubrovinsky, L., Glazyrin, K., Miletich, R. & Dubrovinskaia, N. (2011) Detection of melting by in-situ observation of spherical-drop formation in laser-heated diamond-anvil cells. *Fisica de la Tierra*, **23**, 29-41.
- Potapkin, V., McCammon, C., Glazyrin, K., Kantor, A., Kuppenko, I., Prescher, C., Sinmyo, R., Smirnov, G.V., Popov, S., Chumakov, A.I., and Ruffer, R., Dubrovinsky, L. (2013) Effect of iron oxidation state on the electrical conductivity of the Earth's lower mantle. *Nature Communication*, **4**, 1427.
- Prakapenka, V.B., A. Kubo, A. Kuznetsov, A. Laskin, O. Shkurikhin, P. Deraa, M. L. Riversa & S. R. Suttona (2008) Advanced flat top laser heating system for high pressure research at GSECARS: application to the melting behavior of germanium. *High Pressure Research*, **28**, 225-235.
- Prescher, C., McCammon, C. & Dubrovinsky, L. (2012) MossA - a program for analyzing energy-domain Mossbauer spectra from conventional and synchrotron sources. *Journal of Applied Crystallography*, **45** 329-331.
- Ringwood, A. E. (1979) *Origin of the earth and moon*. Springer, New York.
- Ringwood A.E. (1989) Constitution and evolution of the mantle. *Spec. Publ. Geol. Soc. Australia*, **14**, 457-485
- Ruffer R., & Chumakov A.I. (1996) Nuclear resonance beamline at ESRF. *Hyperfine Interact.*, **97/98**, 589-604.
- Rütter H.D., R.Ruffer, E. Gerdau, R. Hollatz, A. I. Chumakov, M. V. Zelepukhin, G. V. Smirnov, and U. van Bürck (1990) Quantum beat dilation due to magnetisation breakdown. *Hyperfine Interact.*, **58**, 2473- 2476.
- Renninger, M. (1937) Röntgenometrische. Beitrage zur Kenntnis der Ladungsverteilung im Diamantgitter. *Z.Krist.*, **97**, 107-121.
- Rubie, D. C., F. Nimmo, and H. J. Melosh (2007) *Treatise on Geophysics*. Elsevier.
- Safranov V.S. (1969) Evolution of the protoplanetary cloud and formation of the Earth and planets (English translation NASA TTF-667, 1972).
- Saikia, A., Boffa Ballaran, T. & Frost, D. J. (2009) The effect of Fe and Al substitution on the compressibility of MgSiO₃ - perovskite determined through single-crystal X-ray diffraction. *Phys Earth Planet In.*, **173**, 153-161.
- Schröder, T. , M.N. Schneider, T. Rosenthal, A. Eisele, C. Gold, E.-W. Scheidt, W. Scherer, R. Berthold and O. Oeckler (2011) Nanostructures in metastable GeBi₂Te₄ obtained by high-pressure synthesis and rapid quenching and their influence on physical properties. *Phys. Rev. B*, **84**, 184104.
- Schultz, E. Mezouar, M., Crichton, W. A., Bauchau, S., Blattmann, G., Andrault, D., Fiquet, G., Boehler, R., Rambert, N., Sitaud, B. & Loubeyre, P. (2005) Double-

- sided laser heating system for in situ high pressure–high temperature monochromatic x-ray diffraction at the ESRF. *High Pressure Research*, **25**, 71-83.
- Seto, M., Masuda, R., Higashitaniguchi, S., Kitao, S., Kobayashi, Y., Inaba, C., Mitsui, T., & Yoda, Y. (2009). *J.Phys.: Conf. Ser.*, **217**, 012002.
- Shen, G., Rivers, M.L., Wang, Y. & Sutton, S.R. (2001) Laser heated diamond cell system at the Advanced Photon Source for in situ x-ray measurements at high pressure and temperature. *Rev. Sci. Instrum.*, **72**, 1273-1282.
- Shen, G., Wang, L., Ferry, R., Mao, H.-kwang & Hemley, R.J. (2010) A portable laser heating microscope for high pressure research. *Journal of Physics: Conference Series* **215**, 012191.
- Sherman D.M. (1988) Structural and magnetic phase transitions in minerals, pp. 113-128, In: *Advances in physical geochemistry* (eds. Ghose S, Coey J.M.D. and Salje E.) Springer, New York 7.
- Sheldrick, G.M. (2008) A short history of SHELX. *Acta crystallographica. Section A, Foundations of crystallography* **64**, 112-22.
- Shull C.G. , W. A. Strauser , and E. O. Wollan (1951) Neutron Diffraction by Paramagnetic and Antiferromagnetic Substances. *Phys. Rev.*, **83** , 333-345.
- Smirnov, G. V., Sklyarevskii, V. V., Voscanian, R. A. & Artem'ev, A. N. (1969) Nuclear diffraction of resonant γ radiation by an antiferromagnetic crystal. *JETP Lett.* **9**, 70-73.
- Smirnov G.V., V.V.Mostovoi, Yu.V. Shvyd'ko, V.N. Seleznev, and V.V.Rudenko (1980) Supression of nuclear reaction in $^{57}\text{FeBO}_3$ crystal. *JETP*, **51** 603-606.
- Smirnov G.V. (1986) Coherent effects in resonant diffraction: Experiment. *Hyperfine Interact.* **27** , 203-218.
- Smirnov, G.V., Zelepukhin, M.V., & van Bürck, U. (1986) Purely nuclear diffraction of Mössbauer radiation in the critical region near Néel point. *JETP Lett.*, **43**, 352-355.
- Smirnov, G.V., van Bürck, U., Chumakov, A.I., Baron, A.Q.R., & Ruffer, R. (1997) Synchrotron Mössbauer source. *Phys. Rev. B* **55**, 5811-5815.
- Smirnov, G. V. (2000) Synchrotron Mössbauer source of ^{57}Fe radiation. *Hyperfine Interact.*, **125**, 91-112.
- Smirnov G.V., U. van Bürck, W. Potzel , P. Schindermann , S.L. Popov , E. Gerdau , Y.V. Shvyd'ko , H.D. Rüter , and O. Leupold (2005) Propagation of nuclear polaritons through a two-target system: Effect of inversion of targets. *Phys.Rev.A* **71** 023804 .
- Smirnov G.V. , U. van Bürck, J. Arthur , G.S. Brown , A.I. Chumakov , A.Q.R. Baron , W. Petry, and S.L. Ruby (2007) Currents and fields reveal the

- propagation of nuclear polaritons through a resonant target. *Phys. Rev. A*, **76**, 043811.
- Smirnov G.V. (2009) Rocking curves, time and energy distributions of synchrotron Mössbauer radiatio of ^{57}Fe . Preprint IAE-6614/9
- Smirnov, G.V., Chumakov, A.I., Potapkin, V., Ruffer, R., & Popov, S.L. (2011) Multispace quantum interference in a ^{57}Fe synchrotron Mössbauer source. *Phys. Rev. A*, **84**, 053851.
- Speziale S., Milner A., Lee V.E., Clark S.M., Pasternak M.P., and Jeanloz R. (2005) Iron spin transition in Earth's mantle. *Proced. Nat. Acad. Sci.*, **102**, 17918-17922
- Stankov, S., Ruffer, R., Sladecsek, M., Rennhofer, M., Sepiol, B., Vogl, G., Spiridis, N., Slezak, T., & Korecki, J. (2008) An ultra-high vacuum system for in-situ studies. *Rev. Sci. Instrum.*, **79**, 045108.
- Stackhouse S., Brodholt J.P., and Price G.D. (2007) Electronic spin transitions in iron-bearing MgSiO_3 perovskite. *Earth Planet. Sci. Lett.*, **253**, 282–290.
- Stixrude L. and Lithgow-Bertelloni C. (2005a) Mineralogy and elasticity of the oceanic upper mantle: origin of the low-velocity zone. *J. Geophys. Res.*, **110**, B03204.
- Stixrude, L., and C. Lithgow-Bertelloni (2005b) Thermodynamics of mantle minerals - I. Physical properties. *Geophysical Journal International*, **162**, 610-632.
- Sturhahn W., Jackson J.M., and Lin J. (2005) The spin state of iron in minerals of the Earth's lower mantle. *Geophys. Res. Lett.*, **32**, L12307.
- Schvyd'ko Y.V. and G. V. Smirnov (1989) Experimental study of time and frequency properties of collective nuclear excitations in a single crystal (gamma-ray resonance). *J. Phys. : Condens. Matter*, **1**, 10563-10584.
- Tonks W.B. and Melosh H.J. (1992) Core formation by giant impacts. *Icarus*, **100**, 326-346.
- Tarits, P. & Mandéa, M. (2010) The heterogeneous electrical conductivity structure of the lower mantle. *Phys Earth Planet In.*, **183**, 115-125.
- Trammell G.T. (1961) in: Proc. Intern. Atomic Energy Agency Symp. on Chemical Effects of Nuclear Transformations. **1**, 75.
- van Bürck U., Smirnov G. V., Mössbauer R. L., Maurus H. J., and Semioschkina N. A. (1980) Enhanced nuclear resonance scattering in dynamical diffraction of gamma rays. *J. Phys. C : Solid St. Phys.*, **13**, 4511-4529.
- van Bürck U., Mössbauer R. L., Gerdau E., Ruffer R., Hollatz R., Smirnov G. V., Hannon J.P. (1987) Nuclear Bragg scattering of synchrotron radiation with strong speedup of coherent decay, measured on antiferromagnetic $^{57}\text{FeBO}_3$. *Phys. Rev.Lett.*, **59**, 355-358.

- Vanpeteghem, C. B., Zhao, J., Angel, R. J., Ross, N. L. & Bolfan-Casanova (2006) N. Crystal structure and equation of state of MgSiO₃ perovskite. *Geophys. Res. Lett.* **33**, L03306.
- Verhoeven, O. A. Mocquet, P. Vacher, A. Rivoldini, M. Menvielle, P.-A. Arrial, G. Choblet, P. Tarits, V. Dehant, and T. Van Hoolst (2009) Constraints on thermal state and composition of the Earth's lower mantle from electromagnetic impedances and seismic data. *J Geophys Res.*, **114**, B03302.
- Wanke, H., G. Dreibus, and E. Jagoutz (1984) *Mantle chemistry and accretion history of the Earth in "Archaean geochemistry : the origin and evolution of the Archaean continental crust"* edited by A. Kroner, Springer-Verlag, Berlin, New York.
- Weir, C. E., E. R. Lippincott, A. V. Valkenburg, and E. N. Bunting (1959) Infrared Studies in the 1-to 15-Micron Region to 30,000 Atmospheres. *J. Res. Natl. Bur. Stand.*, **63A**, 55-62.
- Wetherill G.W. and Stewart G.R. (1993) Formation of planetary embryos: effects on fragmentation, low relative velocity, and independent variation of eccentricity and inclination. *Icarus* **106**, 190-209
- Wicks, J. K., J. M. Jackson, and W. Sturhahn (2010) Very low sound velocities in iron-rich (Mg,Fe)O: Implications for the core-mantle boundary region, *Geophys. Res. Lett.*, **37**, L15304.
- Wu, X., Steinle-Neumann G, Narygina O, Kantor I, McCammon C, Prakapenka V, Swamy V, and Dubrovinsky L (2009) High-Pressure Behavior of Perovskite: FeTiO₃ Dissociation into (Fe_{1-δ},Ti_δ)O and Fe_{1+δ}Ti_{2-δ}O₅. *Phys. Rev. Lett.* **103**, 065503.
- Xu, Y., C. McCammon, and B. T. Poe (1998) The Effect of Alumina on the Electrical Conductivity of Silicate Perovskite. *Science*, **282**, 922-924.
- Xu, Y., Shankland, T. J. & Poe, B. T. (2000) Laboratory-based electrical conductivity in the Earth's mantle. *J Geophys Res.*, **105**, 865-875.
- Yoshida, Y., Suzuki, K., Hayakawa, K., Yukihiro, K., & Soejima, H. (2009) Mössbauer spectroscopic microscope. *Hyperfine Interact.*, **188**, 121-126.
- Yoshino, T., Ito E., Katysura T., Yamazaki D., Shan S., Guo X., Nishi M., Higo Y., Funakoshi K. (2011) Effect of iron content on electrical conductivity of ferropericlase with implications for the spin transition pressure. *Geophys. Res. Lett.*, **116**, B04202.
- Zhang, F. & Oganov, A. R. (2006) Valence state and spin transitions of iron in Earth's mantle silicates. *Earth Planet. Sci. Lett.*, **249**, 436-443 .

Zelepukhin, M.V., Smirnov, G.V., van Bürck, U. (1985) *Voprosy atomnoĭ nauki i tekhniki*. **4(33)**, 76-77 (in Russian).

Zerr, A., G. Miehe, J. Li, D.A. Dzivenko, V.K. Bulatov, H. Höfer, N. Bolfan-Casanova, M. Fialin, G. Brey, T. Watanabe, and M. Yoshimura (2009) High-Pressure Synthesis of Tantalum Nitride Having Orthorhombic U₂S₃ Structure. *Advanced Functional Materials*, **19**, 2282-2288.

Acknowledgments

I would to thank all my supervisors. Professor Dr. Leonid Dubrovinsky for very interesting problem setting and even more for motivation, support and optimism on course of the thesis. Thank you for letting me in to the wonderful world of high-pressure physics. Dr. Alexander Chumakov for his patience, supervision, and numerous priceless advices. Thank you so much for introducing me to the cutting edge of x-ray experimental science and for all the things that you taught me over these years on daily basics.

My deepest gratitude goes Dr. Catherine McCammon for her scientific advices and for help with Mössbauer measurements. Thank you for your teaching. In addition, I would like to thank Prof. Gennady Smirnov for his help with calculations and vast wisdom, which he sheared always when it was needed.

I would like to thank the whole collective of ID18 of the ESRF of my time: Dr. Rudolf Ruffer, Dr. Ilya Sergueev, Dr. Marcin Zajac and Jean-Philip Celse. Thank you for your help, discussion, and the wonderful working atmosphere at the beamline.

I am thankful to all people who helped me with experiments and provided samples (in alphabetic order): Dr. Konstantin Glazyrin, Dr. Anastasia Kantor, Ilya Kупenko, Dr. Ryosuke Sinmyo.

I am very grateful to all my friends at Grenoble, especially to Innokenty Kantor, Alexei Bosak, Immaculada Martínez-Rovira, Lena Chumakova and Boaz Nash for many discussions - scientific and not, and for the time we spend together in Grenoble. Without all of you people it would have been much tougher.

Finally, I feel obliged to my family, to my father - Boris and my mother - Natalya for having providing me with good education and for all the love and support over all these years. I would never manage to repay you.

This work was supported through ESRF thesis fellowship program.

Erklärung

Hiermit erkläre ich, dass ich die vorliegende Arbeit selbständig verfasst und keine anderen als die von mir angegebenen Quellen und Hilfsmittel benutzt habe. Die aus fremden Quellen direkt oder indirekt übernommenen Gedanken sind als solche kenntlich gemacht.

Ferner erkläre ich, dass ich nicht anderweitig versucht habe, mit oder ohne Erfolg, eine Dissertation einzureichen und auch keine gleichartige Doktorprüfung an einer anderen Hochschule endgültig nicht bestanden habe.

Grenoble, France
29.06.2012